UNIVERSITY OF CALIFORNIA, SAN DIEGO

All-optical Nonlinear Switching in Optical Micro-resonators on a Silicon Chip

A dissertation submitted in partial satisfaction of the
requirements for the degree Doctor of Philosophy

in

Electrical Engineering (Photonics)

by

Kazuhiro Ikeda

Committee in charge:

Professor Yeshaiahu Fainman, Chair
Professor Prabhakar R. Bandaru
Professor Shayan Mookherjea
Professor Lu J. Sham
Professor Paul K. L. Yu

2008

The Dissertation of Kazuhiro Ikeda is approved, and it is acceptable in quality and form for publication on microfilm and electronically:

_____

_____

_____

_____

_____

Chair

University of California, San Diego

2008

DEDICATION

This dissertation is dedicated to my family, my parents and my wife, Miyuki, who have allowed and supported my graduate study abroad.

TABLE OF CONTENTS

LIST OF ABBREVIATIONS

1D	One Dimensional
2D	Two Dimensional
AlGaAs	Aluminum Gallium Arsenide
a-Si	Pure Amorphous Silicon
a-Si:H	Hydrogenated Amorphous Silicon
CMOS	Complementary Metal-Oxide Semiconductor
c-Si	Crystalline Silicon
CW	Continuous Wave
DBR	Distributed Bragg Reflector
e-beam	Electron Beam
FDTD	Finite Difference Time Domain
FOM	Figure of Merit
FSR	Free Spectral Range
FWHM	Full Width at the Half Maximum
GaAs	Gallium Arsenide
HF	Hydrofluoric Acid
HSQ	Hydrogen Silsesquioxane
HWHM	Half Width at the Half Maximum
ICP	Inductively Coupled Plasma
IPA	Isopropanol
LHS	Left-Hand Side

LPCVD	Low Pressure Chemical Vapor Deposition
MIBK	Methyl Isobutyl Ketone
PECVD	Plasma-Enhanced Chemical Vapor Deposition
PhC	Photonic Crystal
PIC	Photonic Integrated Circuit
PMMA	Poly-Methyl Methacrylate
RHS	Right-Hand Side
RIE	Reactive Ion Etching
SEM	Scanning Electron Microscope
Si	Silicon
SiN	Silicon Nitride
SiO_2	Silicon Dioxide
SOI	Silicon on Insulator
TE	Transverse Electric
ThPA	Three Photon Absorption
TM	Transverse Magnetic
TMAH	Tetra-Methyl Ammonium Hydroxide
TPA	Two Photon Absorption
TSA	Two-Step Absorption
VG	Vertical Grating
WDM	Wavelength Division Multiplexing
WSC	Wavelength Selective Coupler

LIST OF FIGURES

LIST OF TABLES

ACKNOWLEDGEMENTS

I would like to acknowledge Professor Yeshaiahu Fainman for his support as my adviser and the chair of my committee. His guidance has proved to be invaluable.

I would also like to acknowledge the post-doctoral fellows (especially, Dr. Hyo-Chang Kim, Dr. Uriel Levy and Dr. Lin Pang) and the graduate students (especially, the graduates, Dr. Chia-Ho Tsai, Dr. Nikola Alic, Dr. Robert Saperstein, Dr. Maziar Nezhad and Dr. Yaoming Shen) from the Fainman's group, without whom my research would have no doubt taken much longer. It is their support that helped me in an immeasurable way.

My graduate study was partially supported by the scholarship award from the Nakajima Foundation, Japan.

Chapter 2, in part, is a reprint of the material as it appears in:

- K. Ikeda, M. Nezhad and Y. Fainman, "Wavelength selective coupler with vertical gratings on silicon chip," Appl. Phys. Lett. 92, 201111 (2008).

The dissertation author was the primary investigator and author of this paper. The co-authors listed in the publication assisted and supervised the research which forms the basis for this chapter.

Chapter 3, in part, is a reprint of the material as it appears in:

- K. Ikeda and Y. Fainman, "Nonlinear Fabry-Perot resonator with a silicon photonic crystal waveguide," Opt. Lett. 31, 3486-3488 (2006).
- K. Ikeda and Y. Fainman, "Material and structural criteria for ultra-fast Kerr nonlinear switching in optical resonant cavities," Solid-State Electron. 51,

1376-1380 (2007).

The dissertation author was the primary investigator and author of these papers. The co-authors listed in these publications directed and supervised the research which forms the basis for this chapter.

Chapter 4, in part, is a reprint of the material as it appears in:

- K. Ikeda, Y. Shen and Y. Fainman, "Enhanced optical nonlinearity in amorphous silicon and its application to waveguide devices," Opt. Express 15, 17761-17771 (2007).

and, in part, is currently being prepared for submission for publication of the material. The dissertation author was the primary investigator and author of these papers. The co-authors listed in the publication assisted and supervised the research which forms the basis for this chapter.

Chapter 5, in part, is a reprint of the material as it appears in:

- K. Ikeda, R. E. Saperstein, N. Alic and Y. Fainman, "Thermal and Kerr nonlinear properties of plasma-deposited silicon nitride/ silicon dioxide waveguides," Opt. Express 16, 12987-12994 (2008).

The dissertation author was the primary investigator and author of this paper. The co-authors listed in the publication assisted and supervised the research which forms the basis for this chapter.

VITA

1998	Bachelor of Engineering, Osaka University, Japan
2000	Master of Engineering, Osaka University, Japan
2000-2004	Researcher, Furukawa Electric Co. Ltd., Japan
2005-2008	Research Assistant, University of California, San Diego
2008	Doctor of Philosophy, University of California, San Diego

SELECTED PUBLICATIONS

K. Ikeda, "PMD Compensator With Second Order PMD Mitigation Using Mode-Coupled Fixed Delay," IEEE Photon. Technol. Lett. 16, 105-107, (2004).

K. Ikeda and Y. Fainman, "Nonlinear Fabry-Perot resonator with a silicon photonic crystal waveguide," Opt. Lett. 31, 3486-3488 (2006).

K. Ikeda and Y. Fainman, "Material and structural criteria for ultra-fast Kerr nonlinear switching in optical resonant cavities," Solid-State Electron. 51, 1376-1380 (2007).

K. Ikeda, Y. Shen and Y. Fainman, "Enhanced optical nonlinearity in amorphous silicon and its application to waveguide devices," Opt. Express 15, 17761-17771 (2007).

K. Ikeda, M. Nezhad and Y. Fainman, "Wavelength selective coupler with vertical gratings on silicon chip," Appl. Phys. Lett. 92, 201111 (2008).

K. Ikeda, R. E. Saperstein, N. Alic and Y. Fainman, "Thermal and Kerr nonlinear properties of plasma-deposited silicon nitride/ silicon dioxide waveguides," Opt. Express 16, 12987-12994 (2008).

ABSTRACT OF THE DISSERTATION

All-optical Nonlinear Switching in Optical Micro-resonators on a Silicon Chip

by

Kazuhiro Ikeda

Doctor of Philosophy in Electrical Engineering (Photonics)

University of California, San Diego, 2008

Professor Yeshaiahu Fainman, Chair

Silicon-based optical interconnects compatible with the standard complementary metal-oxide semiconductor (CMOS) technology are desirable for the realization of on-chip optical interconnections, which have the advantages of high refractive index resulting in nanometer scale waveguides, and of highly cost-effective integrations. Numerous researches thus have been recently conducted in this field, so called “Silicon Photonics”. This dissertation addresses all-optical nonlinear switching

processes, specifically, the critical issue of long free-carrier lifetime in optical micro-resonators where small nonlinearities of the material can be enhanced due to the accumulation of the optical amplitude and phase. The phenomenon observed previously was that the all-optical nonlinear switching in silicon micro-resonators was induced through free carrier refraction via two-photon absorption (TPA) and the lifetime of the photo-excited free-carriers had been the limit for the response time of the switching or modulating operations. For faster switching, bound electronic nonlinearity, i.e. Kerr nonlinearity is preferred.

First, we quantitatively confirm that silicon cannot be considered as the materials for the resonator-enhanced Kerr nonlinear switch at 1.55μm of wavelength, due to the large free-carrier nonlinearity excited by TPA. Therefore, the material of micro-resonators is reconsidered in two directions to solve the issue of the long-lived free carriers; (i) amorphous silicon as a material with faster carrier recombination, (ii) silicon nitride (SiN) as a material with a smaller TPA coefficient. We present the first measurements of optical nonlinearity due to free carrier effects in amorphous silicon films using z-scan technique, demonstrating enhanced nonlinearity due to existence of midgap localized states. We also introduce a new composite waveguide structure consisting of amorphous and crystalline silicon whose measured free-carrier lifetime is shorter than that in pure crystalline silicon waveguides due to existence of the midgap localized states in amorphous silicon. We then present experimental evaluations of loss and nonlinear optical response in waveguides and micro-resonators, both implemented with a SiN/silicon dioxide (SiO_2) material platform. The fabricated ring resonators are

used to observe the all-optical switching and to measure both the thermal and ultrafast Kerr nonlinearities. The nonlinear refractive index of SiN is measured for the first time.

Chapter 1

Introduction

1.1 Overview of Silicon Photonics

Fiber-optic interconnections are commonly used for a wide range of transmission distances, i.e. intercontinental undersea cable systems, terrestrial long haul systems, inter- and intra-metropolitan backbone systems and the Fiber-To-The-Home access networks, and they support today's growing market of information technologies [1]. In contrast to the success of optics in the above fields, very short distance interconnections, such as chip-to-chip or on-chip interconnects inside computers have been achieved using electronics. This is primarily due to the following properties of current photonic integrated circuits (PICs); (i) the compactness of the PIC is not sufficient (centimeters) because the commercially available PIC is based on silica waveguides with a small index contrast between the waveguide core and cladding, (ii) the monolithic integration of all the required components, especially active ones such as lasers and amplifiers, is not available, which leads to high costs to integrate. These properties do not limit the use of the PIC in the fiber-optic communication systems since (i) the PIC used in the network nodes does not have to

be very small and (ii) the high cost of the PIC can be paid by the huge number of shared users, while these properties become critical drawbacks in the on-chip scale integration for consumer products. Recently, more attention is being paid to optical interconnections even for on-chip scale, due to increase in device density, power dissipation, and inter-channel crosstalk and interference [2]. Silicon-based optical interconnects compatible with a standard complementary metal-oxide semiconductor (CMOS) technology are thus desirable for the realization of on-chip optical interconnections, which solves the above drawbacks for on-chip scale integration since (i) the high refractive index of silicon core results in nanometer scale waveguides and (ii) the standard CMOS fabrication technology offers highly cost-effective integrations once some active devices become available in the silicon platform. Numerous researches have been recently conducted in this field, so called “Silicon Photonics”, including waveguides [3, 4], couplers/splitters [5, 6], modulators/switches [7-9], lasers [10, 11], amplifiers [12, 13] and detectors [14] on silicon chips to exploit the advantages of silicon photonics integration. The realization of the silicon-based on-chip interconnects and integrated systems using the above components are now being attempted. As for the modulators/switches, currently around 10GHz modulations with the electrical driving have been demonstrated [9]. However, faster modulation/switching will require all-optical process using the optical nonlinear response of material. In this dissertation, we discuss the all-optical nonlinear switching in optical micro-resonators on a silicon chip. In the next section, we describe how the optical resonators are beneficial for the all-optical nonlinear switching.

1.2 Enhancement of Nonlinear Effects in Optical Resonators

In optical resonators, the intensity and the phase of optical field are accumulated due to the multiple round trips caused by feedbacks with mirrors or couplers. As a result of the intensity accumulation, the intensity inside the resonator becomes higher than the input intensity depending on the finesse of the resonator. Since the nonlinear optical response of the material becomes more significant when the optical intensity gets higher, the nonlinear response is enhanced inside the resonator. Also, as a result of the phase accumulation, the intensity and the phase at the output of the resonator becomes more sensitive to the "single-pass" phase shift caused by the nonlinear response inside the resonator. Therefore, the nonlinear response of the material can be magnified by the optical resonator. We describe these benefits in detail as follows.

Consider a Fabry-Perot resonator depicted in Fig. 1.1. We define the cavity length L, the amplitude transmittance of the mirror t, the amplitude reflectance of the mirror r, the input optical field amplitude a and the wave number inside the resonator k. Here, we assume for simplicity that the losses in the resonators and the mirrors are negligible, and that the transmittance and the reflectance are real, i. e. k, t and r are real and $t^2 + r^2 = 1$. The optical field amplitude $E(z)$ inside the resonator ($0 < z < L$) is given by,

$$E(z) = \frac{at}{1 - r^2 e^{-2jkL}} \left[e^{-jkz} + re^{-2jkL} e^{jkz} \right]. \tag{1.1}$$

The first term and the second term in Eq. (1.1) correspond to the forward propagating

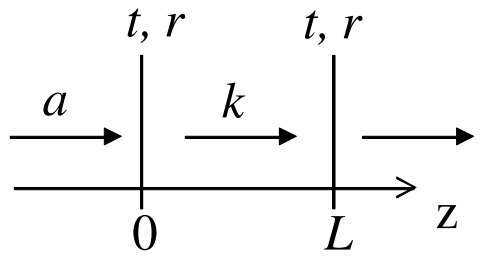

Fig. 1.1 Schematic diagram of a Fabry-Perot resonator with two mirrors.

field and the backward propagating field, respectively. Therefore, the field transmittance right after the mirror at $z = L$ can be written as,

$$T = \frac{tE_{forward}(L)}{a} = \frac{e^{-jkL}\left(1-r^2\right)}{1-r^2e^{-2jkL}}. \tag{1.2}$$

We now calculate the intensity magnification inside the resonator. The magnification factor M is defined as the ratio of the intensity inside the resonator to the input intensity and thus can be calculated using Eq. (1.1) as,

$$M = \frac{\left|E(z)\right|^2}{\left|a\right|^2} = \frac{1+r}{1-r}, \tag{1.3}$$

where on-resonance ($kL = m\pi$) and the maximum point ($\cos 2kz = 1$) are assumed. This means that the higher the reflectance is, the more significant the intensity magnification is. For example, r = 0.9, 0.99, 0.999… give M = 19, 199, 1999…, although a finite loss in the resonator reduces the magnification factor.

Next, we describe the sensitivity of the intensity and phase at the output of the resonator to the single-pass phase shift inside the resonator. The sensitivity of the transmitted intensity to the single-pass phase ($\phi \equiv kL$) can be measured by the half width at the half maximum (HWHM) in phase of the resonant mode $\phi_{1/2}$, which can be

calculated from the equation;

$$|T|^2 = \frac{(1-r^2)^2}{1-2r^2\cos 2\phi_{1/2} + r^4} = \frac{1}{2}. \tag{1.4}$$

Assuming $\cos 2\phi_{1/2} \sim 1 - 2\phi_{1/2}^2$ for a high finesse ($\phi_{1/2} << \pi$), we obtain,

$$\phi_{1/2} = \frac{1-r^2}{2r}. \tag{1.5}$$

This equation means a higher reflectivity gives a smaller HWHM. For example, r = 0.9, 0.99, 0.999… give $\phi_{1/2}$ = 0.1, 0.01, 0.001… Therefore, the transmitted intensity of the resonator can be changed by a small single-pass phase shift in the resonators.

The sensitivity of the transmitted phase to the single-pass phase can be measured by the derivative of the transmitted phase ϕ_{eff} with relation to ϕ. That is;

$$\frac{d\phi_{eff}}{d\phi} = \frac{d}{d\phi}\arg(T) = \frac{1+r^2}{1-r^2} \tag{1.6}$$

where on-resonance ($\phi = m\pi$) are assumed. This equation is similar to Eq. (1.3) except that r is in square. Therefore again, the higher the reflectance is, the more sensitive the transmitted phase is. For example, r = 0.9, 0.99, 0.999… give $d\phi_{eff}/d\phi$ = 9.5, 99.5, 999.5…

As we discussed above, optical resonators can doubly enhance nonlinear optical responses of the material in the following way; (i) the intensity inside the resonator is higher than the input intensity, (ii) the transmitted intensity and phase of the resonator is sensitive to the single-pass phase shift inside the resonator. Since both the transmitted intensity and phase are sensitive to the single-pass phase shift, the optical resonators can be used for both intensity and phase modulation. In this

dissertation, we focus on the intensity modulation. Resonators with higher reflectivity mirrors, resulting in a higher finesse, enhance the nonlinear responses more significantly. However, we have to note that a finite loss inside the resonator degrades the strength of enhancement, and that a higher finesse narrows the transmitted bandwidth of the resonant mode. The detail analysis including the effect of loss and bandwidth is described in Chapter 3. In the next section, we refer to demonstrated all-optical nonlinear switches in optical micro-resonators on a silicon chip in the literature and find the problems in the current devices.

1.3 Nonlinear Switching in Silicon Micro-resonators

Among the numerous demonstrated devices on silicon chips, several all-optical nonlinear switches in silicon micro-resonators have been reported. For example, in Ref. [8], a silicon ring resonator with 10μm diameter was pumped by 10ps pulses at one resonant wavelength and probed by continuous wave (CW) light at another resonant wavelength, where both pump and probe wavelengths are close to 1.55μm (0.8eV). The pump pulses excited free-carriers via two-photon absorption (TPA) inside the ring resonator, which changed the refractive index, shifted the resonant modes and therefore modulated the CW probe. In Ref. [15], a two-dimensional (2D) silicon photonic crystal (PhC) resonator with the cavity length of ~2.1μm was pumped and probed in the similar way as in Ref. [8] and the modulation of the CW probe was also observed. However, in both the devices, the long-lived free carrier effect in silicon (450ps in Ref. [8] and 100ps in Ref. [15]) limits the response time of the devices. The 2D silicon PhC resonator provided a faster recombination because the structure has

periodic holes around the cavity and the generated carriers can diffuse and recombine via surface states on the hole sidewalls. However, the decay time of 100ps is still not sufficiently fast compared to the electrically driven 10GHz modulator. Also, 2D PhC devices have not yet been considered as a standard and practical silicon photonics platform because it requires more precise fabrication (the period and size of holes) over a large area for the desired optical properties, compared to the channel or rib type waveguide devices. This dissertation mainly addresses the issue of the long-lived carrier lifetime in optical micro-resonators with standard waveguide structures on a silicon chip.

1.4 Outline of the Dissertation

As mentioned above, the all-optical nonlinear switching in the demonstrated devices on a silicon chip was found to be induced through free carrier refraction via TPA. This is because the corresponding photon energy (0.8eV) of the operating wavelength (1.55μm) is larger than the half of the band gap energy of silicon (~1.1eV) and the TPA coefficient of silicon is relatively large. For faster switching, bound electronic nonlinearity, i.e. Kerr nonlinearity will be preferred because of the ultrafast response. The question is if it is possible to obtain all-optical switching based on Kerr nonlinearity in silicon micro-resonators with any specific structure design. If it is impossible, the material of micro-resonators will have to be reconsidered in two directions to solve the issue of the long-lived carrier lifetime; (i) a material with faster carrier recombination, (ii) a material with a wider energy band gap, i.e. smaller TPA coefficient. In addition, both the materials should be compatible to the standard CMOS

process for on-chip scale integration. This dissertation is organized in the followings to explore the above theoretical question and the new materials.

In Chapter 2, we review several basic optical resonant structures categorized into localized feedback structures and distributed feedback structures. The mathematical expressions for these structures introduced in this chapter are used in the following chapters. In addition, we discuss an application of the distributed feedback structure, i.e. wavelength selective coupler with vertical gratings, as a new type of devices useful for on-chip scale PICs.

In Chapter 3, we first analyze the nonlinear switching in a silicon micro-resonator, in particular, how the switching works considering the free carrier nonlinearity excited via TPA and the Kerr nonlinearity. Next, the analysis is extended to the discussion of if it is possible to obtain switching based on Kerr nonlinearity in silicon micro-resonators with any specific structure design. We present material and structural criteria for ultra-fast Kerr nonlinear switching in optical resonant cavities. The material criterion with a new nonlinear figure of merit suggests that Si, GaAs and even AlGaAs cannot be considered as the materials for the resonator-enhanced Kerr nonlinear switch at 1.55μm of wavelength, due to the large free-carrier nonlinearity excited by two-photon or three-photon process. We find that insulators with wider band-gaps such as silicon dioxide and silicon nitride will be interesting materials to investigate for this purpose.

In Chapter 4, we investigate amorphous silicon as a material with faster carrier recombination. A large density of localized defect states in amorphous silicon will

work as recombination centers and lead to a shorter carrier lifetime. We present the first measurements of optical nonlinearity due to free carrier effects in amorphous silicon films using z-scan technique, demonstrating enhanced nonlinearity due to the existence of midgap localized states. We also introduce a new composite waveguide structure consisting of amorphous and crystalline silicon. Due to the existence of the midgap localized states in amorphous silicon, the measured free-carrier lifetime in the composite waveguides becomes shorter than the values in crystalline silicon waveguides.

In Chapter 5, we study silicon nitride as a material with a wider energy band gap. We present experimental evaluations of loss and nonlinear optical response in a waveguide and optical resonators, both implemented with a silicon nitride/ silicon dioxide material platform prepared by plasma-enhanced chemical vapor deposition with dual frequency reactors that significantly reduces the stress and the consequent loss of the devices. The fabricated ring resonators are used to observe the all-optical switching and to measure both the thermal and ultrafast Kerr nonlinearities. The nonlinear refractive index n_2 for silicon nitride that is unknown in the literature is measured, for the first time.

Chapter 6 summarizes the dissertation and suggests future directions led from the dissertation.

Chapter 2

Optical Resonant Structures for On-chip Scale Integrations

In this chapter, we review several optical resonant structures categorized into localized feedback structures and distributed feedback structures, as the preparation for embarking on the nonlinear optical responses inside such resonators. The mathematical expressions of these structures are described, which will be used to analyze their nonlinear responses in the following chapters. Also, we discuss an application of the distributed feedback structure, i.e. wavelength selective coupler with vertical gratings, as a new type of device useful for on-chip scale PIC.

2.1 Localized Feedback Structures

Mirrors and couplers are the major localized feedback structures used to configure several types of optical resonators. Fig. 2.1 shows four typical resonators with mirrors and couplers. Fig. 2.1(a) is the Gires-Tournois resonator consisting of a partially reflective mirror and a highly reflective mirror. Fig. 2.1(b) is the Fabry-Perot resonator that has been already touched in section 1.2. Fig. 2.1(c) is the ring resonator

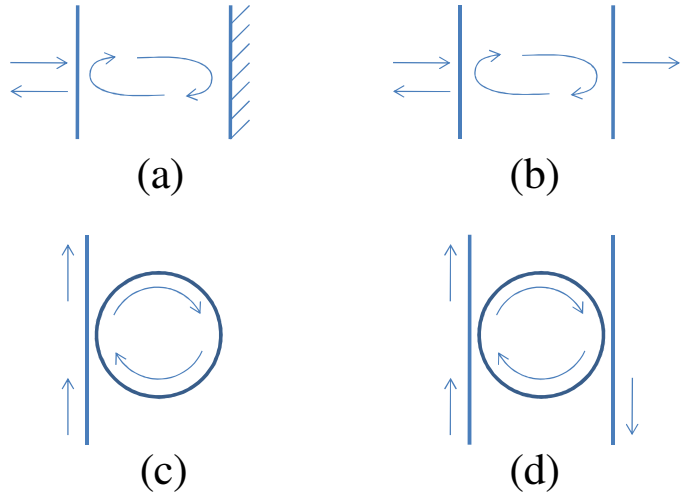

Fig. 2.1 Typical resonant structures with localized feedback structures; (a) Gires-Tournois resonator, (b) Fabry-Perot resonator, (c) all-pass ring resonator, (d) add-drop ring resonator

with all-pass configuration and Fig. 2.1(d) is the ring resonator with add-drop configuration. We can see that the mathematical expression for Fig. 2.1(a) and (b) are same as those for Fig. 2.1(c) and (d) respectively, except that the intensities inside Fig. 2.1(a) and (b) are four times as large as Fig. 2.1(c) and (d) since the forward propagating wave and the backward propagating wave overlap spatially in Fig. 2.1(a) and (b). We also note that, for on-chip scale waveguide devices, mirrors can be realized only by distributed feedback structures [15-18]. Therefore, we consider the structures in Fig. 2.1(c) and (d) in this section.

For the all-pass ring resonator in Fig. 2.1(c), the optical intensity $I(z)$ inside the resonator at resonance is written as [19],

$$I(z) = \frac{a(1-\kappa)\exp(-\alpha z)}{\left(1-\sqrt{\kappa}\exp\left(\frac{-\alpha L}{2}\right)\right)^2}, \tag{2.1}$$

where a is the input intensity, $(1-\kappa)$ is the intensity coupling coefficient between the

bus waveguide and the ring, α is the intensity attenuation inside the ring, L is the perimeter of the ring, z is the coordinate measured along the perimeter (z = 0 ~ L). Therefore, the magnification factor M for this structure may be computed by,

$$M = \frac{I(L)}{a} = \frac{(1-\kappa)\exp(-\alpha L)}{\left(1-\sqrt{\kappa}\exp\left(\frac{-\alpha L}{2}\right)\right)^2}. \tag{2.2}$$

In addition, the intensity transmittance of the resonator is given by [19],

$$T(\phi) = \frac{\kappa - 2\sqrt{\kappa}\exp\left(\frac{-\alpha L}{2}\right)\cos\phi + \exp(-\alpha L)}{1-2\sqrt{\kappa}\exp\left(\frac{-\alpha L}{2}\right)\cos\phi + \kappa\exp(-\alpha L)}, \tag{2.3}$$

where ϕ is the single-pass phase inside the ring ($\phi \equiv kL$). In the same way when we obtained Eq. (1.5), we can calculate the HWHM $\phi_{1/2}$ and then obtain the full width at the half maximum (FWHM) $\Delta\phi \equiv 2\phi_{1/2}$ as,

$$\Delta\phi = 2\sqrt{\frac{1-2\kappa+2\sqrt{\kappa}\exp\left(\frac{-\alpha L}{2}\right)+(\kappa-2)\exp(-\alpha L)}{\sqrt{\kappa}\exp\left(\frac{-\alpha L}{2}\right)}}, \tag{2.4}$$

or solving it for κ;

$$\kappa = \left(\frac{\left(2-\frac{\Delta\phi^2}{4}\right)\exp\left(\frac{-\alpha L}{2}\right)+\sqrt{\left(2-\frac{\Delta\phi^2}{4}\right)^2\exp(-\alpha L)-4(\exp(-\alpha L)-2)(1-2\exp(-\alpha L))}}{2(\exp(-\alpha L)-2)}\right)^2. \tag{2.5}$$

We will need to estimate the magnification factor M to know the intensity inside the resonator and to analyze the nonlinear response. To do this, we first estimate α by fitting Eq. (2.3) to the measured transmission spectrum. Note that since the FWHM $\Delta\phi$ is known in the measured transmission spectrum and the single-pass phase is at the resonant phase (ϕ = 2mπ), the Eq. (2.3) depends only on α. Second, we calculate κ

using the estimated α and Eq. (2.5). Finally, we obtain M using Eq. (2.2).

For the add-drop ring resonator in Fig. 2.1(d), we can analogize the forward propagating wave $E_f(z)$ and the backward propagating wave $E_b(z)$ from Eq. (1.1) by replacing $r^2 \rightarrow \kappa$, $t^2 \rightarrow 1 - \kappa$, $L \rightarrow L/2$ and $k \rightarrow k - j\alpha/2$,

$$E_f(z) = \frac{a\sqrt{1-\kappa}\exp(-jkz)\exp\left(\frac{-\alpha z}{2}\right)}{1-\kappa\exp(-j\phi)\exp\left(\frac{-\alpha L}{2}\right)} \qquad z = 0 \sim L/2, \tag{2.6}$$

$$E_b(z) = \sqrt{\kappa}E_f(z) \qquad z = L/2 \sim L. \tag{2.7}$$

If we take the average of these at $z = L/2$ and on resonance, we obtain the intensity magnification factor inside the ring as,

$$M = \frac{1+\kappa}{2}\frac{(1-\kappa)\exp\left(\frac{-\alpha L}{2}\right)}{\left(1-\kappa\exp\left(\frac{-\alpha L}{2}\right)\right)^2}. \tag{2.8}$$

In addition, the intensity transmittance of the resonator at the drop port is given by,

$$T(\phi) = \frac{(1-\kappa)\left|E_f\left(\frac{L}{2}\right)\right|^2}{|a|^2} = \frac{(1-\kappa)^2\exp\left(\frac{-\alpha L}{2}\right)}{1-2\kappa\exp\left(\frac{-\alpha L}{2}\right)\cos\phi+\kappa^2\exp(-\alpha L)}. \tag{2.9}$$

In the same way when we obtained Eq. (1.5), (2.4) and (2.5), we have the $\Delta\phi$ and κ as,

$$\Delta\phi = 2\frac{1-\kappa\exp\left(\frac{-\alpha L}{2}\right)}{\sqrt{\kappa}\exp\left(\frac{-\alpha L}{4}\right)}, \tag{2.10}$$

$$\kappa = \exp\left(\frac{\alpha L}{2}\right)\left(\frac{\left(\frac{\Delta\phi}{2}\right)^2+2-\frac{\Delta\phi}{2}\sqrt{\left(\frac{\Delta\phi}{2}\right)^2+4}}{2}\right). \tag{2.11}$$

Again, in order to calculate M, we first estimate α by fitting Eq. (2.9) to the measured transmission spectrum, and then calculate κ using the estimated α and Eq. (2.11), and finally obtain M using Eq. (2.8).

2.2 Distributed Feedback Structures

As pointed out in the previous section, for on-chip scale waveguide devices, mirrors can be realized only by distributed feedback structures. The distributed feedback structures, such as 2D PhC [15], one dimensional (1D) PhC implemented in a waveguide [16], deeply etched waveguide grating [17] and sidewall modulated waveguide grating [18], possess periodic index modulations in the direction of light propagation and thus impose the Bragg condition on the propagating light mode in which the mode is reflected to the extent dependent on the strength of the index contrast and the length of the structure. This response is understood as the collective interference of the distributed reflections at each periods of the index modulation and the structure itself has a filter response. When the operating wavelength satisfies the Bragg condition, we can replace the mirrors in Fig. 2.1(a) and (b) with the distributed feedback structures (or in other words, distributed Bragg reflectors (DBRs)) to configure the resonators in on-chip scale as demonstrated [15-18]. The mathematical expressions for these resonators are same as Eq. [2.1] ~ [2.11] except that the intensity inside the resonators are four times larger and that $\kappa \rightarrow r^2$, $L \rightarrow 2L$. The mathematical treatment of the DBRs will be given in the next section.

Since the DBR itself has a filter response, we could make functional devices using the structure. In the next section, we describe a wavelength selective coupler with sidewall modulated waveguides as a new type of functional devices useful for on-chip scale PICs.

2.3 Application of Distributed Feedback Structure: Wavelength Selective Coupler with Vertical Gratings on a Silicon Chip

Development of compact devices using a single lithographic step is essential for cost-effective manufacturing with the standard silicon technology. To meet this objective, we recently constructed a compact silicon photonic device using vertical grating (VG) structure [18, 20] although a similar grating structure but with different waveguide geometry had been reported in Ref. [21]. The sidewalls of a channel-type waveguide are modulated (we call this structure VG) to impose a Bragg condition for the propagating waveguide modes. This structure can be simply integrated upon the definition of the waveguide geometry without additional lithographic process, while horizontal gratings require an additional process after fabricating the waveguide. And this VG structure is useful for filters, resonators, and modulators as demonstrated in Ref [20]. In this section, we show a pair of coupled VG waveguides that create a wavelength selective coupler (WSC) to implement a compact add-drop device useful for wavelength division multiplexing (WDM). We describe the design, fabrication and characterization of our add-drop device. Our device has very large free spectral range (FSR) supporting the total bandwidth of about 70nm used in WDM systems, whereas the FSR of a ring resonator implementation is limited to about 20nm for typical ring designs with radius of about 5μm [8].

Fig. 2.2 shows the schematic diagram of WSC. Two waveguides WG1 and WG2 with VGs are placed close together with a gap *G*, which have different widths

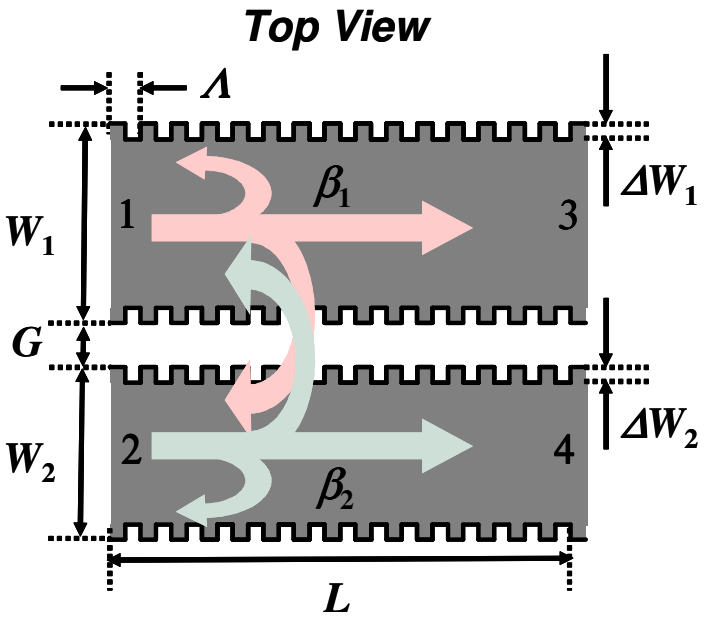

Fig. 2.2 Schematic diagram of the WSC with VG structure.

(W_1 and W_2) and grating depths (ΔW_1 and ΔW_2) but same grating period Λ. In this structure, we have three Bragg conditions as follows [22],

$$2\beta_1 = \frac{2\pi}{\Lambda}, \tag{2.12}$$

$$2\beta_2 = \frac{2\pi}{\Lambda}, \tag{2.13}$$

$$\beta_1 + \beta_2 = \frac{2\pi}{\Lambda}, \tag{2.14}$$

where β_1 and β_2 are the propagation constants for WG1 and WG2, respectively. Eq. (2.12)-(2.14) represent the backward coupling in WG1, the backward coupling in WG2, and the cross coupling between WG1 and WG2, respectively. We perform the following process to design the device: (a) allocate the three Bragg conditions to

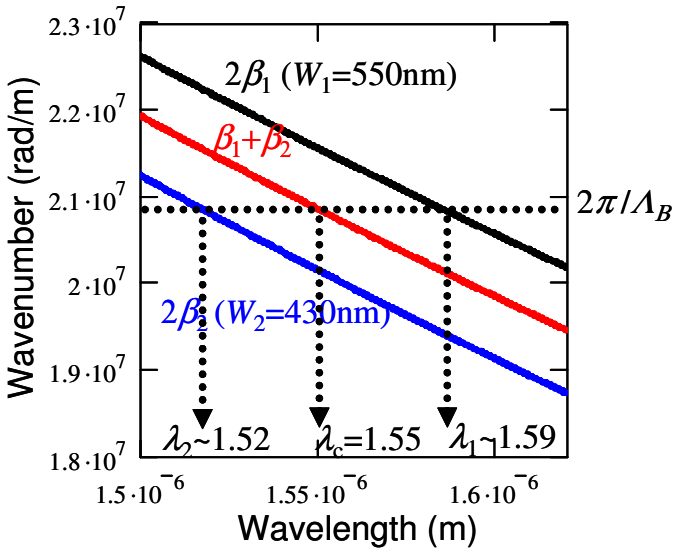

Fig. 2.3 Propagation constants calculated for TE polarization by 2D analysis with effective index method, assuming that the thickness of the silicon slab is 250nm and the silicon slab is sandwiched by silica claddings. The solid lines are the plots of the left-hand sides of the Bragg conditions, Eq. (2.12)-(2.14). The dotted horizontal line indicates the wavenumber of the grating, i.e. the right-hand sides of Eq. (2.12)-(2.14). The cross points of the solid lines and the dotted line are the three Bragg conditions.

desired wavelengths by choosing W_1, W_2 and Λ; (b) determine the coupling coefficients to achieve the desired bandwidths for the Bragg conditions using ΔW_1, ΔW_2 and G; (c) determine the length of the structure to obtain the desired extinctions. These steps are further described below.

We begin with allocating the Bragg conditions as follows. At the first step, we pick up some reasonable values of W_1 and W_2, assuming that the thickness of the silicon core is 250nm and the silicon core is surrounded by silica cladding. In this specific example, we take W_1 = 550nm and W_2 = 430nm, and calculate β for transverse electric (TE) polarization by 2D analysis with effective index method (the effect of the grating on the propagation constants is neglected). The solid lines in Fig. 2.3 are the plots of the left-hand sides of the Bragg conditions, Eq. (2.12)-(2.14). The dotted

horizontal line in Fig. 2.3 indicates the wavenumber of the grating, i.e. the right-hand sides of Eq. (2.12)-(2.14). Therefore, the cross points of the solid and the dotted lines provide the three Bragg conditions. We now calculate Λ_B to set a specific wavelength at cross coupling (λ_c=1.55μm for this example) using Eq. (2.14) as, $\Lambda_B = 2\pi/\{\beta_1(\lambda = 1.55\mu m) + \beta_2(\lambda = 1.55\mu m)\} = 301nm$. With this value of Λ_B, we find the corresponding wavelengths, λ_1 and λ_2 for the other Bragg conditions of Eq. (2.12) and (2.13), and check if these are at the desired wavelengths. In our design example, we tried to allocate these backward couplings outside the C-band and indeed these wavelengths locate outside C-band with this design (λ_1 ~ 1.52μm and λ_2 ~ 1.59μm). Note that these stop-bands may be also used for band-stop filters together with the cross coupling. If the designed Bragg wavelengths are not appropriate, then we repeat the above procedure until the desired Bragg conditions are satisfied.

Next, we determine the coupling coefficients and the length of the device. The coupling coefficients are given by the following formulas using the coupled mode theory [22, 23],

$$\kappa_1 = \frac{\varepsilon_0 \omega}{4} \left\langle E_1 \left| \Delta n_g^2 \right| E_1 \right\rangle, \tag{2.15}$$

$$\kappa_2 = \frac{\varepsilon_0 \omega}{4} \left\langle E_2 \left| \Delta n_g^2 \right| E_2 \right\rangle, \tag{2.16}$$

$$\kappa_c = \frac{\varepsilon_0 \omega}{4} \left\langle E_1 \left| \Delta n_g^2 \right| E_2 \right\rangle, \tag{2.17}$$

with

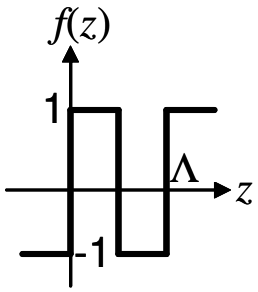

Fig. 2.4 Periodic function $f(z)$ used for calculating the coupling coefficients

$$\Delta n_g^2 = \begin{cases} -\left(n_{core}^2 - n_{clad}^2\right)\dfrac{f(z)+1}{2} & \text{in grating region} \\ 0 & \text{otherwise} \end{cases}, \qquad (2.18)$$

where κ_1, κ_2 and κ_c are the coupling coefficients for the backward coupling in WG1, the backward coupling in WG2 and the cross coupling between WG1 and WG2, respectively; ε_0 is the vacuum permittivity; ω is the angular frequency of light; E_1 and E_2 are the field distributions in WG1 and WG2 which are calculated for TE polarization again using 2D effective index method; Δn_g indicates the index perturbation which has values only at the grating region; n_{core} and n_{clad} are the silicon core effective index, 2.96 and the silica cladding refractive index, 1.4; $f(z)$ is a periodic function shown in Fig. 2.4, where z is the coordinate along the grating waveguide. Intuitively, the larger the modulation (i.e. larger ΔW_1 and ΔW_2) and the field overlap (i.e. smaller W_1, W_2 and G), the larger the coupling coefficients. For known coupling coefficients, we can estimate the coupling bandwidths, $\Delta\lambda_i = \lambda^2|\kappa_i|/\pi n_{eff}$ and the corresponding Bragg lengths, $L_{Bi} = 1/|\kappa_i|$, where i = 1, 2, c and n_{eff} is the effective index for WG1 or WG2 for the backward couplings, but the average effective index is used for the cross coupling. Fig. 2.5 shows the plots of the bandwidth $\Delta\lambda_c$ and Bragg

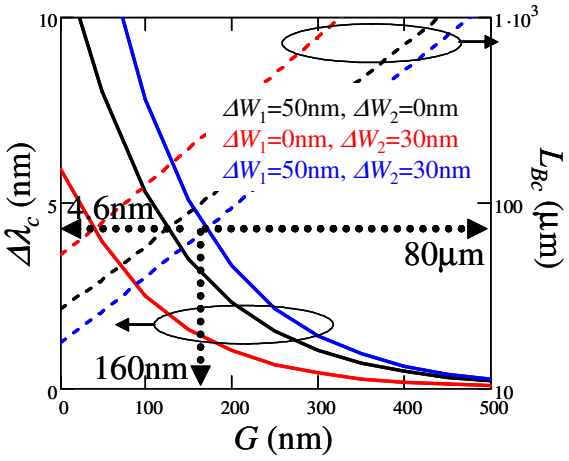

Fig. 2.5 Plots of the bandwidth $\Delta\lambda_c$ and Bragg length L_{Bc} for cross coupling with relation to the gap G, for several grating depths, ΔW_1 = 50nm and ΔW_2 = 0nm; ΔW_1 = 0nm and ΔW_2 = 30nm; ΔW_1 = 50nm and ΔW_2 = 30nm.

length L_{Bc} for cross coupling with relation to the gap G, for several grating modulation depths, (i) ΔW_1 = 50nm and ΔW_2 = 0nm, (ii) ΔW_1 = 0nm and ΔW_2 = 30nm, and (iii) ΔW_1 = 50nm and ΔW_2 = 30nm. We observe that a larger grating depth and a smaller gap give a wider bandwidth and a shorter Bragg length. Here, we take ΔW_1 = 50nm and ΔW_2 = 30nm. And since in our electron beam (e-beam) writing system, the writing field with enough high resolution and without stitching function is limited by around 100μm^2, we determine the length of WSC as L_{Bc} = 80μm for this example. Thus, we have G = 160nm and $\Delta\lambda_c$ = 4.6nm from Fig. 2.5. We can reduce the bandwidth by increasing the gap or decreasing the modulation depth of the gratings. But in both cases, a longer interaction length is required for the same extinction. Note that a higher extinction and suppressed sidelobes will require a longer grating length than Bragg length and apodization of the grating [21, 22], however, we focus on demonstrating the coupling function as these advanced designs are not in the scope of this section.

We performed 2D finite difference time domain (FDTD) simulations (See Fig. 2.6) to validate the device structure designed above which is summarized in the schematic diagram of Fig. 2.6(a). Due to the limited accuracy of the analytic effective index method, we have adjusted the grating period to 305nm to assure operation at 1.55μm. Fig. 2.6(b) and (c) show the calculated spectra in the output ports for light incident in Port1 and Port2, respectively, with the designed bands indicated by green area. We can see that the backward couplings in WG1 and WG2, and cross coupling occur almost at the designed wavelengths with a small error due to inaccuracy of the analytic effective index method. We also note that due to the sinusoidal-shaped grating assumed in the FDTD simulation, the coupling coefficients are slightly higher than that of the square-shaped grating in the analysis as observed from the wider bandwidths and the higher extinction of the cross coupling than that for the Bragg length in the simulation results.

We fabricated the designed WSC on a silicon-on-insulator (SOI) chip using e-beam lithography and reactive ion etching (RIE) with nickel hard mask process (see Fig. 2.7). The fabrication processes are described in Appendices A.1. Fig. 2.7(a) shows the optical microscope image of the whole fabricated device whereas Fig. 2.7(b) shows the SEM micrograph of the magnified small area indicated in Fig. 2.7(a). We experimentally measured the transmission spectrum with the light incident on Port1 (see Fig. 2.7(c)). The backward coupling in WG1 and the cross coupling occur at the desired wavelengths, whereas the extinction was less than those predicted by the simulation. We attribute the smaller extinction to the reduced coupling coefficient due

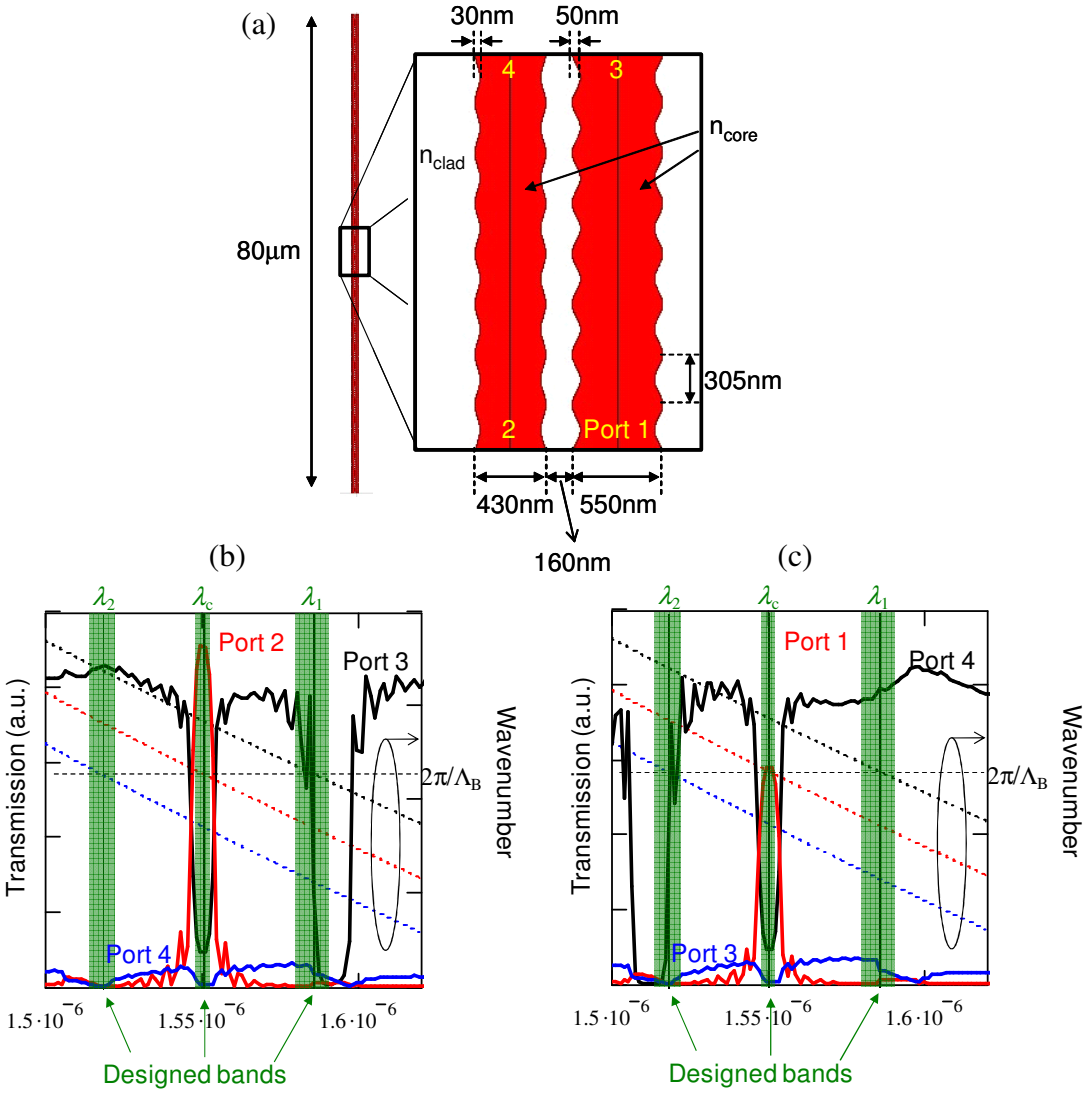

Fig. 2.6 (a) Geometry of the designed device; (b) and (c) Spectra at the output ports calculated by 2D FDTD, when the incident light is introduced into Port1 and Port2 respectively.

to the incomplete uniformity (e.g. period fluctuation, sidewall roughness) and the incomplete dimensions of the gratings and the waveguides. The Fabry-Perot oscillation in the measured spectrum is found to be from the e-beam stitching error according to the FSR of the oscillation. The small extinction can be increased by an improved fabrication and/or by a longer grating. Note that our device has very large

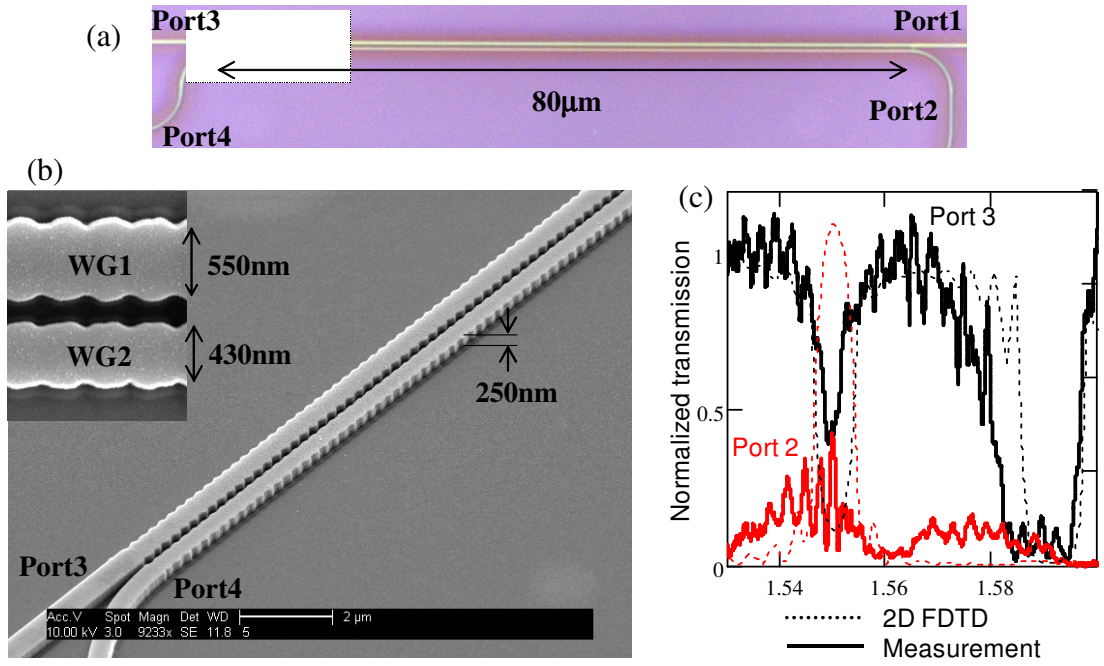

Fig. 2.7 (a) Optical microscope image of the fabricated WSC device; (b) SEM micrograph of the area indicated by the shaded area in (a); (c) Measured transmission spectra with the input light introduced into Port1.

free spectral range supporting the total bandwidth of about 70nm used in WDM systems, whereas the FSR of a ring resonator implementation is limited to about 20nm for typical ring designs with radius of about 5µm [8].

Finally, we briefly discuss the applications of WSC. We could configure a multi-port add-drop device by adding another VG waveguide and cascading the devices (see Fig. 2.8(a)). When we add another VG waveguide with different waveguide width as shown in the magnified view of Fig. 2.8(a), another cross coupling happens at a corresponding wavelength. Fig. 2.8(b) shows the 2D FDTD simulation result for the dimensions given in Fig. 2.8(a). We observe additional cross coupling at about 1.53µm. The WSC structure can be also used in a ring resonator to

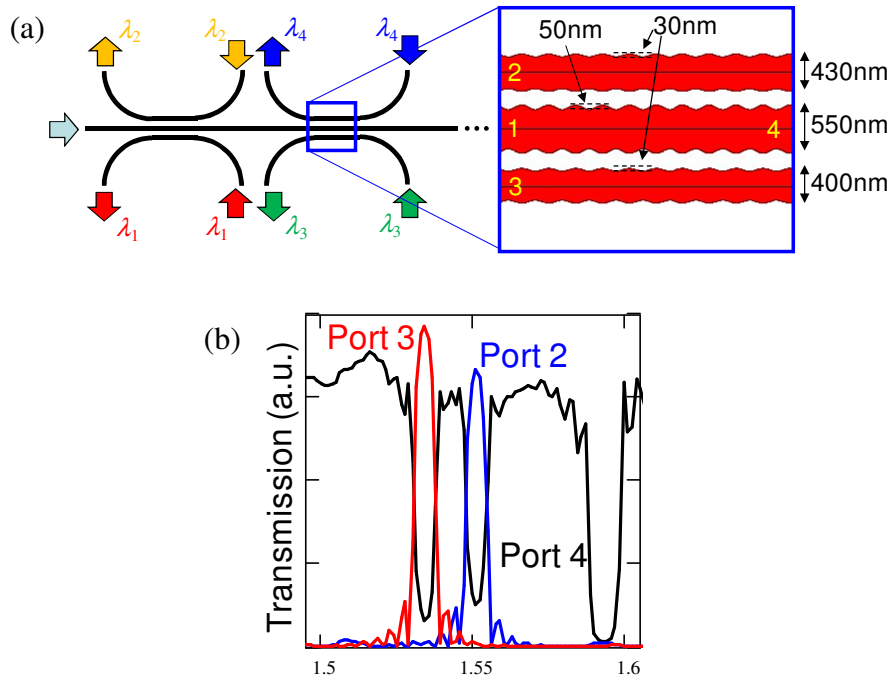

Fig. 2.8 (a) Schematic diagram of multi-port add-drop device with adding another waveguide and cascading the WSC; (b) 2D FDTD simulation results for the transmission spectrum to the output ports.

select a single resonant mode from multiple resonant modes. Ring resonators generally have multiple resonant modes and they limit the WDM bandwidth when it is used in WDM systems. Fig. 2.9(a) shows a mode-selected ring resonator with the WSC. Outside of the cross coupling window, the incident light couples in the ring and just passes through without any feedback. Therefore, the transmission has only two backward couplings for each grating. However, within the cross coupling window, the loop becomes a ring resonator due the feedback from the WSC and if the field inside the ring is in-phase, then we have a resonant mode. Fig. 2.9(b) is 2D FDTD simulation result for the structure in Fig. 2.9(a) and we see the two backward couplings and a single resonant mode selected among the multiple ring resonant modes within the

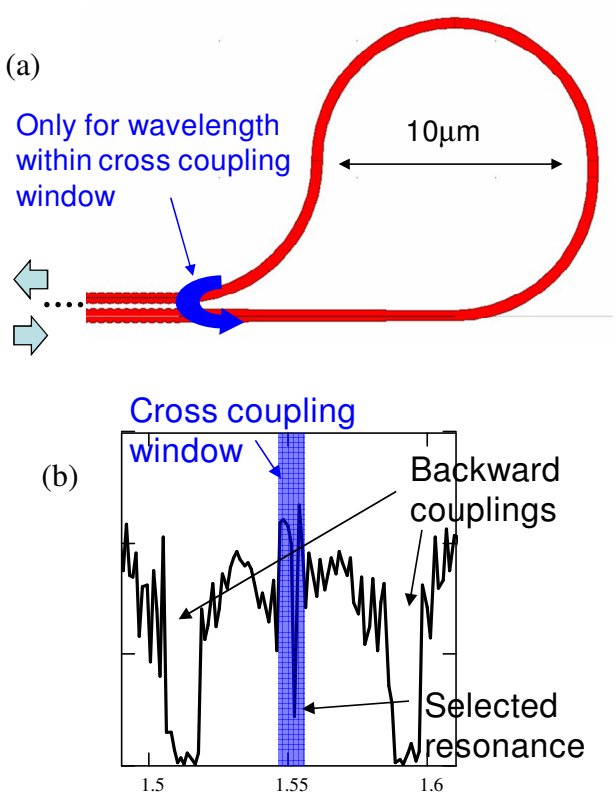

Fig. 2.9 (a) a mode-selected ring resonator with WSC; (b) transmission spectrum for the design in (a) calculated by 2D FDTD.

cross coupling window. Thus, we can select a single resonant mode using the WSC and the WDM bandwidth is not limited by the FSR of the ring. Also note that since the designed cross couplings happen for only TE-like mode in the rectangle waveguides, this structure can be an on-chip polarization beam splitter.

2.4 Summary

In this second introductory chapter, we formulated several optical resonant structures categorized into localized feedback structures and distributed feedback structures. The mathematical expressions of these structures are used to analyze their nonlinear responses in the following chapters. Also, we discussed an application of the

distributed feedback structure as a new type of device useful for on-chip scale PIC. We introduced a WSC using VG structure on a silicon chip, and gave the operation principle and the analytic design procedure. The transmission spectra expected by the procedure agreed with FDTD simulation results. We also fabricated the designed WSC and demonstrated the expected operation. The available WDM bandwidth of this device is not limited by FSR as in ring resonators.

Chapter 2, in part, is a reprint of the material as it appears in:

- K. Ikeda, M. Nezhad and Y. Fainman, "Wavelength selective coupler with vertical gratings on silicon chip," Appl. Phys. Lett. 92, 201111 (2008).

The dissertation author was the primary investigator and author of this paper. The co-authors listed in the publication assisted and supervised the research which forms the basis for this chapter.

Chapter 3

Analysis of Nonlinear Switching in Optical Micro-resonators

In this chapter, we first analyze the nonlinear switching in a silicon micro-resonator, in particular, how the switching works considering the free carrier nonlinearity excited via TPA and the Kerr nonlinearity. Next, the analysis is extended to the discussion of if it is possible to obtain switching based on Kerr nonlinearity in silicon micro-resonators with any specific structure design. Specifically, we present material and structural criteria for ultra-fast Kerr nonlinear switching in optical resonant cavities and find that insulators with a wider band-gap such as silicon dioxide and silicon nitride will be interesting materials to investigate for this purpose.

3.1 Free-carrier Effect vs. Kerr Effect in Silicon Micro-resonators

In this section, we introduce a simple analysis of the nonlinear response in a Fabry-Perot resonator realized with a 2D PhC waveguide on silicon, considering the

effects from two-photon-excited free carrier nonlinearity and Kerr nonlinearity operating at a pump wavelength of 1.55μm. In particular, for given linear parameters of the resonator, an analytic procedure is presented to predict the required optical pump energy for a desired modulation depth. In the meantime, we compare the strengths of the free-carrier nonlinearity and the Kerr nonlinearity in the silicon resonant structure.

Consider a simple model described in the diagram of Fig. 3.1, where the two mirrors with the amplitude reflectance r, the amplitude transmittance t and the amplitude scattering loss s are placed at $z = 0$ and $z = L$. We assume that the waveguide between them has the material index n and the corresponding group index n_g (equivalently group velocity v_g). We also assume that the refractive index n changes due to the nonlinear Kerr effect $n_2 I$ and due to the Drude effect via free carrier generation by TPA $n_d I^2$, yielding,

$$n = (n_0 - jn'_0) + n_d I^2 + (n_2 - jn'_2) I \,, \tag{3.1}$$

where n_0 and n_0' are the real and the imaginary part of the linear refractive index of the waveguide material, respectively, n_2 and n_2' are the real and imaginary part of the nonlinear refractive index due to the Kerr nonlinearity, respectively. Assuming a Gaussian shape pump pulse with the FWHM τ_p and the angular frequency ω_p, the value of n_d can be expressed for the time scale much shorter than the carrier lifetime as [24],

$$n_d = \frac{-e^2}{2n_0\omega_s^2 m^* \varepsilon_0} \frac{\tau_p \sqrt{\pi}}{\sqrt{4\ln 2}} \frac{\beta}{2\hbar\omega_p}, \tag{3.2}$$

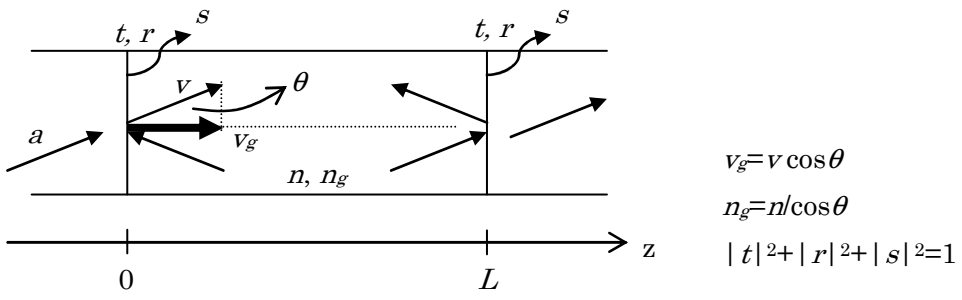

Fig. 3.1 Schematic diagram describing the analytic model for Fabry-Perot resonator in a large group index waveguide.

where e is the electron charge, ω_s is the angular frequency of the signal, m^* is the effective mass of electrons and holes (=0.16m_0, with m_0 being mass of the electron), ε_0 is the vacuum permittivity and β is the TPA coefficient. The propagation constant for the field inside the waveguide shown in Fig. 3.1 is given by,

$$k = k_0 n_g = k_0 \frac{n}{\cos\theta}, \tag{3.3}$$

where k_0 is the free space wavenumber, θ is the angle between the waveguide direction and the direction of the ray's phase velocity. The zigzag ray picture for group index is valid for the strongly confined waveguide where the effect of Goos-Haenchen shift can be neglected [25], which will be the case for a 2D PhC waveguide when neglecting the small dispersion from the material and the vertical index guiding. Substituting Eq. (3.1) into Eq. (3.3) yields,

$$\begin{aligned} k &= \frac{k_0}{\cos\theta}\left(n_0 + n_d I^2 + n_2 I\right) - j\left(\frac{\alpha + \beta I}{2\cos\theta}\right), \\ &\equiv \kappa - j\mu \end{aligned} \tag{3.4}$$

where $\alpha = 2k_0n_0$' is the attenuation coefficient that includes losses due to single-photon absorption and waveguide loss, and $\beta = 2k_0n_2$' is the TPA coefficient already defined. Here, we also defined κ and μ as the real and imaginary part of the propagation constant. A large value of n_g (or large θ) can be achieved using a PhC waveguide [26] and we apply our theory to the PhC micro-resonator later. Using the electric field inside the cavity $E(z)$ in Eq. (1.1), we find the intensity of the field inside the cavity $I(z) = |E(z)|^2$ normalized to the intensity of the input field $|a|^2$,

$$\frac{I(z)}{|a|^2} = \frac{e^{-2\xi(z)} + R^2 e^{-4\xi(L)} e^{2\xi(z)} + 2R \cdot e^{-2\xi(L)} \cos 2\left(\phi(L) - \phi(z)\right)}{1 - 2R^2 e^{-2\xi(L)} \cos 2\phi(L) + R^4 e^{-4\xi(L)}} (1 - S^2 - R^2), \quad (3.5)$$

where we assumed real values for the reflectance $r = R$ and the scattering loss $s = S$, and the phase $\phi(z)$ and the attenuation $\xi(z)$ are given by,

$$\phi(z) = \int_0^z \kappa(z')dz' = \frac{k_0 n_0 z}{\cos\theta} + \frac{k_0}{\cos\theta}\left(n_d \int_0^z I^2(z')dz' + n_2 \int_0^z I(z')dz' \right), \quad (3.6)$$

$$\xi(z) = \int_0^z \mu(z')dz' = \frac{\alpha z}{2\cos\theta} + \frac{\beta}{2\cos\theta} \int_0^z I(z')dz'. \quad (3.7)$$

Eq. (3.5) can be solved for I together with Eq. (3.6) and (3.7), as $\phi(z)$ and $\xi(z)$ depend on I in the nonlinear regime. The resulting solution will be multi-valued, indicating that the resonator will become bistable [27], when the pump has a wavelength (or phase) detuned from the resonance and the input intensity $|a|^2$ is large enough. The solutions are graphically described in Fig. 3.2(a) by schematically plotting the left-hand-side (LHS) which is a straight line with the tilt $1/|a|^2$ and the right-hand-side (RHS) which is the same curve as the cavity spectrum, of Eq. (3.5) with regard to I. If

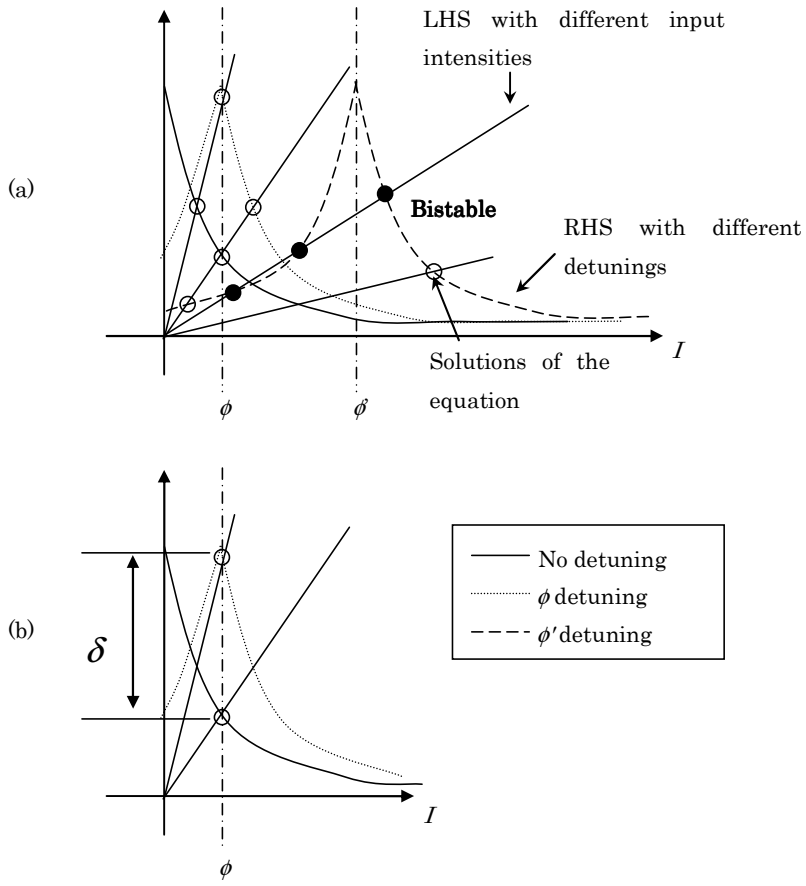

Fig. 3.2 Schematic plots of LHS and RHS of Eq. (3.5): (a) Solutions (circles) for various input intensities and phase detunings, (b) Two solutions for a fixed modulation depth.

the pump is at the resonant wavelength, i.e., with no phase detuning (the first term of Eq. (3.6) at $z = L$ is zero), we obtain a single valued solution (see the cross points in Fig. 3.2(a) for no detuning) and the solution increases nonlinearly as the input intensity $|a|^2$ increases. If the pump wavelength is with a small phase detuning ϕ (the first term of Eq. (3.6) at $z = L$ is not zero), then the solution is still single valued, and as the input intensity increases it increases following the resonant curve. However, when the pump wavelength is with a large phase detuning ϕ', then there will be three

solutions at some value of the input intensity. As the input intensity increases, the solution is at first single valued and gradually increases. After the straight line of the RHS crosses the peak of the resonant curve of the LHS, the solution becomes triple valued and the physical solution is the smallest (largest) point for the ascending (descending) of the pump pulse. Finally, after the crossing point of the smallest (largest) solution vanishes, the physical solution jumps to the largest (smallest) value and becomes again single valued. If we compare the solutions with no detuning to that with a detuning of ϕ in Fig. 3.2(b), the required input intensity $|a|^2$ for ϕ detuning is smaller than that for no detuning (see the tilt difference of the straight lines), in order to have the same modulation depth δ and same phase shift ϕ. Thus, with an appropriate phase detuning, the required input intensity can be significantly reduced. By solving Eq. (3.5), we can easily predict the optimum pump phase detuning and the required pump power for switching operation using the material parameters and the measured linear parameters of the device.

We first simplify the integral equations of Eq. (3.5)-(3.7) by removing the z dependence in I. We assume that the phase and the loss inside the cavity are independent of z as,

$$\phi(z) = m\pi\,, \quad \xi(z) = \frac{1}{2}\xi(L)\,. \tag{3.8}$$

With this assumption, we can use the position-independent intensity I_p, which represents the peak intensity inside the cavity with the loss at the center of the cavity, instead of $I(z)$ in Eq. (3.5)-(3.7). Thus, we can simplify the integrals in Eq. (3.6) and Eq. (3.7) as,

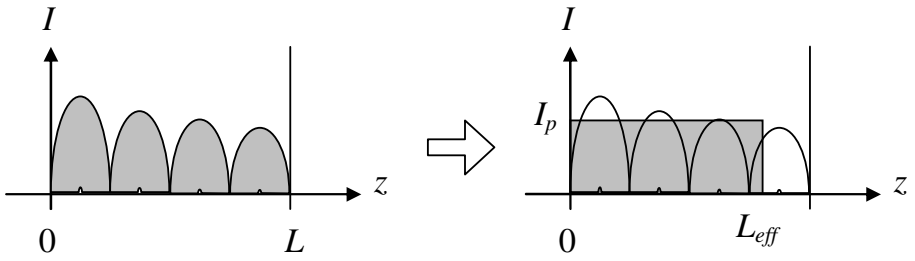

Fig. 3.3 Approximation of Eq. (3.5)-(3.7) with Eq. (3.8)-(3.11).

$$\phi(L) = \frac{k_0 n_0 L}{\cos\theta} + \frac{k_0}{\cos\theta}\left(n_d I_p^2 L_{eff\,2} + n_2 I_p L_{eff\,1}\right) \equiv \phi_0 + \phi_1 I_p + \phi_2 I_p^2, \tag{3.9}$$

$$\xi(L) = \frac{\alpha L}{2\cos\theta} + \frac{\beta}{2\cos\theta} I_p L_{eff\,1} \equiv \xi_0 + \xi_1 I_p, \tag{3.10}$$

where the effective length L_{eff1} and L_{eff2} are given by the corresponding equations,

$$L_{eff\,1} = \frac{\int_0^L I(z')dz'}{I_P}, \qquad L_{eff\,2} = \frac{\int_0^L I^2(z')dz'}{I_P^2} \qquad \text{with } \beta = n_d = n_2 = 0. \tag{3.11}$$

The assumption of linearity condition is reflected in $\beta = n_d = n_2 = 0$ when obtaining L_{eff1} and L_{eff2}. In Eq. (3.9) and (3.10), we also defined the constant phase (or phase detuning) ϕ_0, the linear phase coefficient ϕ_1, the quadratic phase coefficient ϕ_2, the constant loss ξ_0 and the linear loss coefficient ξ_1. Fig. 3.3 shows the above approximation schematically. Note that with approximation of $e^x \sim 1 + x$ and $\cos 2x \sim 1 - 2x^2$ that are appropriate for a high finesse and low loss cavity mode, Eq. (3.5) reduces to 6th order algebraic equation for I_p.

Next we compare our analysis with the experimental data from Ref. [15] where linear parameters of a PhC micro-resonator and the nonlinear operation were

Table 3.1 Parameters extracted from the resonator and pump pulse in Ref. [15], and the estimated parameters.

Extracted parameters	Estimated parameters
Resonant wavelength λ_r = 1547.68nm	Group index (from λ_r and *FSR*) n_g = 15.2
Free spectrum range *FSR* = 37.58nm	Amplitude reflectance (from $\Delta\lambda$ and α(dB)) *R* = 0.9974
FWHM of the resonant mode $\Delta\lambda$ = 0.084nm	Finesse (from $\Delta\lambda_r$ and *FSR*) *F* = 447
Waveguide loss α(dB) = 1dB/mm	Effective cavity length (from n_g, n_0 and L_a) *L* = 7.34μm
Cavity length L_a = 1.68μm	
Core area A_{eff} = 0.145μm^2	
Pump pulse time duration τ_p = 7.3ps	

measured. We use the following measured parameters for the linear regime of operation: the resonant wavelength λ_r = 1547.68nm (= λ_s = λ_p, for the degenerate case), the free spectrum range of *FSR* = 1568.05 − 1530.47 = 37.58nm, the FWHM of the resonant mode $\Delta\lambda$ = 0.084nm, the waveguide loss α(dB) = 1dB/mm [28], the cavity length of $L_a = 4 \times 0.42 = 1.68\mu m$ and the core area of $A_{eff} = 0.2 \times 3^{1/2} \times 0.42 = 0.145\mu m^2$. Note that we here picked up the *FSR* from the sample B to estimate the group index for the PhC waveguide while the other parameters are from the sample A whose nonlinear response is presented in detail. We estimate the following values (i) the group index $n_g = \lambda_r^2/\{2(5 \times 0.42\mu m)FSR\} = 15.2$ and (ii) the reflectance *R* = 0.9974 from $\Delta\lambda$ and α(dB) as in Eq. (2.11). *S* is set to zero. The above extracted and

estimated parameters of the resonator are summarized in Table 3.1. The finesse and the effective cavity length in Table 3.1 are used in the next section. We assumed the material parameters of $n_0 = 3.46$, $n_2 = 0.45 \times 10^{-13}\text{cm}^2/\text{W}$ and $\beta = 0.8\text{cm/GW}$ [29]. To predict the nonlinear operation, we first calculate $n_d = -4.7 \times 10^{-31}\text{m}^4/\text{W}^2$ with τ_p = 7.3ps which was used in the experiment in Ref. [15]. After estimating ϕ_1, ϕ_2, ξ_0 and ξ_1 in Eq. (3.9) and (3.10) with $L_{eff1} \sim L_{eff2} \sim L_a$, we use Mathcad to solve the 6th order algebraic equation approximating Eq. (3.5) (see Fig. 3.4). Specifically, Fig. 3.4(a) shows plots of LHS and RHS of Eq. (3.5) with different input powers and different wavelength detunings $\lambda_0 = -\phi_0\lambda_r^2/(2\pi n_g L_a)$. Comparing to Fig. 3.2(a), we can see small red shifts due to the Kerr effect at a low power and resonant peak degradations due to TPA in RHS curves. Fig. 3.4(b) shows the wavelength shift with regard to the input peak power for different values of λ_0. For 0.084nm of wavelength shift corresponding to the FWHM of the resonant mode, the required input power is 9.5mW with the detuning of $-0.82\Delta\lambda$, corresponding to 7.3ps × 9.5mW = 69.4fJ. The experimental value in Ref. [15] was 100fJ and the effectively coupled energy to the cavity was estimated as 10fJ to take into account the broad spectrum of the pump pulse and the transmission bandwidth of the cavity. Consequently, our estimated analytic value is close to the experimental results, with error due to the uncertainty in the values of waveguide loss, group index and mode volume. According to our dimensions, the volume may be simply calculated as $V = A_{eff} \times L_a = 0.24\mu\text{m}^3$ which is however three times larger than its mode volume of $0.07\mu\text{m}^3$ given in Ref. [15]. If we use the volume of $V/3$ with $(1/3)^{2/3}A_{eff}$ and $(1/3)^{1/3}L_a$, the required pump power is

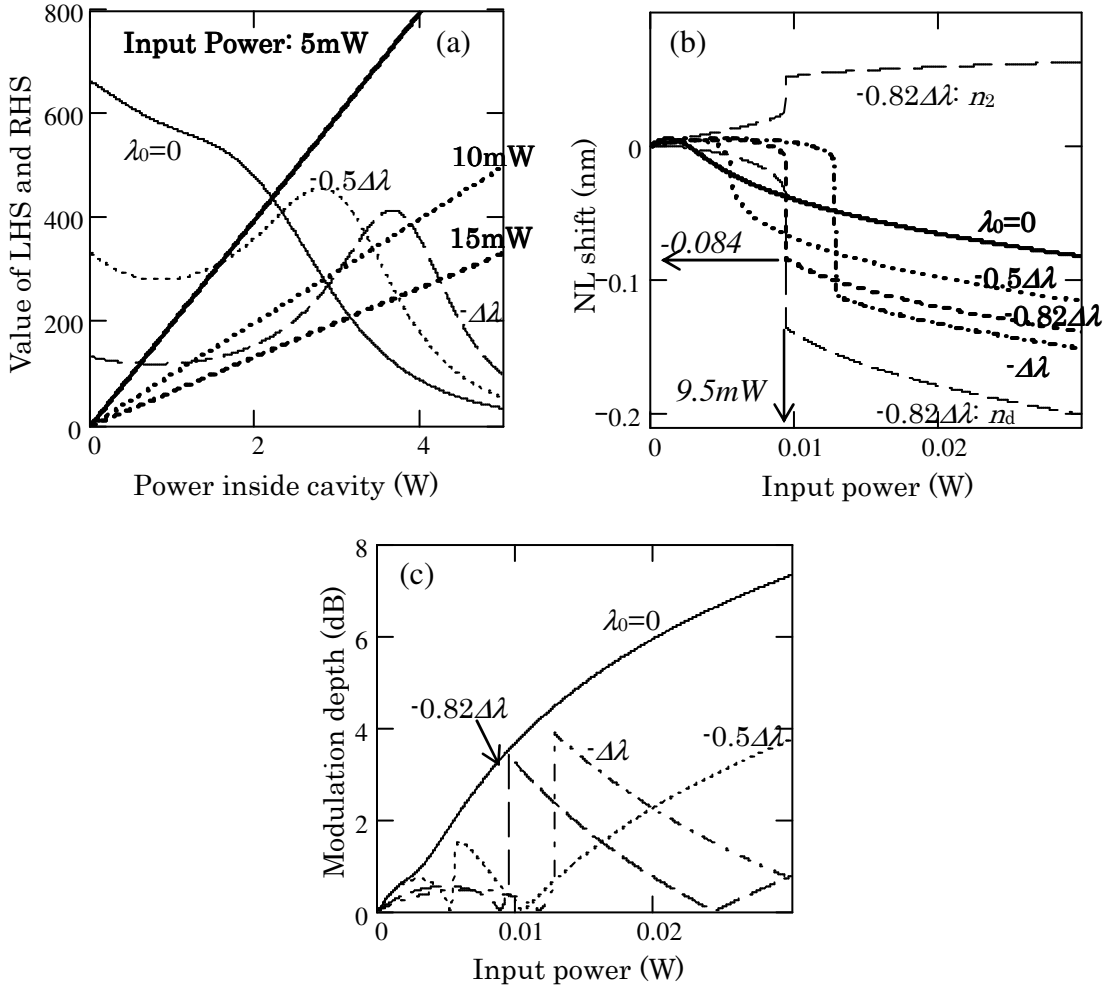

Fig. 3.4 Plots of the solutions of Eq. (3.5) for data from Ref. [15]. (a) Plots of LHS and RHS of Eq. (3.5) with relation to the power inside the cavity for various input peak powers and wavelength detunings, (b) Nonlinear phase shift and (c) modulation depth with relation to the input peak power for various wavelength detunings.

calculated as 3.3mW leading to the pump energy of 24.1fJ, which will be more accurate. In Fig. 3.4(b), the portions originating from Kerr effect (n_2) and Drude effect (n_d) are also separately drawn for $\lambda_0 = -0.82\Delta\lambda$, which indicates the Drude effect overcomes the Kerr effect. Fig. 3.4(c) can be used to obtain the modulation depth. Because of the significant peak degradation from TPA as seen in Fig. 3.4(a), the

reduction of the required pump power explained in Fig. 3.2(b) is not observed and zero phase detuning is optimum for a higher modulation depth in this case. The above procedure could be applied in the same way to any other cavity structures such as a ring resonator using its analytic expression (e.g. Eq. (2.1)) for the internal intensity instead of that in Eq. (3.5).

3.2 Material and Structural Criteria for Ultra-fast Kerr Nonlinear Switching in Optical Resonant Cavities

In the previous section, it has been shown analytically that the switching operation in a silicon micro-resonator originates from the free carrier refraction excited by TPA that overcomes the ultrafast Kerr nonlinear refraction. The same happens in a GaAs micro-resonator [30]. Alternatively, Kerr nonlinearity in AlGaAs micro-resonators was considered (without a proof) by simply assuming that the photon energy at 1.55 μm (0.8eV) is below the half-bandgap of the material [31]. Suitability of a specific optical material for realization of Kerr nonlinear optical devices with non-resonant [32] or resonant [33] geometry was evaluated using a nonlinear figure of merit (FOM) that includes only the effect from the loss due to TPA process. However, as described above, the dominant nonlinear effect in the demonstrated resonant devices is in practice the free carrier refraction, which prevents the devices from the ultra-fast operation under Kerr nonlinearity and thus the TPA is less significant than the free carrier refraction in the resonator-enhanced switching. In this section, we include the free carrier refraction and define a new nonlinear FOM for characterization of ultrafast Kerr nonlinear materials in resonant cavities and a structural criterion for

design of such nonlinear devices. This way, we could find the answer for our first question of if it is possible to obtain switching based on Kerr nonlinearity in silicon micro-resonators with any specific structure design.

For ultra-fast nonlinear operations, the refractive index change from Kerr nonlinearity has to be much larger than that from free carrier nonlinearity excited through *n*-photon absorption. If we use the Drude model for the refractive index change due to free carrier effect, this condition can be described by $|n_2|I >> |n_d^{(n)}|I^n$ or,

$$\frac{|n_2|}{|n_d^{(n)}|} >> I^{n-1}, \tag{3.12}$$

where $|n_2|I$ is the refractive index change from Kerr nonlinearity, I is the intensity inside the resonant cavity, n_2 is the nonlinear refractive index of the material and $n_d^{(n)}$ is given by,

$$n_d^{(n)} = \frac{-e^2}{2n_0\omega_s^2 m^* \varepsilon_0} \frac{\tau_p\sqrt{\pi}}{2\sqrt{n\ln 2}} \frac{\beta^{(n)}}{n\hbar\omega_p} \equiv c_d^{(n)} \frac{\tau_p}{n_0\omega^3}, \tag{3.13}$$

assuming a Gaussian shaped pump pulse with the FWHM τ_p and the angular frequency ω_p, where τ_p is much shorter than the carrier lifetime. Here, e is the electron charge, ω_s is the angular frequency of the signal, m^* is the conductivity effective mass of electrons and holes [$= (1/m_{ce} + 1/m_{ch})^{-1}$, with m_{ce} and m_{ch} being conductivity effective mass of electrons and that of holes, respectively], ε_0 is the vacuum permittivity, n_0 is the refractive index of the material and $\beta^{(n)}$ is the *n*-photon absorption coefficient. For our future discussions, we also assumed that $\omega \sim \omega_s \sim \omega_p$ in Eq. (3.13) (pump and signal pulses are both at a wavelength of about 1.55μm) and

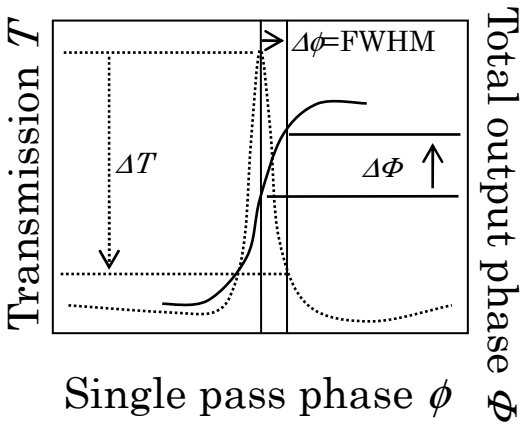

Fig. 3.5 Schematic plots of the transmission T and the total output phase Φ of a resonant mode with relation to the single pass phase ϕ. With the single pass phase shift $\Delta\phi \sim$ FWHM, a large transmission modulation ΔT and a large total output phase $\Delta\Phi$ are introduced.

defined the coefficient $c_d^{(n)}$,

$$c_d^{(n)} \equiv \frac{-\sqrt{\pi} e^2 \beta^{(n)}}{4\hbar m^* \varepsilon_0 n \sqrt{n \ln 2}}. \tag{3.14}$$

In addition, the n_2-induced nonlinear phase shift must be at least larger than the FWHM of a resonant cavity mode in single pass phase $\Delta\phi$, in order to introduce a large enough intensity modulation ΔT or total phase shift $\Delta\Phi$ at the output of the resonator (See Fig. 3.5). That is $2\pi n_2 |I| L/\lambda \sim \Delta\phi$ or,

$$I \sim \frac{\lambda}{|n_2| FL}, \tag{3.15}$$

where λ is the signal wavelength in vacuum and F and L are the finesse and the roundtrip length of the resonant cavity, respectively. The finesse F will be slightly degraded by TPA in nonlinear regime and so the F could be replaced by the value at a

high intensity irradiation for more precise characterization. Substitution of Eq. (3.13) and (3.15) into (3.12) yields,

$$(FL)^{n-1} >> \frac{\left|c_d^{(n)}\right|(2\pi c)^{n-1}\tau_p}{\left|n_2\right|^n n_0 \omega^{n+2}}. \tag{3.16}$$

The left-hand side of Eq. (3.16) is determined by the cavity design, whereas the right-hand side is determined by the material parameters at the operation wavelength of the device and the pump pulse time duration corresponding to the operation speed of the device. Therefore, Eq. (3.16) is one of the design criteria for a resonant cavity to operate under the ultra-fast Kerr nonlinearity. Another important consideration is that the pulse duration τ_p should be longer than the cavity lifetime τ_c for the fields inside the cavity to coherently interfere and to create the nonlinear enhancement of intensity and phase. That is $\tau_p > \tau_c$ or,

$$\frac{2\pi c\tau_p}{n_0} > FL. \tag{3.17}$$

From Eq. (3.16) and (3.17), we obtain a universal criterion for the resonant cavity to operate in ultra-fast Kerr nonlinear regime:

$$\left(\frac{2\pi c\tau_p}{n_0}\right)^{n-1} > (FL)^{n-1} >> \frac{\left|c_d^{(n)}\right|(2\pi c)^{n-1}\tau_p}{\left|n_2\right|^n n_0 \omega^{n+2}}. \tag{3.18}$$

We can extract from Eq. (3.18) a nonlinear optical material criterion,

$$\left(\frac{2\pi c\tau_p}{n_0}\right)^{n-1} >> \frac{\left|c_d^{(n)}\right|(2\pi c)^{n-1}\tau_p}{\left|n_2\right|^n n_0 \omega^{n+2}}, \tag{3.19}$$

and define a new nonlinear FOM for *n*-photon process as,

$$FOM^{(n)} \equiv \frac{\left|n_2\right|^n \omega^{n+2} \tau_p^{n-2}}{\left|c_d^{(n)}\right| n_0^{n-2}} >> 1. \tag{3.20}$$

The $FOM^{(n)}$ in Eq. (3.20) is determined for any material at a wavelength of interest and gives a fundamental measure of whether the material can be used as a resonantly enhanced nonlinear optical device with the ultra-fast Kerr nonlinearity. In summary, if a material satisfies Eq. (3.20), then we can use Eq. (3.18) to design the resonant device. In particular, we basically want to design a cavity operating at low input powers and at high speed. This design leads to a large finesse F for strong intensity enhancement, a long cavity length L for long interaction length, and a short pulse duration τ_p for fast operation, but limited by the left-hand side of the inequality of Eq. (3.18). Additionally, if we have a small F and L and a large τ_p imposed by fabrication process limitations or pump laser specification, the lower limit is defined by the right-hand side of the inequality of Eq. (3.18).

Table 3.2 shows the FOMs and the material parameters used to calculate our FOMs for several commonly used materials. The $FOM^{(2)}$ for Si and GaAs are 0.154 and 0.053, respectively (i.e., much smaller than 1) and cannot be used for resonantly enhanced Kerr nonlinear switch. In other word, the contribution of free carrier nonlinearity is larger than that of the ultra-fast Kerr nonlinearity and the switching speed is limited by the free carrier lifetime. Even in $Al_{0.18}Ga_{0.82}As$, the $FOM^{(2)}$ is close to or less than 1, when we are using the measured material parameters from the current literature. Note that the theory based on the two-parabolic-band approximation from Ref. [41] and [44] will not be accurate around or below the half bandgap where the $\beta^{(2)}$

Table 3.2. New FOMs and material parameters used to calculate the FOMs, for silicon (Si), gallium arsenide (GaAs), aluminum gallium arsenide (AlGaAs), and silicon dioxide (SiO_2).

Material	Si	GaAs	$Al_{0.18}Ga_{0.82}As$		$Al_{0.36}Ga_{0.64}As$		SiO_2
n_0	3.48 [a]	3.399 [b]	3.308 [c]		3.216 [c]		1.44 [d]
m_{ce}, m_{ch} ($\times m_0$)	0.26, 0.39 [e]	0.067, 0.33 [f]	0.07, 0.36 [f]		0.091, 0.40 [f]		-
n_2 (cm^2/W)	0.45×10^{-13} [g]	1.59×10^{-13} [g]	1.7×10^{-13} [h] (0.58×10^{-13} [i])		6.0×10^{-14} [j]		2.16×10^{-16} [k]
n	2	2	2	3	2	3	>10
$\beta^{(n)}$ (cm^{2n-3}/GW^{n-1})	0.79 [g]	10.2 [g]	0.37 [h] (0.14 [i])	0.05 [l]	0.007 [m]	0.09 [m]	~0 [n]
$FOM^{(n)}$	0.154	0.053	1.76 (0.542)	44.8 [o]	15.0	1.42 [o]	Very large

a: From Ref. [34], at 1.55μm.
b: From Ref. [35], at 1.55μm.
c: Linear interpolation with values of GaAs and AlAs from Ref. [36], at 1.55μm.
d: From Ref. [34], fused silica at 1.5μm.
e: From Ref. [37].
f: Γ valley minimum for m_{ce} and Γ valley in [100] for m_{ch} (heavy hole) from Ref. [38].
g: From Ref. [29].
h: From Ref. [39], at 1.55μm.
i: From Ref. [40].
j: From a rough estimation at 1760nm using the measured value for $Al_{0.18}Ga_{0.82}As$ in Ref. [39] and the scaling rule from Ref. [41].
k: From Ref. [42].
l: From Ref. [43], at 1.55μm.
m: From rough estimations at 1760nm using the measured values for $Al_{0.18}Ga_{0.82}As$ in Ref. [39] and [43], and the scaling rules from Ref. [44]
n: From Ref. [45]. A damage level intensity ($2.7\times10^{13}W/cm^2$) of 2eV (620nm) photons created a comparable free-carrier effect to Kerr effect via five-photon absorption. Thus, there should not be free-carrier effect excited via ten-photon absorption with 0.8eV (1550nm) photons at a practical power level.
o: τ_p=30ps.

vanishes in $Al_{0.18}Ga_{0.82}As$, as shown in Ref. [39] and [43]. Therefore, we used the measured values for $Al_{0.18}Ga_{0.82}As$ (and other materials as well) from those references. We believe that this is a fair treatment because we will not have a perfect bulk crystal for the real waveguide devices, which should have a higher density of surface states as well as some defect density. The $FOM^{(3)}$ for $Al_{0.18}Ga_{0.82}As$ is much larger than 1 for τ_p=30ps and the three-photon process will not limit the Kerr nonlinearity. In $Al_{0.36}Ga_{0.64}As$, since the photon energy of 0.8eV is far below the half bandgap of 0.936eV [38], the TPA almost vanishes and the $FOM^{(2)}$ is in fact much larger than 1. However, we found that in turn the $FOM^{(3)}$ became close to 1, meaning the free carriers excited via three photon absorption (ThPA) will be the limitation in $Al_{0.36}Ga_{0.64}As$. Here, since we could not find measured values for $Al_{0.36}Ga_{0.64}As$ in the literature, we estimated the values for $Al_{0.36}Ga_{0.64}As$ using the measured values for $Al_{0.18}Ga_{0.82}As$ and the scaling rules from Ref. [41] and [44], assuming that the scaling rules approximately hold around the half-band tail (See Appendices A.2 for the detail). The authors of Ref. [31] claimed that the nonlinear switching operation in their $Al_{0.36}Ga_{0.64}As$ device originates from Kerr nonlinearity. However, they did not provide evidence, such as a time-resolved measurement or a red shift of the resonant mode, and thus it may also be possible to consider that the origin is the free carrier nonlinearity. From the parameters of their experiment we find that the intensity inside the cavity is greater than $33W/0.5\mu m^2 = 66W/\mu m^2$ and the pulse time duration is 30ps. With these parameters and n_2, $\beta^{(2)}$ and $\beta^{(3)}$ of $Al_{0.36}Ga_{0.64}As$ from Table 3.2, we estimated the index shifts of 4.0×10^{-4} from Kerr effect $n_2 I$, -1.2×10^{-4} from free

carrier effect via TPA $n_d^{(2)}I^2$ and -5.6×10^{-3} from free carrier effect via ThPA $n_d^{(3)}I^3$. These estimations indicate that the contribution due to free carrier effect via ThPA will be larger than that of the Kerr effect. Conversely, for silicon dioxide (SiO_2), the FOM is almost infinite due to the negligibly small free-carrier effect [45], and therefore it can be used for implementation of resonator-enhanced nonlinear device with the ultra-fast Kerr nonlinearity. However, SiO_2 has a relatively small refractive index and a small Kerr nonlinearity and thus will not be very useful for practical realizations of micro-photonic devices on a silicon chip. For example, micro-resonators made of SiO_2 must have air cladding due to the small refractive index [46] and thus cannot be protected by a cladding material. This prevents multi-layer implementation of devices and will also result in a higher cost for a protective packaging of the devices. Therefore, identifying a new material with a large energy bandgap to decrease the TPA/ThPA or with a large Kerr nonlinearity, which is also compatible with silicon CMOS fabrication process, would be of great importance for the future applications of ultrafast Kerr nonlinearity in various resonant devices.

We apply the results obtained above to a concrete example of silicon micro-resonators used in the previous section and prove the validity of our criteria Eq. (3.18) and nonlinear FOM Eq. (3.20). We then demonstrate the design considerations to achieve an ultra-fast Kerr nonlinear switching assuming that we have a material with FOM >> 1. First, we consider the silicon photonic crystal micro-resonator experimentally demonstrated, and already used in the previous section. The parameters extracted from the fabricated device and the used pump pulse, and the

estimated values of F and L using these parameters are summarized in Table 3.1. Note that the actual length L_a=1.68μm was multiplied by the factor of n_g/n_0 taking into account the effect of the large group index n_g. Using the values in Table 3.1 and 3.2, the terms in Eq. (3.18) for TPA (n = 2) are calculated as, from the left, 3.95×10^{-3}, 6.56×10^{-3} and 26×10^{-3}, which does not satisfy the inequalities in the Eq. (3.18) and this is directly related to the fact that the $FOM^{(2)}$ of silicon is smaller than 1. Specifically, the relation of the first two values (3.95×10^{-3} and 6.56×10^{-3}) indicates that the pump pulse cannot efficiently interfere within the cavity due to the low coherence of the pump pulse. In fact, the pulse spectrum is wider than the FWHM of the resonant mode as shown in the Ref. [15]. The last value (26×10^{-3}) is much larger than the second value (6.56×10^{-3}) and this means that the free carrier nonlinearity excited via TPA overcomes the Kerr nonlinearity for a large enough nonlinear phase shift. We can see from Fig. 3.4(b) with $\lambda_0 = 0$ that the Kerr nonlinear effect (red shift) overcomes the free carrier effect (blue shift) at the small input power less than about 2mW but the resonant wavelength shift (or phase shift) at this input power is much smaller than the FWHM of the resonant mode (0.084nm) and thus is not enough for a switching operation (recall Fig. 3.5). It is obvious that at the resonant wavelength shift of 0.084nm or larger, the free carrier nonlinearity overcomes the Kerr nonlinearity. Thus, we can conclude that our criteria and nonlinear FOM are valid. Finally, we demonstrate the design consideration to achieve an ultra-fast Kerr nonlinear switching device. We assume a material that has a FOM much larger than 1. Here, we use the values from SiO_2 in Table 3.2. We also notice that silicon nitride (SiN) could be a

good material candidate because it has a larger refractive index than SiO_2 and still an enough wide bandgap, but we will look at the SiN in Chapter 5. In this case, we need to consider only the left-hand side of the inequality of Eq. (3.18). For example, if we can have the same $F = 447$ and $\tau_p = 7.3$ps as the previous example, then we will need a roundtrip cavity length to be smaller than 21μm. However, it will be difficult to obtain a resonator with such a high finesse and a small size using SiO_2 material due to its small refractive index. If we have $L = 1$mm instead, then the finesse must be smaller than 9.5 and such a resonator will be possible to construct in practice. However, the enhancement of nonlinearity (i.e. the magnification factor) should be small with such a small finesse and therefore the required input power for switching operation becomes very large.

3.3 Summary

We derived an equation that describes the nonlinear operation of a silicon Fabry-Perot resonator with large group index waveguide. Specifically, a silicon PhC micro-resonator with nonlinearities due to two-photon-excited free carrier effect and Kerr effect was assumed. The equation clearly explained the bistability of the device and the reduction of the required pump energy for a specific nonlinear phase shift or a specific modulation depth at an appropriate phase detuning from the resonance. We presented a simple procedure to predict the required optical pump energy for the modulation and the resulting modulation depth using the equation and the device parameters. Comparing to coupled mode analysis [47] or rate equation analysis [48], this procedure is straightforward to see intuitively why the bistable operation happens

or how a phase detuning and loss due to TPA affect the bistability and the device operation. Our analysis is compared with an experiment reported in the literature, and found in good agreement, indicating the validity and usefulness of our method for analysis of nonlinear resonant structures. As the result, we found that the strength of the free-carrier nonlinearity overcomes that of the ultra-fast Kerr nonlinearity in the specific silicon resonator.

In order to find the answer for our first question of if it is possible to obtain all-optical switching based on Kerr nonlinearity in silicon micro-resonators with any specific structure design, we discussed material and structural criteria for ultra-fast Kerr nonlinear switching in resonant cavities in light of the free carrier nonlinearity. A new nonlinear FOM was introduced to define the material criterion, suggesting that Si, GaAs and even AlGaAs cannot be considered as the materials for resonator-enhanced Kerr nonlinear switch at 1.55μm (0.8eV) of wavelength, due to the large free carrier refraction excited by two-photon or three-photon process. We also discussed the validity of our criteria and nonlinear FOM using data from a demonstrated device in the literature. We thus found it is impossible to obtain all-optical switching based on Kerr nonlinearity in silicon micro-resonators and insulators with wider band-gaps such as SiO_2 and SiN will be interesting materials to investigate for this purpose.

Chapter 3, in part, is a reprint of the material as it appears in:

- K. Ikeda and Y. Fainman, "Nonlinear Fabry-Perot resonator with a silicon photonic crystal waveguide," Opt. Lett. 31, 3486-3488 (2006).
- K. Ikeda and Y. Fainman, "Material and structural criteria for ultra-fast Kerr

nonlinear switching in optical resonant cavities," Solid-State Electron. 51, 1376-1380 (2007).

The dissertation author was the primary investigator and author of these papers. The co-authors listed in these publications directed and supervised the research which forms the basis for this chapter.

Chapter 4

Amorphous Silicon for Faster Free-carrier Recombination

4.1 Introduction

In the previous chapter, it has been demonstrated quantitatively that it is impossible to obtain all-optical switching based on Kerr nonlinearity in silicon micro-resonators due to the dominant free carrier nonlinearity excited via TPA. Therefore, the demonstrated devices have the response time limited by the free carrier lifetime of hundreds of picoseconds depending on the device geometry. In order to achieve faster operation in such resonator-enhanced nonlinear devices, we need to identify a new waveguide material with a shorter carrier lifetime or with a smaller TPA coefficient (i.e., wide energy bandgap), and also compatible with the standard CMOS fabrication process. In this chapter, we investigate amorphous silicon as a candidate material to decrease carrier lifetime, utilizing its relatively large density of defects (localized states) as recombination centers leading to a shorter carrier lifetime (~10ps) [49]. Although pure amorphous silicon (a-Si) has a very high defect density preventing it from being useful electronic material, hydrogenated amorphous silicon

(a-Si:H) has long been investigated for solar cells because the film is inexpensively deposited over a very large area and the hydrogen introduced into amorphous silicon terminates the defects [50]. The a-Si:H film can be deposited usually by plasma-enhanced chemical vapor deposition (PECVD) at low temperature (~400°C) on any substrate and therefore is compatible with the CMOS fabrication process. Several works on its application to optical devices have been reported, including a single-mode waveguide with 2.0dB/cm loss [51] and a thermo-optical switch with 10μs response time [52, 53]. However, to the best of our knowledge, no information on nonlinear optical property of amorphous silicon is available in the literature. Here, we present the first measurements of nonlinear optical effects dominated by the free carrier nonlinearity in amorphous silicon films using the z-scan technique and find the enhanced nonlinearity mainly due to the presence of midgap localized states. We also propose a new composite waveguide structure, fabricate such composite waveguides and validate experimentally the results on the enhanced nonlinearity and the shorter free-carrier lifetime.

4.2 Measurement of Nonlinear Optical Property of Amorphous Silicon

We use the z-scan technique (see Fig. 4.1) [54] to investigate the nonlinear optical properties of amorphous silicon films. We use a mode-locked Ti: Sapphire oscillator combined with a regenerative optical amplifier, producing laser pulses with time duration of 100fs, beam diameter of 6mm at a wavelength of 1.55μm and 1kHz repetition rate. A beam splitter is used to reflect a small fraction of the laser beam to a

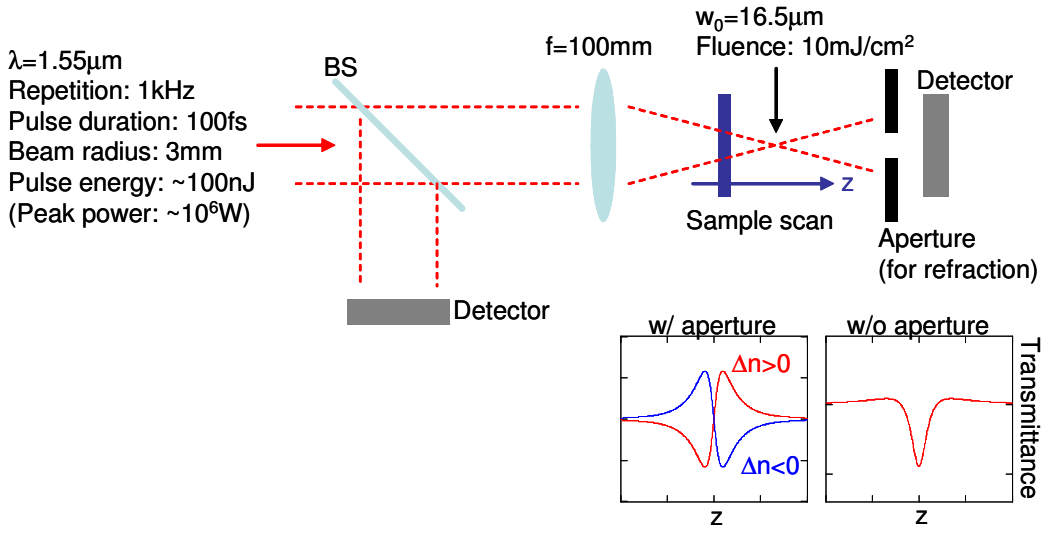

Fig. 4.1 Schematic diagram of the z-scan measurement setup and z-scan traces with and without the aperture.

photodetector to monitor the laser power. The transmitted beam is focused on the sample using a lens with focal length f = 100mm producing 16.5μm beam waist and ~10mJ/cm^2 energy fluence. The incident optical field causes a nonlinear refraction and absorption in the sample as it is being scanned along the optical axis of the lens. The light transmitted through the sample is detected by a detector with or without a small aperture in front of it. When the detection is performed with the aperture, the detected signal has a peak-valley or valley-peak trace, depending on the sign of the nonlinear refraction, because the original Gaussian mode distribution is distorted by the intensity-dependent nonlinear refraction at the focal point. When the detection is performed without the aperture, the detected signal carries only the nonlinear absorption dip information when the sample is at z = 0. The intensity I of the field propagating within the sample satisfies the differential equation,

$$\frac{dI}{dz'} = -(\alpha + \beta I)I \,, \tag{4.1}$$

where α is the absorption coefficient, β is the TPA coefficient, z' is the coordinate within the sample. The solution of Eq. (4.1) at the output surface of the sample ($z' = L$, where L is the thickness of the sample) can be written as,

$$I(L, r, t, z) = \frac{I(0, r, t, z)\exp(-\alpha L)}{1 + q(r, t, z)}, \tag{4.2}$$

where $I(0, r, t, z)$ is the Gaussian mode behind the lens, $q(r, t, z) = \beta I(0, r, t, z)L_{eff}$, with $L_{eff} = (1 - \exp(-\alpha L))/\alpha$. When the aperture is present, we calculate the field integral over the aperture area using the Gaussian decomposition method or the Fresnel integral. When the aperture is absent, we simply integrate Eq. (4.2) spatially and temporally, yielding the normalized transmittance at $z = 0$,

$$T(z = 0) = \frac{1}{\sqrt{\pi} q_0} \int_{-\infty}^{\infty} \ln\left[1 + q_0 \exp(-\tau^2)\right] d\tau \,, \tag{4.3}$$

$$q_0 = \beta I_0 L_{eff} \,, \tag{4.4}$$

where I_0 is the center peak intensity of the original Gaussian pulse. Fig. 4.2 shows the plot of $T(z = 0)$ in Eq. (4.3) with relation to the parameter q_0 in Eq. (4.4). Note that q_0 is obtained from the measured normalized transmission dip corresponding to the value of $T(z = 0)$ using Fig. 4.2. Once q_0 is found, we can then calculate β using Eq. (4.4) with the known I_0 and L_{eff}. We use this q_0 for the data analysis later.

We fabricated and prepared four samples for the z-scan measurement as summarized in Table 4.1. One of the samples was a-Si prepared using RF sputtering and two other samples were a-Si:H prepared by different PECVD processes with

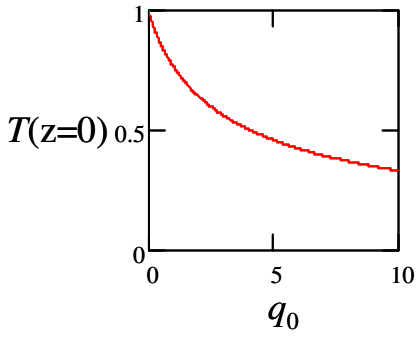

Fig. 4.2 Plot of normalized transmittance at $z = 0$ vs. parameter q_0 from Eq. (4.3) for z-scan measurement without aperture.

Table 4.1 Samples for the z-scan measurement.

Material	a-Si □	a-Si:H(1) ○	a-Si:H(2) △	c-Si ×
Refractive index n_0	3.7	3.4	3.4	3.48
Thickness L	4.85μm	2.94μm	3.14μm	220μm
Absorption α at 1.55μm	0.7dB/μm	0.037dB/μm	small	small
Substrate	1mm SiO_2	150μm SiO_2	0.5mm SiO_2	-
Process	RF sputtering	PECVD	PECVD (high quality)	-

saline and helium mixture (See Appendices A.1 for the detail process). The fourth sample was crystalline silicon (c-Si). The amorphous samples with thicknesses of several microns are deposited on silicon dioxide substrates, much thinner than the thickness of the crystalline sample. We measured the transmission spectra of the samples using a normally incident beam from a 120nm-broadband source centered at a wavelength of 1.56μm. We estimate the film thicknesses L from the observed Fabry-Perot resonance oscillations, assuming the refractive index n_0 of 3.7 [55] for a-Si and 3.4 [52] for a-Si:H. The obtained thickness for a-Si was close to the expected value estimated from the deposition rate and the total deposition time. We also

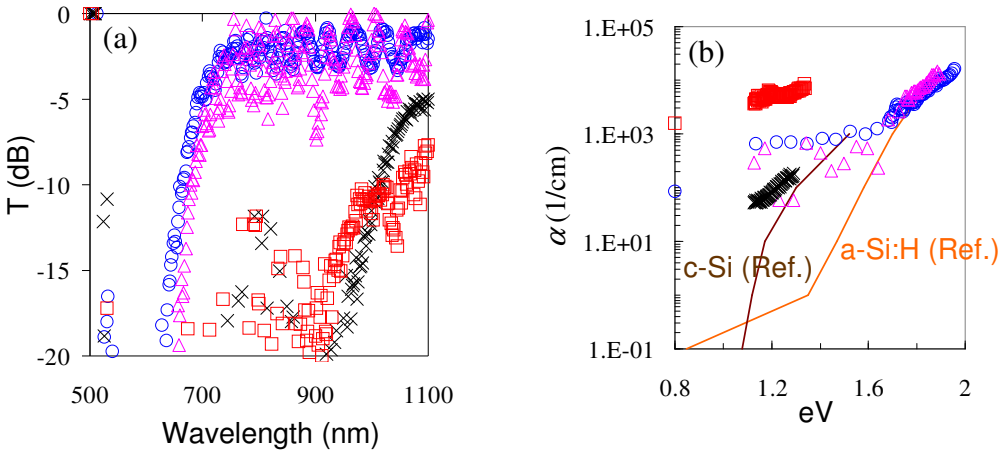

Fig. 4.3 (a) Transmission spectra of the samples using a super-continuum light source with the wavelength ranging from 500nm (2.48eV) to 1100nm (1.13eV); (b) Plot of absorption coefficient vs. photon energy as extracted from (a). The values in Ref. [52] for a-Si:H and c-Si are also plotted. (Red square: a-Si, blue circle: a-Si:H(1), pink triangle: a-Si:H(2), black cross: c-Si)

determined the material absorption α around 1.55μm of the films from the peaks of the Fabry-Perot oscillations. Next, we measured the transmission spectra of these samples using a super-continuum light source with the wavelength ranging from 500nm (2.48eV) to 1100nm (1.13eV), as shown in Fig. 4.3(a). Fig. 4.3(b) shows the plot of absorption coefficient vs. photon energy which was extracted from the transmission spectra in Fig. 4.3(a). Note that the noisy data points with the transmission below −20dB were removed for the clarity of the graph. For reference, we also include plots of the values from Ref. [52] for a-Si:H and c-Si. We conclude that the measured α for c-Si is consistent with those in Ref. [52]. The measured α for a-Si is very large, which means that the density of defect states in a-Si is very large. The measured α for a-Si:H ranges between the values measured for c-Si and a-Si, indicating that a-Si:H has a moderate defect density. We also observe that the

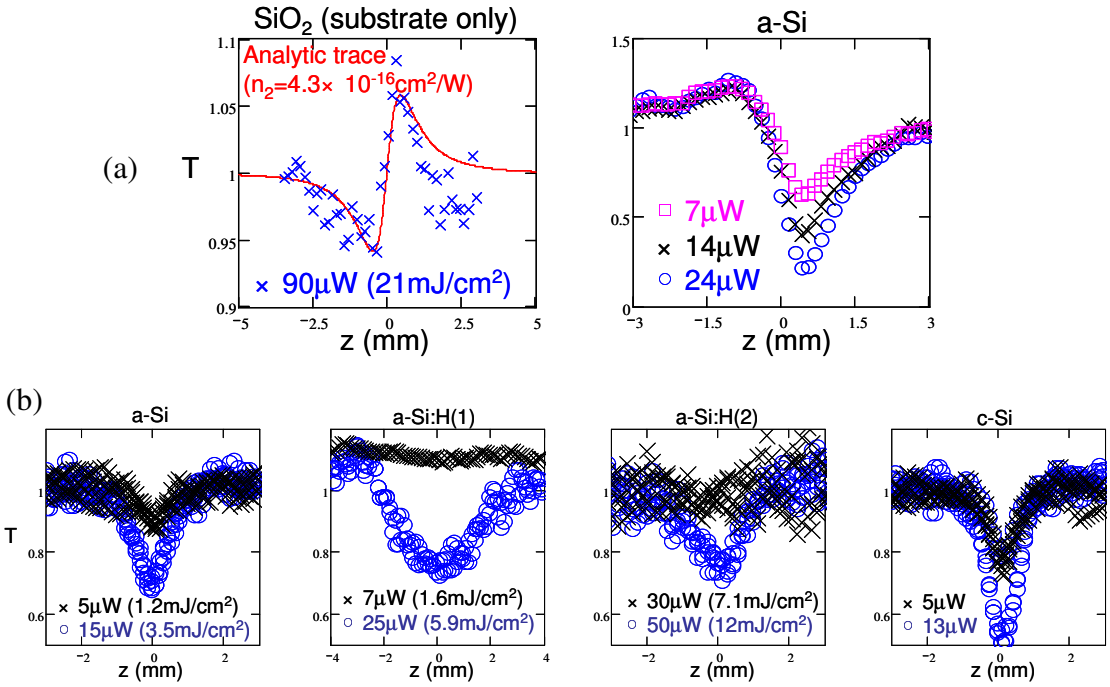

Fig. 4.4 (a) z-scan traces when the aperture is present, for a 1mm-thick SiO_2 substrate and for the a-Si sample on the SiO_2 substrate; (b) z-scan traces without aperture for all the samples measured at different average powers.

a-Si:H(2) sample has a higher quality (i.e. lower density of defects) than the a-Si:H(1) sample. It should be noted that the film quality of our samples decreases in the following order: c-Si > a-Si:H(2) > a-Si:H(1) > a-Si.

Fig. 4.4 summarizes the z-scan measurement results: Fig. 4.4(a) shows the normalized transmittance vs. z-coordinate when we use an aperture for a 1mm-thick SiO_2 substrate and the a-Si sample. Fig. 4.4(b) shows the normalized transmittance traces vs. z-coordinate for our 4 samples described in Table 4.1 with different average powers, when we did not use the aperture. It is evident that we can neglect the effect of the SiO_2 substrate on our characterization of silicon films, since the laser beam at very high power of 90μW generated only a small signal for the thick SiO_2 substrate

(see Fig. 4.4(a)) in contrast to those for the silicon samples with smaller powers. For the analytic fit (the solid curve in Fig. 4.4(a)), we used a value $n_2 = 4.3 \times 10^{-16}\text{cm}^2/\text{W}$, which is only two times larger than the values of n_2 for SiO_2 found in the literature [42], indicating a good accuracy of our measurements. The discrepancy might be due to an error in the confocal parameters we used since the beam from the femto-second light source was not a very clean Gaussian. The trace for a-Si in Fig. 4.4(a) is inverted in z direction, in comparison to that for SiO_2 substrate, indicating that the dominant nonlinear effect in a-Si corresponds to the negative nonlinear refraction due to free carrier nonlinearity. From the results in Fig. 4.4(b), we note that the signals for a-Si and c-Si are very close, although the thickness of a-Si is much less than that of c-Si. Therefore, we expect that the nonlinear effect in a-Si will be much larger than that in c-Si. In contrast, for a-Si:H samples, since higher input powers are required to obtain the similar level of signals to these observed in a-Si, we anticipate that the nonlinear effect in a-Si:H should be smaller than that in a-Si. To quantify these observations, we plot the parameter q_0 vs. average power in Fig. 4.5 which are found from the measured z-scan dips $T(z = 0)$ using the relation of Eq. (4.3) plotted in Fig. 4.2, together with the linear fits (dotted lines) from the analytic formula given by Eq. (4.4). The values of β are estimated from the dotted lines providing the values of 4.4cm/GW, 12cm/GW, 40cm/GW and 120cm/GW for our four samples c-Si, a-Si:H(2), a-Si:H(1) and a-Si respectively, which corresponds to the order of the film quality. The estimated value of 4.4cm/GW for c-Si is only several times larger than that found in the literature [29]. Again, this discrepancy might be due to an error in the confocal parameters we used or

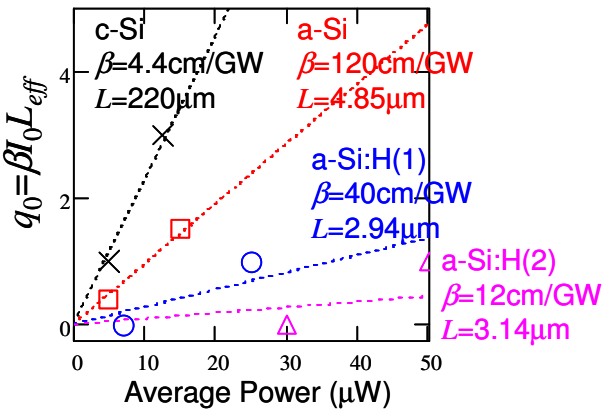

Fig. 4.5 Parameter q_0 found from the z-scan dips using the relation of Fig. 4.2, with relation to the average power, together with the linear fits (dotted lines) from the analytic formula of Eq. (4.4).

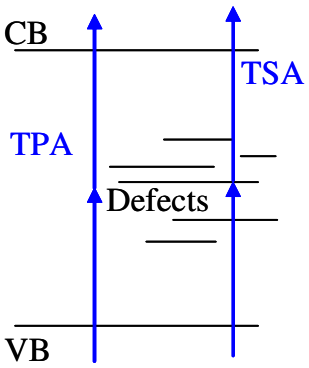

Fig. 4.6 Schematic diagram describing two-step absorption (TSA) through midgap localized states.

due to the material itself. The values for a-Si and a-Si:H are extremely large as we have expected. We attribute such a large nonlinear absorption to the "two-step" absorption (TSA) process through the midgap localized states (See Fig. 4.6). n_2 could be directly measured at much lower fluence levels but the n_2 signal in our setup was unfortunately not able to be distinguished from the noise. It should be noted that accurate measurements of n_2 can be achieved using waveguide structures with a longer

interaction length [56], however these measurements are not in the scope of our current study.

For more accurate analysis of the nonlinear interactions, we modify Eq. (4.1) by including the free-carrier absorption term yielding,

$$\frac{dI}{dz'} = -(\alpha + \beta I + \sigma N) I \,, \tag{4.5}$$

where σ is the change in the attenuation per unit photo-excited free carrier density and N is the carrier density. When we assume that the free carriers in the a-Si and a-Si:H samples are mainly generated via TSA, the σ and N are described by,

$$\sigma = \frac{e_0^3 \lambda^2}{4\pi^2 c^3 \varepsilon_0 n_0} \left(\frac{1}{m_e^2 \mu_e} + \frac{1}{m_h^2 \mu_h} \right), \tag{4.6}$$

$$N = \frac{\alpha}{2\hbar\omega} \frac{\sqrt{\pi}\tau_p}{2\sqrt{\ln 2}} I \,, \tag{4.7}$$

where we reproduced σ from Ref. [37] and N is found from integrating Gaussian temporal variation of I, e_0 is the electron charge, ε_0 is the vacuum permittivity, m_e and m_h are the effective masses of electrons and holes, μ_e and μ_h are the mobilities of electrons and holes, n_0 is the refractive index of the material and τ_p is the time duration of the laser pulses. Therefore, we can combine the second and the third terms on the right-hand side of Eq. (4.5) and define an enhanced nonlinear absorption coefficient β' as,

$$\beta' = \beta + \sigma \frac{\alpha}{2\hbar\omega} \frac{\sqrt{\pi}\tau_p}{2\sqrt{\ln 2}} \,. \tag{4.8}$$

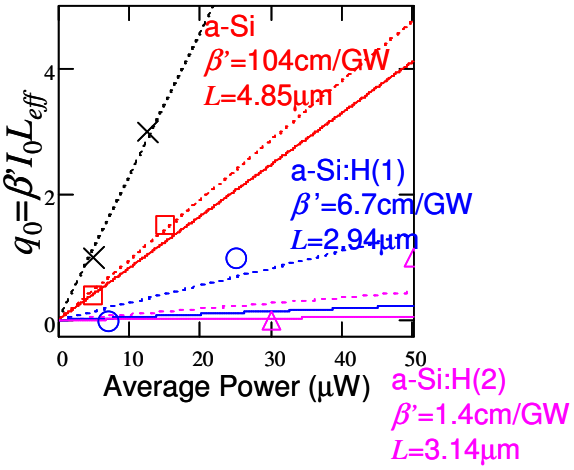

Fig. 4.7 Data from Fig. 4.5 together with the relation $q_0 = \beta' I_0 L_{eff}$ plotted for a-Si and a-Si:H as solid lines.

The last equation indicates that the free carrier absorption excited by TSA is of the same order as TPA, whereas the free carrier absorption due to TPA is of the higher order. Thus, Eq. (4.5) can be solved in the same way as Eq. (4.1) but by replacing β with β', yielding the relation $q_0 = \beta' I_0 L_{eff}$ instead of Eq. (4.4) plotted for a-Si and a-Si:H as solid lines in Fig. 4.7. We used the following parameters; β = 0.8cm/GW (from c-Si [29]), $m_e = 0.5m_0$, $m_h = 1.0m_0$, μ_e = 2.0cm^2/Vs and μ_h = 0.4cm^2/Vs [49]. The calculated β' are 104cm/GW for a-Si, 6.7cm/GW for a-Si:H(1) and 1.4cm/GW for a-Si:H(2), where we used one order magnitude smaller α for a-Si:H(2) than that for a-Si:H(1) as roughly estimated from the data. We observe that the q_0 vs. P plots with the β' in Fig. 4.7 are fairly close to the measured z-scan data especially at lower powers. The discrepancy at higher power will be from an additional free carrier absorption excited via TPA. Fig. 4.8 shows the plot of β' with relation to α from Eq. (4.8) with example waveguide losses of 1dB/cm for a channel waveguide and 1dB/mm

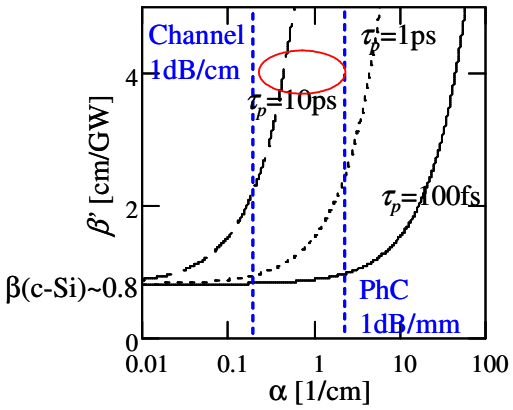

Fig. 4.8 Plot of β' vs. α from Eq. (4.8) with example waveguide losses of 1dB/cm for channel waveguides and 1dB/mm for slab PhC waveguides.

for a slab PhC waveguide. Since we are using laser pulses of 100fs, a higher α (> 10dB/mm) than that of PhC waveguides or channel waveguides is required to have an enhanced nonlinearity and this will lead to device degradation. However, if we are to use picosecond pulses, the enhancement occurs even at a lower value of α (< 1dB/mm), comparable to these waveguide losses. Therefore, amorphous silicon with small α can be useful to enhance the nonlinear effects in waveguide devices without device degradation. Note that the enhancement of free carrier refraction Δn via TSA can be calculated in the similar way [37] with $\Delta n = -(e^2\lambda^2/8\pi^2c^2\varepsilon_0 n_0)[1/m_e+1/m_h]N$.

4.3 Composite Waveguides Made of Amorphous and Crystalline Silicon

We exploit the results discussed in the previous section by constructing a novel composite waveguide consisting of a-Si and c-Si (ac-Si) for use in silicon photonics applications. The advantage of our structure is that the effect from midgap states can

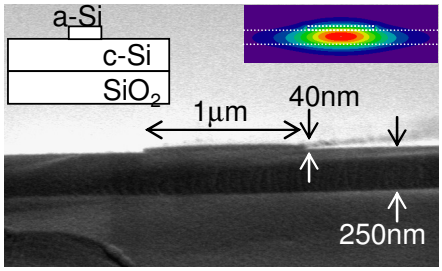

Fig. 4.9 SEM micrograph of a fabricated composite rib waveguide with a loss of about 3dB/mm

be tailored by controlling the fraction of a-Si in the ac-Si composite, instead of depositing different films with different recipes. Additionally, the c-Si layer can act as a heat sink for a-Si since thermal conductivity of c-Si is much higher than that of a-Si [53]. Fig. 4.9 shows the SEM micrograph of a fabricated composite rib waveguide with about 3dB/mm loss. This waveguide was fabricated by (i) e-beam lithography with polymethyl-methacrylate (PMMA) resist spin-coated on a SOI chip, (ii) RF sputtering of a-Si and (iii) lift-off the a-Si film (See Appendices A.1 for details). We measure β' of this waveguide using picosecond laser pulses with repetition rate of 76MHz, and the solution of Eq. (4.1) with replacing β by β', yields

$$T^{-1} = T_0^{-1} + \frac{C \cdot \beta' \cdot L_{eff}}{T_0 \cdot A_{eff}} P, \tag{4.9}$$

where T_0 is the transmission at low power (linear regime), C is the coupling loss to the waveguide, P is the input peak power, A_{eff} is the effective core area of the waveguide. If we measure and plot the inverse transmittance T^{-1} of this waveguide with regard to the input peak power P, we can extract β' from the tilt of the plot since we know the other parameters in the second term of the right-hand side of Eq. (4.9) [56]. Fig.

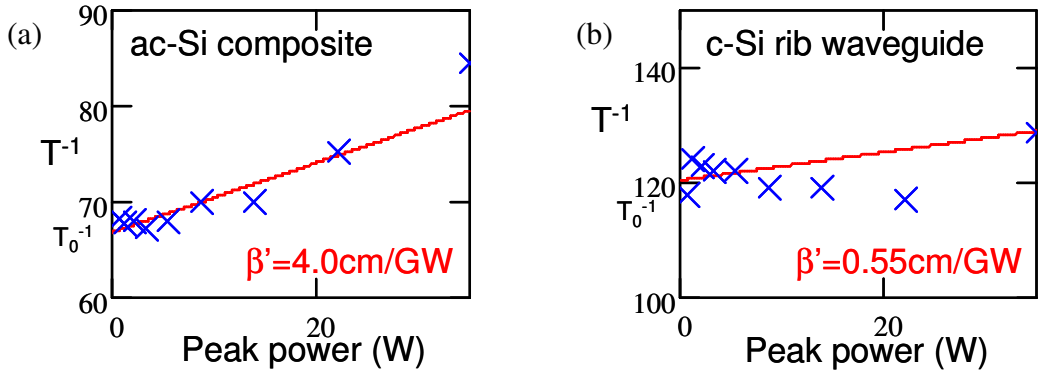

Fig. 4.10 Plot of inverse transmittance vs. the input peak power (a) for the ac-Si composite rib waveguide; (b) for a pure c-Si rib waveguide with similar dimensions.

4.10(a) is the result for the ac-Si composite rib waveguide and Fig. 4.10(b) is the result for pure c-Si rib waveguide with similar dimensions. The measured β' are 0.55cm/GW and 4cm/GW for c-Si and ac-Si, respectively. Since the data points in Fig. 4.10 do not appear exactly linear, it might include a higher order nonlinear absorption probably from the free carrier absorption via TPA. Therefore, the estimated values might not be very accurate. Even so, we can clearly see from the data that the nonlinear absorption in the ac-Si waveguide is much larger than that in the c-Si waveguide. Since some part of waveguide loss should come from scattering, the loss due to midgap states α will be a little smaller than 3dB/mm. Also, we used pulses with about 10ps time duration. Therefore, this measurement approximately corresponds to the area indicated by the red circle in Fig. 4.8.

4.4 Free-carrier Lifetime Measurements

We measure the free-carrier lifetime of the composite rib waveguide in Fig. 4.9, by introducing the same picosecond pulses at 1.54μm as a pump and a CW source at

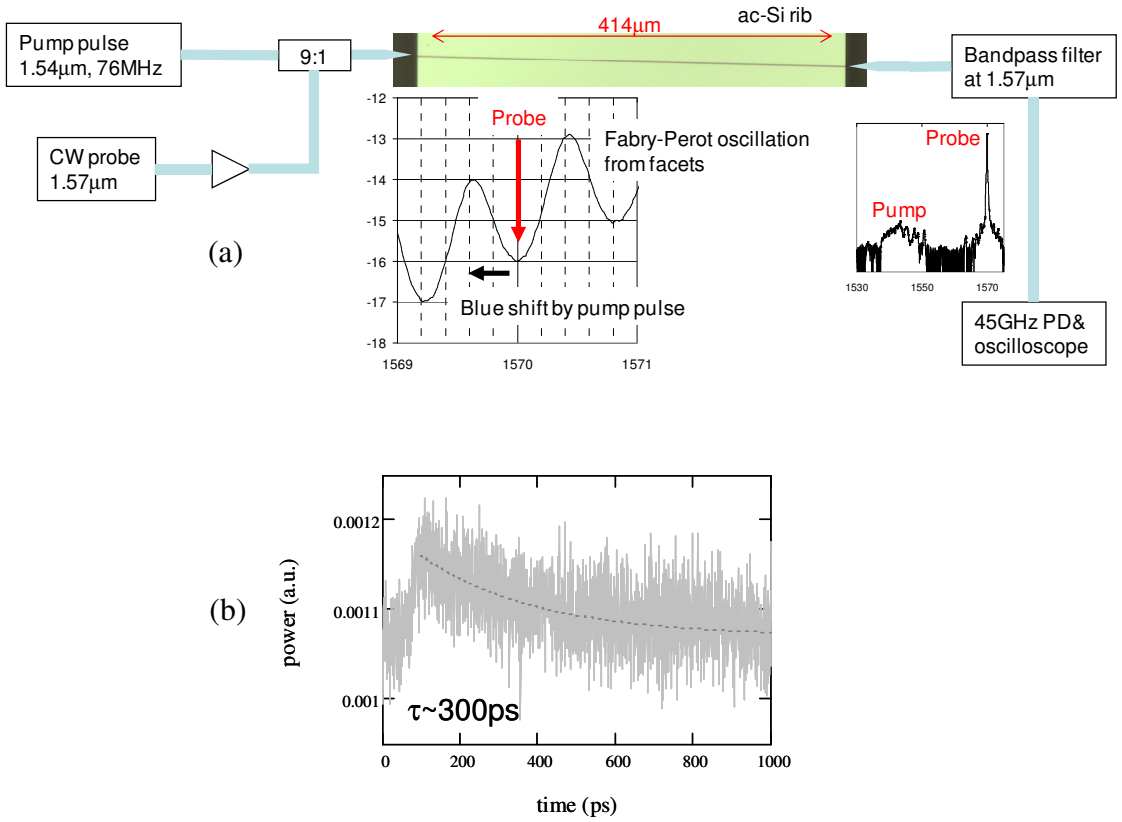

Fig. 4.11 (a) Measurement setup for the carrier lifetime measurement of the composite waveguide in Fig. 4.9; (b) Probe signal modulated by the free-carrier nonlinear refraction excited by pump laser pulses.

1.57μm as a probe signal. This composite waveguide has oscillations in the transmission spectrum that is described by Fabry-Perot effect due to the impedance mismatch on the input-output facets. Since the picosecond pump pulses excite the free carriers by TSA or TPA, the refractive index is modulated by the free carriers, causing the transmitted Fabry-Perot spectrum to shift to shorter wavelengths. Therefore, we can detect the modulated probe signal using a 45GHz photo-detector and oscilloscope. Fig. 4.11(a) and (b) show the measurement setup and the detected probe signal, respectively. The detected signal has 300ps decay time, which is shorter than the

reported values in the literature for pure c-Si waveguides (for example, 1ns [57] or 450ps [58]).

We next fabricated a ring resonator (see Fig. 4.12(a)) with an ac-Si composite channel waveguide with the cross section and the mode profile (for quasi-TE mode) shown in Fig. 4.12(b). The same pure a-Si film without hydrogen of about 20nm thickness was deposited on a SOI chip, followed by e-beam lithography with PMMA, nickel lift-off, and RIE etching processes (see Appendices A.1 for the details). The measured spectrum for quasi-transverse magnetic (TM) mode is shown in Fig. 4.12(c) and the quality factor was measured to be 2200 at 1550nm. We demonstrate switching operation using 430nm femtosecond pump pulses illuminating the ring resonator from the top through a microscope objective lens, and 1550nm (on the resonance) CW probe signal coupled into/out the input/output waveguides through tapered fibers. We achieved 30% modulation of the probe signal using 17pJ/pulse energy as shown in Fig. 4.13(a). Notice that the carrier lifetime was around 30ps, which is much shorter than the reported value in similar experiment [58]. Even in an ion-implanted PhC resonator, the lifetime was reported to be around 70ps [57]. We also measured the carrier lifetime in a pure c-Si ring resonator (see Fig. 4.13(b)) fabricated by the same process, and found that the observed carrier lifetime of ~40ps was similar to that in the ac-Si ring resonator. Since we measured a very large waveguide loss of about 20dB/mm for both the waveguides in quasi-TE polarization (we can observe the roughness in Fig. 4.12(a)), we hypothesize that the main recombination centers for the generated free carriers in these waveguides were the surface states due to the rough sidewalls

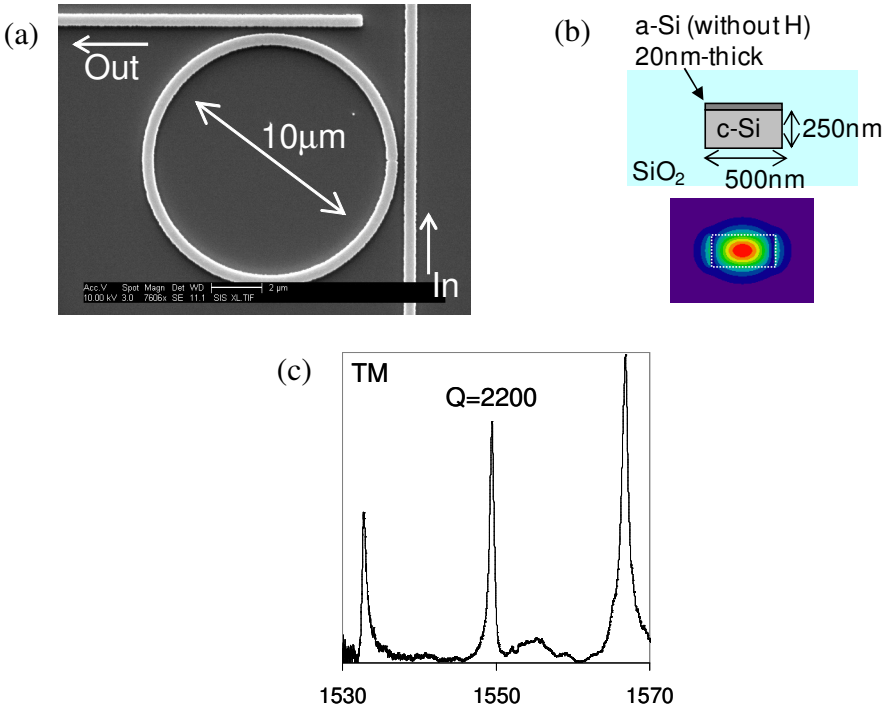

Fig. 4.12 (a) SEM micrograph of the fabricated ring resonator with the ac-Si composite channel waveguide; (b) Cross section and mode profile (quasi-TE mode) of the ac-Si composite channel waveguide; (c) Measured spectrum for quasi-TM mode of the ring resonator.

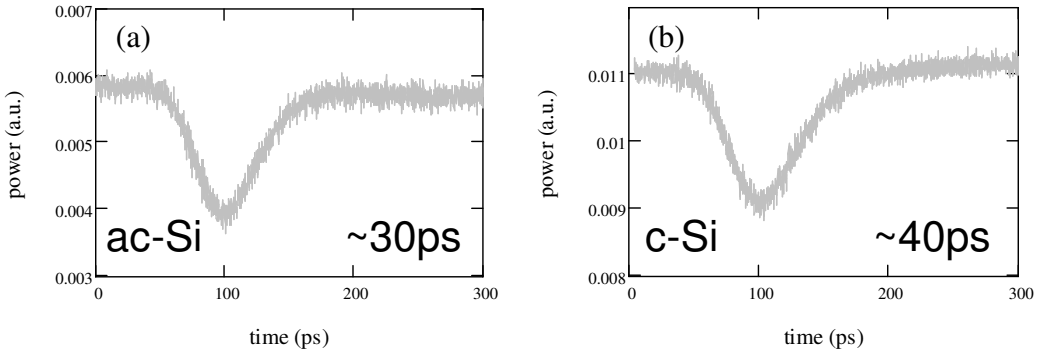

Fig. 4.13 Switching operation of the ring resonators using 430nm femtosecond pump pulses incident from the top and 1550nm probe at the resonant wavelength, with (a) ac-Si composite channel waveguide; (b) pure c-Si channel waveguide.

originating from our lithography and RIE processes. Also, there is a report [59] that some silicide can be formed on waveguide sidewalls during a RIE process if nickel

mask is used, and it induces a very high waveguide loss. This might be another possible reason for this very short carrier lifetime. The results from these resonators unfortunately do not demonstrate the advantage of the faster recombination originating from a-Si due to the roughness of the structure. They however demonstrated that we can make a resonant device using the ac-Si waveguide structure.

In order to distinguish the effect of the defect states in a-Si from that of the roughness, we removed the sidewall roughness (20dB/mm → 0.7dB/mm) by changing the fabrication recipe for silicon etching, from the nickel mask process with Trion etcher to the hydrogen silsesquioxane (HSQ) [60] mask process with Oxford etcher (see Appendices A.1 for details). We fabricated three waveguides using this process, i.e. pure c-Si channel waveguide (~ 500nm × 250nm), ac-Si channel waveguide in the same cross section as in Fig. 4.12(b) but with a-Si:H(2) in Table 4.1, ac-Si channel waveguide in the same cross section as in Fig. 4.12(b). The first waveguide and the third waveguide had the waveguide losses of about 0.5dB/mm and about 4dB/mm for quasi-TM polarization, which represent the density of defect states in the waveguides. The second waveguide should have the waveguide loss between these values because the a-Si:H(2) has lower density of defect states. We measured the carrier lifetime of these waveguides in the same setup used in Fig. 4.13. In this measurement, we did not make ring resonators but used the Fabry-Perot oscillation from the input and output facets of the waveguides in order to have the modulated probe signal and illuminated a part of the waveguides with the focused 430nm pump pulses from the top. Also we coupled the probe with quasi-TM polarization since the mode size of quasi-TM mode

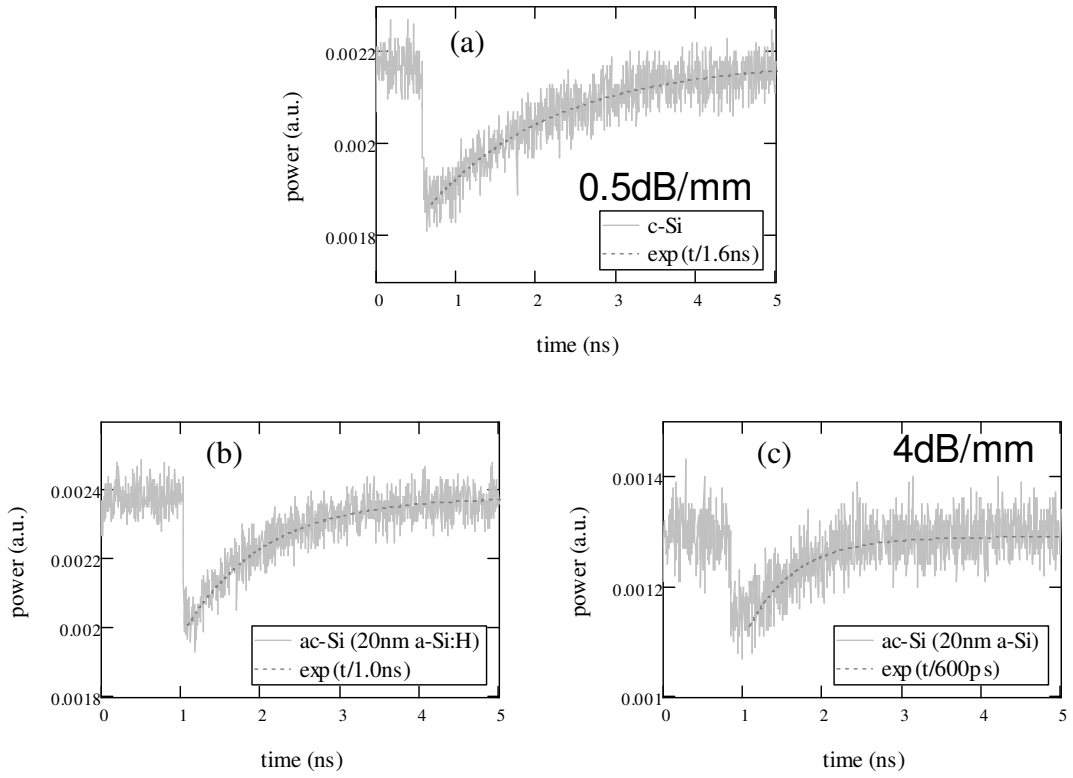

Fig. 4.14 (a), (b) and (c) Detected probe signals for the pure c-Si channel waveguide, the ac-Si channel waveguide with a-Si:H(2) and the ac-Si channel waveguide with a-Si, respectively, all fabricated with the HSQ process.

is larger and the coupling loss from the tapered fiber tips to the waveguides is smaller. Fig. 4.14(a), (b) and (c) show the detected probe signals for the pure c-Si waveguide, the ac-Si waveguide with a-Si:H(2) and the ac-Si waveguide with a-Si, respectively. We observe in Fig. 4.14 that the measured carrier lifetime decreases as the defect density becomes higher (1.6ns → 1.0ns → 600ps). Therefore, we conclude that the defect states in the composite waveguides indeed act as the recombination centers for the photo-excited free carriers and shorten the carrier lifetime. However, the carrier lifetime of 600ps is not very short although the lifetime in a-Si should be much shorter [49]. We could anticipate that the free carriers excited within the c-Si region move into

the a-Si region much slower than the decay time within the a-Si region but faster or similar to the decay time within the c-Si region. We estimated the decay time τ_m from the c-Si region to the a-Si and a-Si:H(2) regions as 0.96ns and 2.7ns respectively using the relation,

$$\frac{1}{\tau_{eff}} = \frac{1}{\tau_{c-Si}} + \frac{1}{\tau_m}, \tag{4.10}$$

where $\tau_{c\text{-}Si}$ is the decay time within the c-Si region (i.e. 1.6ns) and τ_{eff} is the measured effective decay time (i.e. 600ps and 1.0ns). In order to see the carrier decay within the a-Si region, we changed the probe wavelength to the peak or dip of the Fabry-Perot oscillation, where the free carrier refraction excited by the 430nm pump pulses does not modulate the probe signal. In this case, we detect only the free carrier absorption within the amorphous region since the free carrier absorption in amorphous silicon is much larger than in c-Si due to the very low carrier mobility (see Eq. (4.6)). Fig. 4.15 shows the detected probe signal for the ac-Si channel waveguide with a-Si:H(2). We observe the very fast recombination with the lifetime of about 25ps. We did not detect any probe signal for the ac-Si channel waveguide with a-Si probably because the decay time in a-Si with the higher defect density was too short to detect using our 45GHz photodetector. Therefore, as we anticipated, although the free carriers excited within the a-Si region of the composite waveguides recombine very quickly, the free carriers excited within the c-Si region move into the a-Si region much slower than the decay time within the a-Si region. The behavior of the free carriers at the boundaries could be affected by a surface treatment before the a-Si deposition and thermal

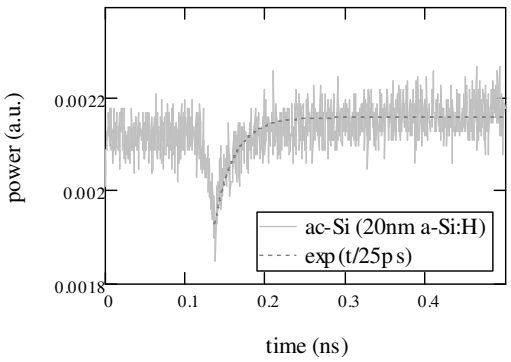

Fig. 4.15 Detected probe signal for the ac-Si channel waveguide with a-Si:H(2) at the probe wavelength on the peak or dip of the Fabry-Perot oscillation.

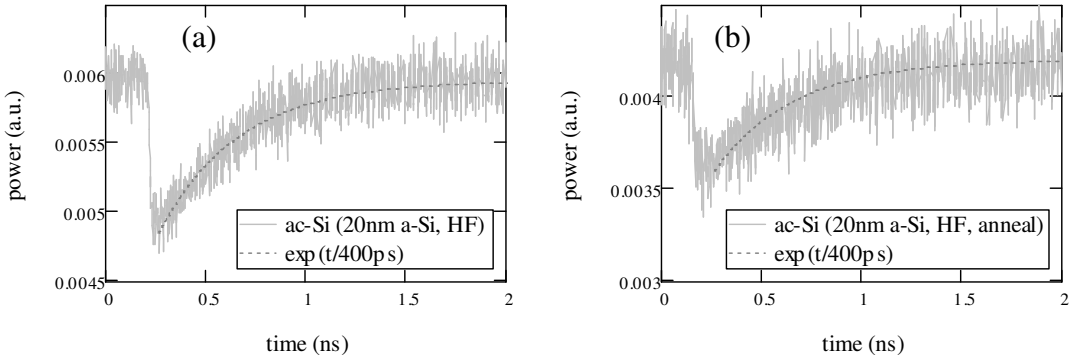

Fig. 4.16 Detected probe signals for the ac-Si channel waveguides with a-Si with the treatments of (a) RCA and HF dip before the a-Si deposition, (b) annealing at 600˚C for 3 hours after (a).

treatment after the deposition [61, 62]. For the ac-Si waveguides used so far, any treatment had not been done before the a-Si depositions. We performed the RCA clean and hydrofluoric acid (HF) dip right before the a-Si deposition (Fig. 4.16(a)) and the additional annealing at 600˚C for 3 hours after the a-Si deposition (Fig. 4.16(b)) when fabricating new ac-Si channel waveguides with a-Si. We observe from Fig. 4.16(a) that the measured carrier lifetime (τ_{eff} = 400ps) and the corresponding decay time from the c-Si to a-Si regions (τ_m = 530ps with Eq. (4.10)) are shorter than those (τ_{eff} = 600ps

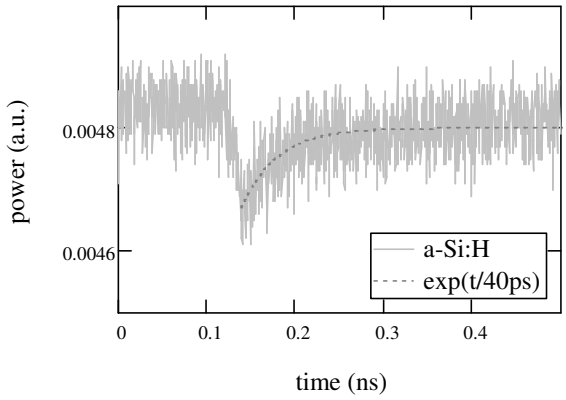

Fig. 4.17 Detected probe signal for the channel waveguide with only a-Si:H(2).

and τ_m = 960ps) in Fig. 4.14(c), however the additional annealing did not change the carrier lifetime. Further investigation on the carrier dynamics at the boundary between the c-Si and a-Si regions will be necessary to further shorten the carrier lifetime in the composite waveguide structure. One possibility is to increase the area of the boundary, for example, to use polysilicon in which crystalline grains are surrounded by disordered amorphous network. In fact, a shorter carrier lifetime (~130ps) in polysilicon waveguides has been recently reported [63]. Another simple direction is to use waveguides made of only amorphous silicon with relatively low absorption. We succeeded to fabricate waveguides using only the a-Si:H(2) and the HSQ process with the dimensions of about 500nm × 250nm and the propagation losses of 5dB/mm for TE and 4dB/mm for TM mode. Fig. 4.17 shows the detected probe signal for this waveguide in the same measurement. We can see a very short decay time of about 40ps close to the result in Fig. 4.15. However, in this waveguide, we observed only the free carrier absorption since it is more significant than the free carrier refraction due to its lower mobility. Therefore, if we use this waveguide for the resonator-enhanced

switching devices, the operation principle will be quite different from what we assumed for the free carrier refraction.

4.5 Summary

We measured enhanced nonlinearities in amorphous silicon using the z-scan technique. The free-carrier nonlinearity due to TSA through midgap states explained this effect. We introduced, fabricated and characterized composite ac-Si waveguides made of a-Si and c-Si. The fabricated composite rib waveguide is confirmed to have the enhanced free-carrier nonlinearity at the estimated value of 4cm/GW, seven times larger than that of a pure c-Si waveguide. We measured the free-carrier lifetime in the composite rib waveguide (~300ps), which was shorter than the reported values in the literature for similar geometries of c-Si. We also fabricated a ring resonator using the composite waveguide approach and demonstrated the modulation function using femto-second pump pulses. The resonator had a very short carrier lifetime of ~30ps, which was attributed to the high density of surface states or the silicide contamination both due to the dry etching process. The composite waveguides with reduced sidewall roughness proved that the defect states in the a-Si region facilitate the recombination of photo-excited free carriers. Although the free carriers excited within the amorphous region of the composite waveguides recombine very quickly (< 25ps), the free carriers excited within the crystalline region move into the amorphous region much slower (530ps) than the decay time within the amorphous region. The processes of RCA clean and HF dip right before the a-Si deposition shortened the carrier decay time from the amorphous to the crystalline regions. However, further investigation on the carrier

dynamics at the boundary between the c-Si and a-Si regions will be necessary to further shorten the carrier lifetime in the composite waveguide structure. The waveguide with only hydrogenated amorphous silicon had a very short lifetime (<40ps). However, we have to reconsider how to apply this waveguide to the resonator-enhanced all-optical switching since the free carrier absorption is the dominant nonlinear effect in the waveguide.

Chapter 4, in part, is a reprint of the material as it appears in:

- K. Ikeda, Y. Shen and Y. Fainman, "Enhanced optical nonlinearity in amorphous silicon and its application to waveguide devices," Opt. Express 15, 17761-17771 (2007),

and, in part, is currently being prepared for submission for publication of the material. The dissertation author was the primary investigator and author of these papers. The co-authors listed in the publication assisted and supervised the research which forms the basis for this chapter.

Chapter 5

Silicon Nitride for Ultra-fast Kerr Nonlinear Switching

5.1 Introduction

In Chapter 3, it has been demonstrated quantitatively that it is impossible to obtain all-optical switching based on Kerr nonlinearity in silicon micro-resonators due to the dominant free carrier nonlinearity excited via TPA. Therefore, the demonstrated devices have the response time limited by the free carrier lifetime of hundreds of picoseconds depending on the device geometry. In order to achieve faster operation in such resonator-enhanced nonlinear devices, we need to identify a new waveguide material with a shorter carrier lifetime or with a smaller TPA coefficient (i.e. wide energy bandgap), and also compatible with the standard CMOS fabrication process. In Chapter 4, amorphous silicon has been investigated as a candidate for the new material with a shorter carrier lifetime. In this chapter, we investigate silicon nitride (SiN) as a candidate for the new material with a smaller TPA coefficient, because its relatively larger refractive index than silicon dioxide (SiO_2) results in small waveguide dimensions and its large energy bandgap gives a negligible TPA coefficient. This

material will be also useful in pure bound electronic nonlinear processes in a long interaction scheme without resonant structures since in silicon these devices are often limited by the nonlinear loss incurred by the generation of carriers and TPA [64]. Moreover, extensive researches in silicon photonics have been so far focused on using SOI substrates where the buried oxide layer is used as the under cladding and the crystalline silicon layer as the waveguide cores. This assumes that the photonic circuits are integrated in a single layer shared with electronic circuits. However, for more flexible and efficient integration, three dimensional multi-layer structures will be necessary, and SiN is one of the potential candidates because it is prepared by deposition processes. This material can be deposited by either low pressure chemical vapor deposition (LPCVD) at ~800°C, or PECVD at ~400°C. Although these are both accessible equipments in the standard silicon fabrication process, the PECVD will be more attractive for various applications due to the low process temperature. Several works on optical waveguide applications using SiN films prepared by LPCVD [65-68] have been reported. However, to the best of our knowledge, no work with the films by PECVD has been reported due to the basic drawback of large tensile stress resulting in undesirable cracks [65]. Here, we present a SiN/SiO_2 waveguide and resonators using materials prepared by PECVD with dual frequency reactors that can significantly reduce the stress [69], and we also evaluate the nonlinear response of this material.

5.2 Fabrication of Waveguides and Micro-resonators

We begin with depositing a 3μm-thick SiO_2 under-cladding layer on a silicon substrate, followed by deposition of a 500nm-thick SiN core layer, using the Oxford

Plasmalab PECVD system where the stress of the SiN film is controlled by alternating between RF and low frequency plasmas during the deposition. The SiO_2 film is deposited in the same process as used for the upper-cladding layer in the silicon fabrication (See Appendices A.1). The SiN film is deposited with the gas mixture of 5% SiH_4 diluted by N_2 (400sccm), NH_3 (22sccm) and N_2 (600sccm), the process pressure of 650mT, the process temperature of 350°C, and the plasma frequencies alternating between 13.56MHz (20W, 13s) and 100kHz (20W, 7s). The refractive indexes of the fabricated films of SiN and SiO_2 are around 1.99 and 1.46, respectively. We next perform e-beam lithography with 30kV acceleration voltage using PMMA lift-off process to make a nickel hard mask pattern on top of the SiN film. Then, a RIE with the gas mixture of CHF_3 (16sccm) and O_2 (3sccm) [68], the process pressure of 30mT, and the RIE power of 100W is used to define the SiN waveguide with 1μm width. After the nickel mask is removed, a 2μm-thick SiO_2 upper-cladding layer is deposited by the same process. Fig. 5.1(a) and (b) show the scanning electron microscope (SEM) pictures for the etched SiN waveguide before the upper-cladding deposition and the cross section of the waveguide after the deposition, respectively. We made an array of the waveguides with different lengths up to 5mm and measured the transmission loss of 4dB/cm for TE-like modes (see Fig. 5.1(c)), which is found comparable to those measured in waveguides prepared by LPCVD [65-68].

Using the same procedure, we fabricated add-drop type ring resonators with different bending radiuses (r = 10, 15, 20μm) and different gaps between the bus waveguides and the rings (g = 300, 500, 700nm). We measured the transmission

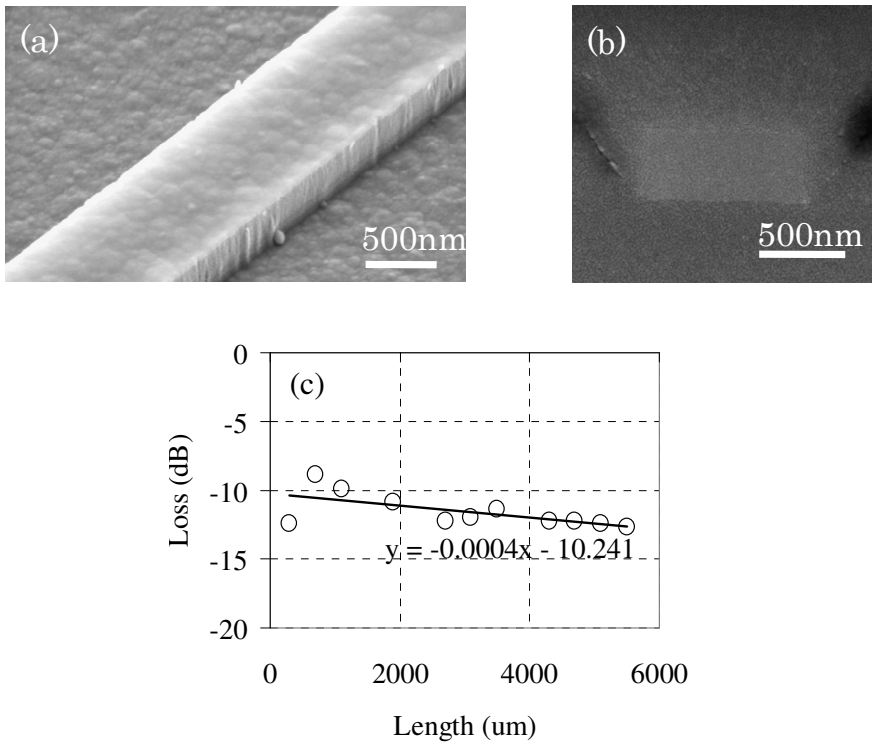

Fig. 5.1 Fabricated SiN/SiO_2 waveguides: (a) and (b) SEM micrographs of the SiN/SiO_2 waveguides before and after the SiO_2 upper-cladding deposition, respectively. (c) Measured data and the linear fit of propagation loss vs. waveguide length.

spectra of the fabricated devices using a broadband light source and a spectrum analyzer. Due to the relatively smaller index contrast than that in Si/SiO_2 waveguides, a tight bending in the SiN/SiO_2 waveguides results in a large bending loss. Consequently, we measured Q factors of 460, 8,500 and 12,900 for the ring resonators with r = 10, 15 and 20μm, all with g = 700nm. Smaller gaps resulted in smaller Q factors due to higher unloading losses into the bus waveguides. Fig. 5.2(a), (b) and (c) show the SEM micrograph of a ring resonator with r = 20μm and g = 700nm, the measured transmission spectrum, and the magnified spectrum for a resonance at 1548nm, respectively.

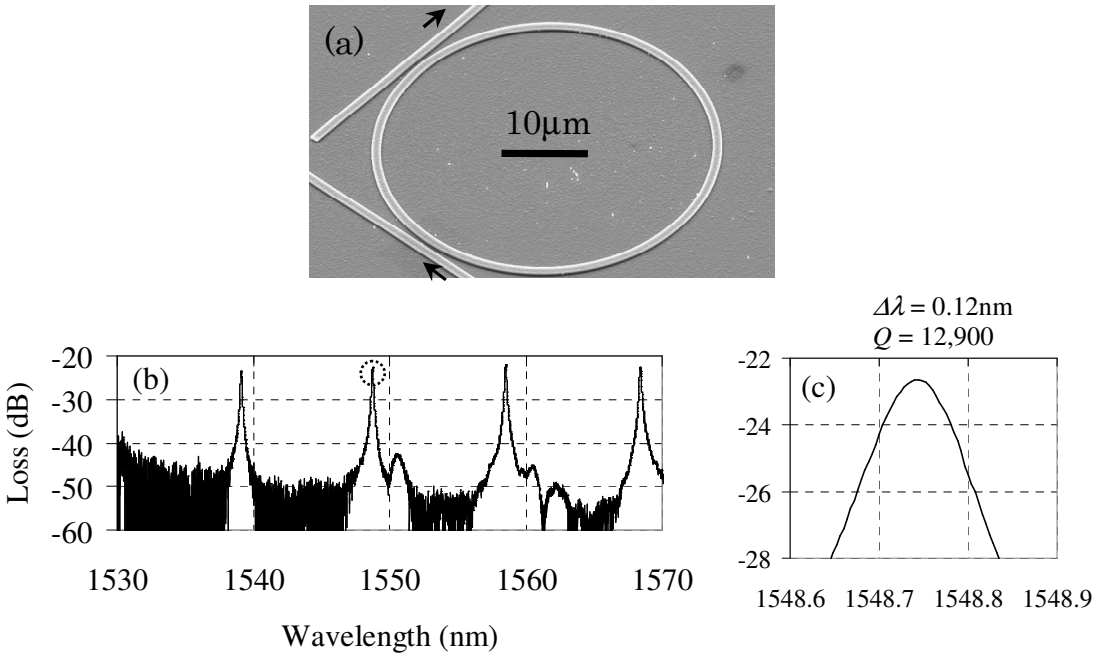

Fig. 5.2 Ring resonators with the SiN/SiO_2 waveguide (r = 20μm, g = 700nm): (a) SEM micrograph of the ring. (b) and (c) Transmission spectra.

5.3 Measurement of Thermal and Kerr Nonlinear Responses of Silicon Nitride Micro-resonators

We investigate the nonlinear response of our fabricated SiN/SiO_2 ring resonator with r = 20μm and g = 700nm. The first measurement uses a tunable CW light source and a high power amplifier. Fig. 5.3(a) shows the shift of the resonant peak wavelength as function of the input power. We observe that the wavelength of the resonant transmission peak shifts to longer wavelength as the input power increases. Fig. 5.3(b) shows the measured output power when the input power is kept constant at 23dBm and the wavelength is swept from shorter to longer wavelengths. This asymmetric response occurs due to the feedback from the ring resonator resulting

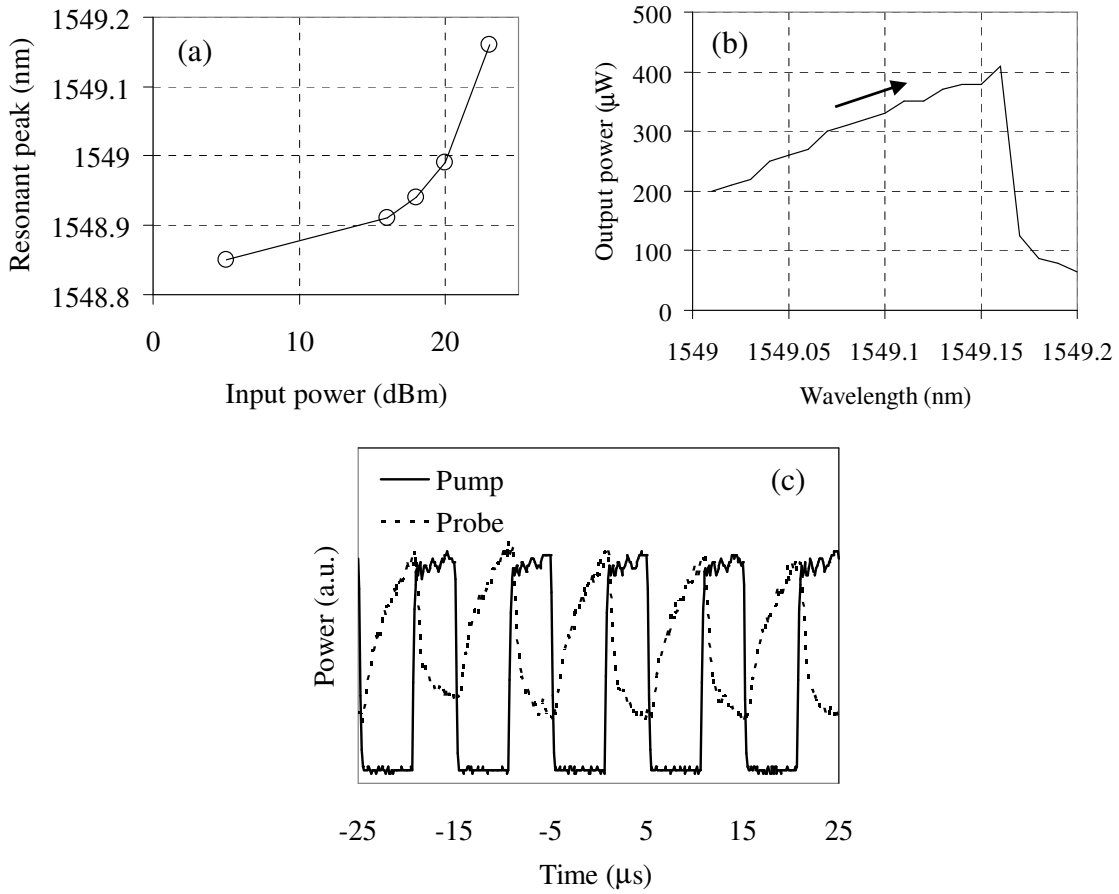

Fig. 5.3 Nonlinear response of the SiN/SiO_2 ring resonator: (a) and (b) Nonlinear responses with CW light, (c) Detected probe modulation by pump light modulated at 100kHz.

in the bistable response as discussed in Ref. [70]. These nonlinear responses can be considered as either ultra-fast Kerr nonlinearity or accumulated thermal nonlinearity since both effects change the refractive index to a larger value (red shift). In order to determine which effect is responsible, we conduct a pump-probe experiment. We use CW probe light of ~0dBm at 1558nm to monitor the resonant transmission (i.e. the resonant wavelength shift) of the device in time, while the resonator is optically modulated by pump light of 23dBm at 1548nm with slow and fast modulation frequencies of 100 kHz and 4 GHz. We obtained a clear probe modulation (see Fig.

5.3(c)) for the pump light modulated at 100kHz. However, we did not observe any probe modulation when we used a pump modulated at 4GHz. Therefore, we conclude that the nonlinearity we observed in these experiments corresponds to the accumulated thermal nonlinearity.

We analyzed the thermal response of our fabricated device as follows. First, we estimate the group index n_g, the absorption coefficient α inside the ring, and the coupling coefficient $(1 - \kappa)$ between the bus waveguide and the ring, by fitting the measured spectrum to the analytic formula of Eq. (2.9). The estimated parameters are $n_g = 1.91$, $\alpha = 2.0$dB/mm and $(1 - \kappa) = 0.0087$. From these values, we can calculate the intensity enhancement inside the ring resonator at the resonant wavelength using Eq. (2.8) as $M = 6.2$. Thus, the peak power inside the ring resonator at the resonant wavelength can be estimated as 6.2 times the input peak power of 26dBm reduced by the coupling loss of 5dB (see Fig. 5.1(c)), corresponding to about 0.78W. And the measured probe modulation in Fig. 5.3(c) of 5.4dB corresponds to a refractive index change Δn of 1.5×10^{-4}. We then calculate the thermal accumulation using the rate equation with linear accumulation term Δn_a and heat dissipation decay term $\Delta n/t_c$,

$$\frac{d\Delta n}{dt} = \Delta n_a - \frac{\Delta n}{t_c}. \tag{5.1}$$

The Δn_a and the characteristic time constant t_c are given by [71, 72],

$$\Delta n_a = \frac{(dn/dT) \cdot I \cdot \alpha}{2 \cdot \rho \cdot C_p}, \tag{5.2}$$

$$t_c = \frac{R_m^2 \cdot \rho \cdot C_p}{4 \cdot k}, \tag{5.3}$$

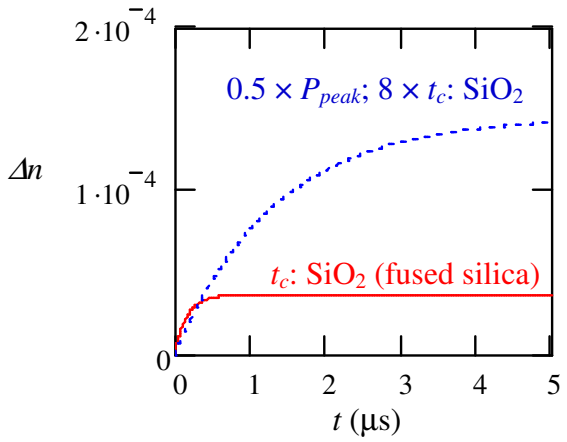

Fig. 5.4 Time response of Δn calculated with Eq. (5.1).

where dn/dT, I, ρ, C_p, R_m and k are the thermo-optic effect, intensity, density, specific heat, mode radius and thermal conductivity, respectively. We use 4dB/cm for the α in the Eq. (5.2) since the estimated value of 2.0dB/mm above will include the bending loss. We use the thermal parameters for fused silica in the literature because the SiN waveguide is surrounded by SiO_2 and dn/dT of SiN is unknown (i.e. $dn/dT \sim 1 \times 10^{-5}$, $\rho \sim 2.2 g/cm^3$, $C_p \sim 0.76 J/gK$, and $k \sim 0.014 W/cmK$). The resultant plot for the time response of Δn is depicted by the red line in Fig. 5.4. The calculated accumulation time is less than 1μs, which is much shorter than the measured response of > 5μs (see Fig. 5.3(c)). Also, the calculated steady state Δn is smaller than the measured value of 1.5×10^{-4}. If we use 8 times longer t_c and a smaller peak power (0.5 of the peak power right on resonance), the accumulation time and the index shift becomes close to the measured results as depicted by the blue line in Fig. 5.4. In fact, the peak intensity should be smaller than the value at the resonant wavelength because the resonant wavelength is slightly shifted by the induced index change. Therefore, the PECVD

SiO_2 film probably has slower heat dissipation due to the high hydrogen content, compared to the high quality fused silica. Note that the uncertainty of the dn/dT of SiN only affects the steady state Δn but not the time constant t_c.

In order to observe the Kerr nonlinear response, we improved the SiN resonators by use of the HSQ resist [60] as the dry etching mask to achieve smoother sidewalls and decrease the scattering loss, by removing the drop port to reduce the unloading loss, and by use of inverse tapers [73] at the input and output waveguide facets to reduce the coupling loss of the pump power. Fig. 5.5(a) shows the transmission spectrum of the all-pass type ring resonator with r = 20μm and g = 600nm. As expected, we obtained a higher quality factor of about 35,600. We introduced modulated pump and CW probe in the same arrangement as in the previous pump-probe experiment, and detected 1GHz modulations as shown in Fig. 5.5(b). Probe 1 and Probe 2 indicate the cases with the probe wavelength slightly shorter and slightly longer than that of the resonant peak wavelength, respectively. Therefore, the modulation phases for these probes should be opposite to each other, as indeed can be observed from the experimental data in Fig. 5.5(b). Thus, we conclude that these modulations originate from the resonance shift by the Kerr nonlinear effect. Now we estimate the n_2 of the SiN film, which to the best of our knowledge is currently unknown in the literature. We first estimate the group index n_g, the absorption coefficient α inside the ring, and the coupling coefficient $(1 - \kappa)$ between the bus waveguide and the ring by fitting the measured spectrum around 1548nm to the analytic formula of all-pass type ring resonator, Eq. (2.3). The obtained parameters are

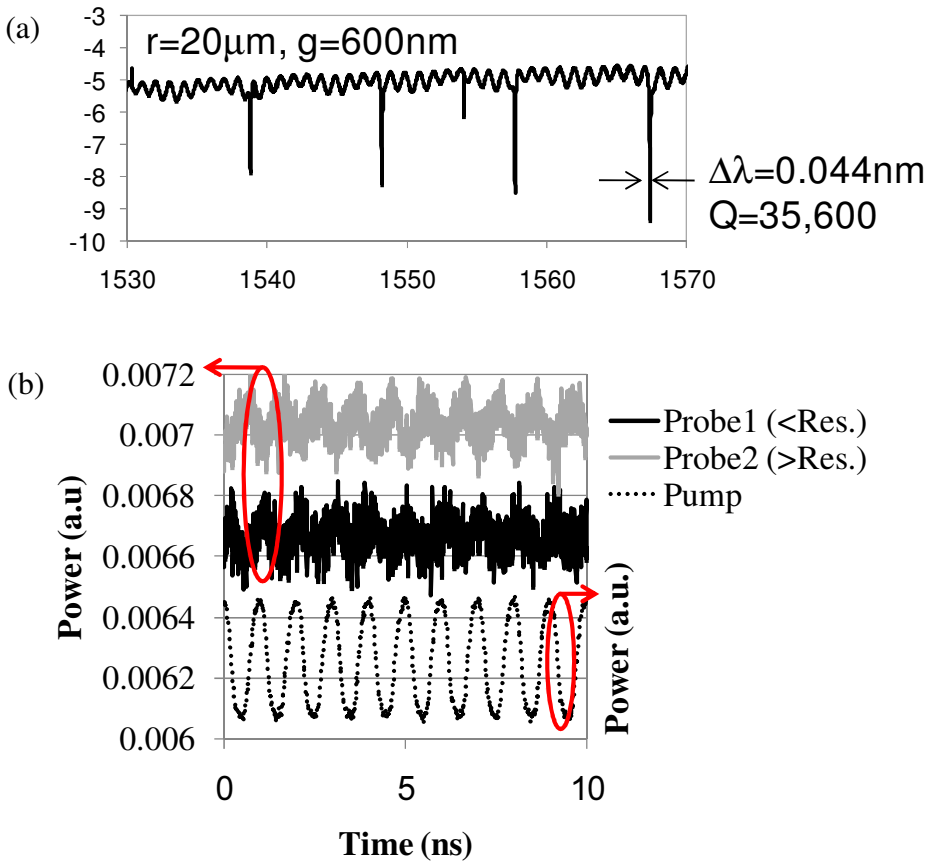

Fig. 5.5 All-pass type ring resonator with the SiN/SiO_2 waveguide (r = 20μm, g = 600nm): (a) Transmission spectrum (b) Detected probe modulations by pump modulated at 1GHz.

n_g = 1.91, α = 1.6dB/mm and (1 − κ) = 0.0089. The reason why the loss inside the ring was not significantly improved is probably that the bending loss is dominant. Next, using these parameters and Eq. (2.2) for the intensity magnification factor M for the all-pass type ring resonator, we estimated M = 11.4. With the input peak power of 26dBm, the improved coupling loss of 2.5dB from the tapered fiber tips to the SiN waveguides, and the estimated magnification factor of 11.4, we obtain the peak power of 2.6W inside the ring resonator. The measured modulation depth of 1.4% in Fig. 5.5(b) corresponds to 0.001nm of resonant wavelength shift, with which we calculate

the corresponding index shift of 1.2×10^{-6}. Therefore, n_2 of our SiN film is estimated as $n_2 = \Delta n/I = 2.4 \times 10^{-15}\text{cm}^2/\text{W}$, which is 10 times larger than that for SiO_2 [42]. This value would make sense because the n_2 of SiN should be in between those of silicon and SiO_2 according to the refractive index and n_2 scaling.

Finally, we briefly discuss on the SiN resonator in terms of the resonator-enhanced nonlinear switching. Since the detected modulation in the above measurement was very small (~1.4%), a much higher pump power has to be used for modulators and switches. In order to reduce the required pump power, we could use the results from Chapter 3 to redesign the resonator. As we did for SiO_2 in Chapter 3, the right hand inequality in Eq. (3.18) is neglected assuming $\beta^{(n)} \sim 0$. With the left hand inequality in Eq. (3.18), the measured finesse $F = 227$, and the perimeter $L = 126\mu\text{m}$ of the all-pass ring resonator, we obtain $\tau_p > 30\text{ps}$. In other words, this resonator can enhance fully the pump pulses longer than 30ps (i.e. 33GHz non-return-to-zero signals). If we redesign the resonator to increase the product of $F \times L$ by reducing α or increasing r and g, the required pump power can be reduced as in Eq. (3.15), however the pump pulses should be longer to be efficiently enhanced as in the left hand inequality in Eq. (3.18). Instead, we could keep the product of $F \times L$ but increase F and decrease L. Using the magnification factor M and the input intensity I_{input}, Eq. (3.15) can be rewritten as,

$$I_{input} \sim \frac{\lambda}{|n_2| \cdot F \cdot L \cdot M} . \tag{5.4}$$

Since M increases when F increases, increasing F is more efficient for reducing I_{input} than increasing L. Therefore, a shorter cavity with a higher finesse is appropriate for this material to achieve a fast resonator-enhanced all-optical switch with a small required pump power. The distributed feedback structures, such as 1D PhC micro-resonators, could be used for this purpose.

5.4 Summary

We introduced and presented experimental evaluations of loss and nonlinear optical response in waveguides and optical resonators, both implemented with SiN/SiO_2 material platform prepared by the PECVD with dual frequency reactors that significantly reduces the stress and the consequent loss in the fabricated devices. We measured a relatively small loss of ~4dB/cm in the SiN/SiO_2 waveguides. The fabricated add-drop and all-pass type ring resonators with the waveguides demonstrated quality factors of Q = 12,900 and 35,600, respectively. The resonators were used to measure both the thermal and ultrafast Kerr nonlinearities. The measured thermal nonlinearity was larger than expected, which was attributed to slower heat dissipation in the PECVD SiO_2. The n_2 for SiN that is unknown in the literature was measured for the first time as $2.4 \times 10^{-15} cm^2/W$, which is 10 times larger than that for SiO_2. For fast resonator-enhanced all-optical switching operation with this material, a smaller micro-resonator with a higher finesse will be required.

Chapter 5, in part, is a reprint of the material as it appears in:

- K. Ikeda, R. E. Saperstein, N. Alic and Y. Fainman, “Thermal and Kerr nonlinear properties of plasma-deposited silicon nitride/ silicon dioxide

waveguides," Opt. Express 16, 12987-12994 (2008).

The dissertation author was the primary investigator and author of this paper. The co-authors listed in the publication assisted and supervised the research which forms the basis for this chapter.

Chapter 6

Conclusions and Future Directions

This dissertation has systematically addressed the critical issue of long free-carrier lifetime in all-optical nonlinear switching with resonant enhancement on a silicon chip. The phenomenon observed previously in demonstrated devices was that the all-optical nonlinear switching in silicon micro-resonators was induced through the free carrier refraction via TPA and the lifetime of the photo-excited free-carriers had been the limit for the response time of the switching or modulating operations. For faster switching, bound electronic nonlinearity, i.e. Kerr nonlinearity is preferred because of the ultrafast response. Therefore, our first question was if it is possible to obtain all-optical switching based on the Kerr nonlinearity in silicon micro-resonators with any specific structure design.

We first reviewed several basic optical resonant structures categorized into localized feedback structures and distributed feedback structures. The mathematical expressions for these structures introduced here are used in the main part of this dissertation. In addition, we discussed an application of the distributed feedback structure, i.e. wavelength selective coupler with vertical gratings, as a new type of devices useful for on-chip scale PICs.

We then analyzed the nonlinear switching in a silicon micro-resonator, in particular, how the switching works considering the free carrier nonlinearity excited via TPA and the Kerr nonlinearity. The analysis was extended to the discussion of if it is possible to obtain all-optical switching based on the Kerr nonlinearity in silicon micro-resonators with any specific structure design. We presented material and structural criteria for ultra-fast Kerr nonlinear switching in optical resonant cavities. The material criterion with a new nonlinear figure of merit suggested that Si, GaAs and even AlGaAs cannot be considered as the materials for the resonator-enhanced Kerr nonlinear switch at 1.55μm of wavelength, due to the large free-carrier nonlinearity excited by two-photon or three-photon process. Insulators with wider band-gaps such as SiO_2 and SiN are interesting materials to investigate for this purpose.

Since we have quantitatively found that it is impossible to obtain all-optical switching based on the Kerr nonlinearity in silicon micro-resonators, the material of micro-resonators has to be reconsidered in two directions to solve the issue of the long-lived free carriers; (i) a material with faster carrier recombination, (ii) a material with a wider energy band gap, i.e. smaller TPA coefficient. In addition, both the materials should be compatible to the standard CMOS process for on-chip scale integration. The remaining part of this dissertation was devoted to the works on the above two directions.

We investigated amorphous silicon as a material with faster carrier recombination since a large density of localized defect states in amorphous silicon will

work as recombination centers and lead to a shorter carrier lifetime. We presented the first measurements of optical nonlinearity due to the free carrier effects in amorphous silicon films using the z-scan technique, demonstrating the enhanced nonlinearity due to the existence of midgap localized states. We also introduced a new composite waveguide structure consisting of amorphous and crystalline silicon. Due to the existence of the midgap localized states in amorphous silicon, the measured free-carrier lifetime in the composite waveguides (300ps and 400ps) was shorter than the value in pure crystalline silicon waveguides (1.6ns). The detail measurements showed that although the free carriers excited within the amorphous region of the composite waveguides recombine very quickly (< 25ps), the free carriers excited within the crystalline region move into the amorphous region much slower (530ps) than the decay time within the amorphous region. The waveguide with only hydrogenated amorphous silicon was also fabricated and demonstrated a very short lifetime (< 40ps). However, we have to reconsider how to apply this waveguide to the resonator-enhanced all-optical switching since the free carrier absorption is the dominant nonlinear effect in the waveguide. We also measured a very short carrier lifetime (~30ps) in a ring resonator with a composite waveguide fabricated with a different process, which however was attributed to the high density of surface states due to the rough sidewall of the waveguide or to the silicide contamination during the fabrication process.

We also studied SiN as a material with a wider energy band gap since it is a common material in the standard CMOS process and the relatively large refractive

index results in small dimensions of waveguide devices. We presented experimental evaluations of loss and nonlinear optical response in waveguides and optical resonators, both implemented with a SiN/SiO_2 material platform prepared by PECVD with dual frequency reactors that significantly reduces the stress and the consequent loss of the devices. The fabricated ring resonators are used to observe the all-optical switching and to measure both the thermal and ultrafast Kerr nonlinearities. The nonlinear refractive index n_2 for SiN that is unknown in the literature is measured as $2.4 \times 10^{-15} cm^2/W$, for the first time. According to our theoretical design considerations and the measured parameters in the fabricated resonator, a smaller micro-resonator with a higher finesse will be required for fast resonator-enhanced all-optical switching operation using this material.

At the last, we suggest future research directions led from the results presented in this dissertation. We have investigated amorphous silicon as a material with faster carrier recombination and SiN as a material with a wider energy band gap, for fast resonator-enhanced all-optical switching. However, there will be other materials useful for these purposes. For instance, ion-implanted silicon micro-resonators demonstrated fast carrier recombination [57] and chalcogenide glasses have a wide energy band gap and also very large n_2 [74], although their compatibility with the standard CMOS process has to be examined since the fabrication of the ion-implanted silicon devices and the chalcogenide glasses are accompanied respectively by the high temperature thermal activation process (> 1000°C) and the specialized deposition process.

For amorphous silicon, we have experimentally shown that the defect states in the amorphous region of the newly introduced composite waveguides work as the recombination centers for the photo-excited free-carriers in the crystalline region, and shorten the overall free-carrier lifetime in the composite waveguides. However, the decay time was not as short as that in the amorphous region. A detail study of the carrier dynamics around the boundary between the amorphous and crystalline regions (numerical simulations etc.) could give a solution to further shorten the lifetime of the composite waveguide structures. The waveguide made of only hydrogenated amorphous silicon is also interesting to be used since it demonstrated a very fast recombination. The first step for this will be to analyze how to apply the waveguide to the resonator-enhanced all-optical switching since the free carrier absorption is the dominant nonlinear effect in the waveguide. In addition, it would be interesting to further investigate the reason why we obtained the very fast recombination of ~30ps in the ring resonators fabricated with the nickel mask process, which was attributed to the rough sidewall of the waveguide or the contamination during the RIE process.

For the SiN/SiO_2 material system, a redesign of the micro-resonators with a shorter cavity and a higher finesse is necessary to obtain a larger modulation depth and to keep the efficient and fast response. 1D PhC micro-resonators would be one of the interesting structures for such a resonator. In addition to the resonator-enhanced switching application, nonlinear processes in long interaction scheme using the SiN/SiO_2 waveguides are also interesting phenomena to investigate since the free-carrier nonlinearity can be neglected in this material system and we have found n_2

of the SiN/SiO_2 waveguides is 10 times larger than silica waveguides. In the mean time, the reduction of the waveguide loss will have to be attempted in order to be used for various applications. The main source of propagation loss in the waveguide is thought to be from the material itself, such as the hydrogen content. Although a high temperature annealing could improve the material absorption, optimization of the PECVD process will be one of the important directions because of the low process temperature.

Appendices

A.1 Silicon Fabrication Processes

In this section, we review the silicon fabrication processes used in this dissertation. We first used the nickel hard mask process (Chapter 2 and 4) and then developed the new HSQ process to improve the sidewall roughness and the propagation loss (Chapter 4). After these fabrication processes, we lap the back side of the processed chip to make the cleaving easier, and cleave the chip at the input and output waveguides so that the tapered fibers can access to the input and output waveguide facets when the devices are measured.

A.1.1 Nickel Hard Mask Process

First, PMMA positive e-beam resist (950K molecular weight, 4% in Anisole, from MicroChem Co.) is spin-coated on a SOI chip with 250nm-thick silicon layer on 3μm-thick buried oxide layer, followed by soft-baking with a hot plate set at 180°C for 90s. The spin speed is 4000rpm, resulting in about 200nm-thick PMMA film. The surface of the chip is exposed by e-beam with the acceleration voltage of 30kV, the beam current of 10 or 20pA, the area dose of 400μC/cm^2 and the magnification of

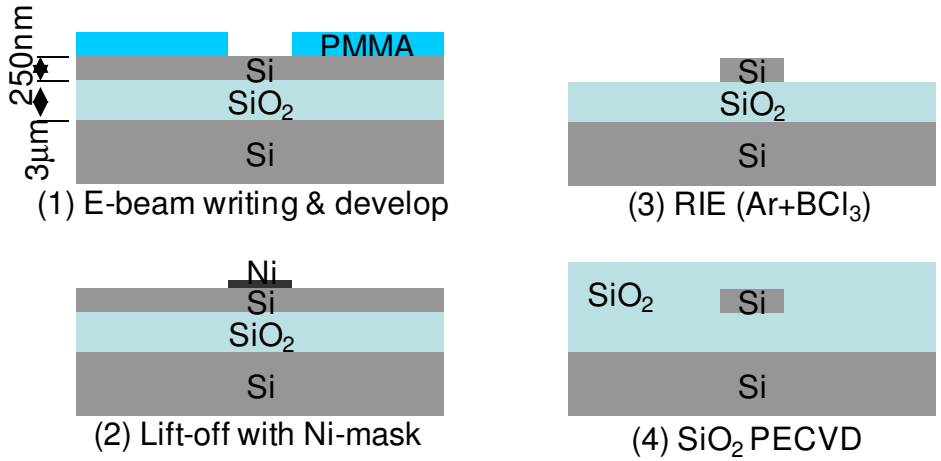

Fig. A.1.1 Fabrication process with the nickel hard mask

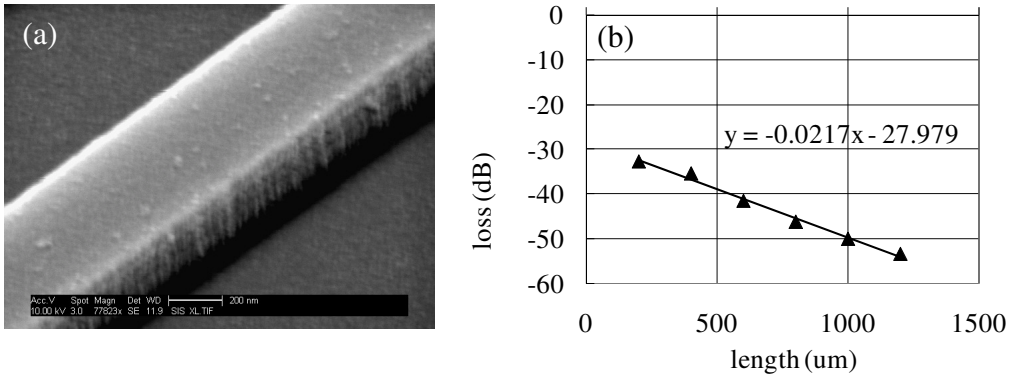

Fig. A.1.2 (a) SEM micrograph of the fabricated waveguide, (b) typical measured loss data for TE-like mode vs. waveguide length for the waveguides (~ 22dB/mm).

1000 (the writing field of 100μm × 100μm), using the Raith50 e-beam writer. The exposed PMMA is developed with 1:2 Methyl-Isobutyl-Ketone (MIBK)/ Isopropanol (IPA) developer for 40s. Then, nickel film with 20nm thickness is deposited on the developed PMMA film with the deposition speed of 0.1 ~ 0.2 nm/s using the Temescal BJD 1800 e-beam evaporator. The chip after the nickel deposition is immersed in heated acetone to lift-off the nickel film. If necessary to remove the residual nickel film, the beaker containing the chip in acetone is exposed by ultra-sound for less than

3min. At this point, we have the patterned nickel hard mask for dry-etching process. RIE with 10sccm Ar and 10sccm BCl_3 gas mixture, the process pressure of 30mT and the RIE power of 100W is performed for 400s divided into 10 steps, using the Trion etcher. After the nickel hard mask is removed by a commercial nickel etchant, SiO_2 cladding is deposited over the etched structures using the Oxford Plasmalab PECVD with the gas mixture of 5% SiH_4 diluted by N_2 (170sccm) and NO_2 (710sccm), the process pressure of 1000mT, the process temperature of 350°C, and the plasma frequency of 13.56MHz (20W, RF only). The above fabrication processes are summarized in Fig. A.1.1. The SEM picture and the measured loss data (TE-like mode) for a typical fabricated waveguide are presented in Fig. A.1.2(a) and (b), respectively.

A.1.2 HSQ Mask Process

HSQ negative e-beam resist [60] (FOx-13 from Dow Corning Co.) is spin-coated on a SOI chip with 250nm-thick silicon layer on 3μm-thick buried oxide layer, followed by soft-baking with a hot plate set at 90°C for 5min. The spin speed is 1500rpm, resulting in about 200nm-thick HSQ film. The surface of the chip is exposed by e-beam with the acceleration voltage of 30kV, the beam current of 10 or 20pA, the area dose of 1000μC/cm^2 and the magnification of 1000 (the writing field of 100μm × 100μm), using the Raith50 e-beam writer. The exposed HSQ film is developed with 25% Tetra-Methyl Ammonium Hydroxide (TMAH) developer for less than 60s, followed by post-baking with a hot plate set at 300°C for 3min. At this point, we have the patterned HSQ mask for dry-etching process. RIE/Inductively Coupled Plasma

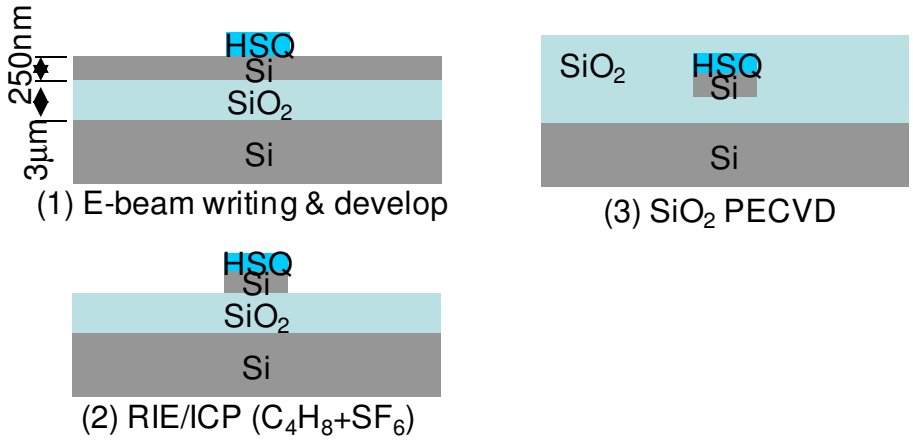

Fig. A.1.3 Fabrication process with the HSQ mask

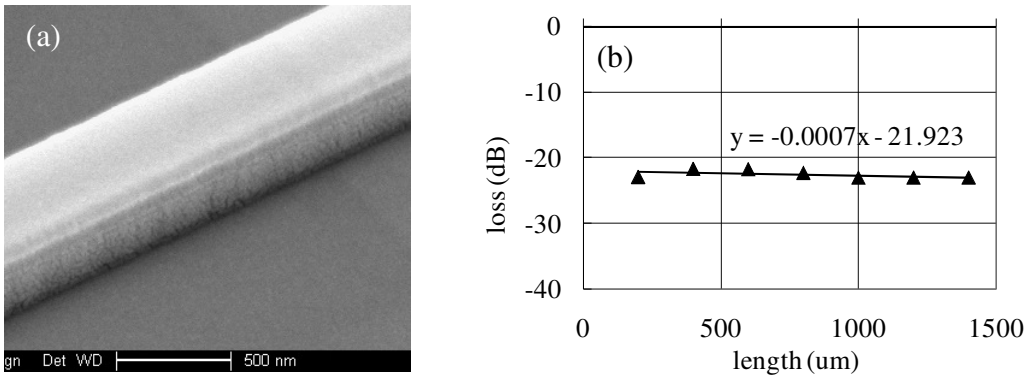

Fig. A.1.4 (a) SEM micrograph of the fabricated waveguide, (b) typical measured loss data for TE-like mode vs. waveguide length for the waveguides (~ 7dB/cm).

(ICP) with 50sccm C_4H_8 and 25sccm SF_6 gas mixture, the process pressure of 15mT and the RIE/ICP power of 30/1200W is performed at 20°C for 100s, using the Oxford P100 etcher. The residual HSQ mask does not have to be removed since it does not affect the propagating mode in the etched structure because of the low refractive index close to SiO_2. SiO_2 cladding is deposited over the etched structures using the Oxford Plasmalab PECVD with the gas mixture of 5% SiH_4 diluted by N_2 (170sccm) and NO_2 (710sccm), the process pressure of 1000mT, the process temperature of 350°C, and the plasma frequency of 13.56MHz (20W, RF only). The above fabrication processes are

summarized in Fig. A.1.3. The SEM picture and the measured loss data (TE-like mode) for a typical fabricated waveguide are presented in Fig. A.1.4(a) and (b), respectively.

A.1.3 Amorphous Silicon Depositions

The deposition processes for the a-Si, a-Si:H(1) and a-Si:H(2) films used in Chapter 4 are summarized as follows. The a-Si film is deposited using the Denton Discovery 18 Sputter System (RF sputtering), with the RF power 400W, the target material of silicon, the Ar flow of 35sccm, the deposition rate of 350nm/h and the process temperature of room temperature. The a-Si:H(1) is deposited using the Plasma-Therm 790 PECVD System, with 115sccm helium and 9sccm silane gas mixture, the process pressure of 980mT, the process power of 50W, the deposition rate of about 12.3nm/min, at 300°C [75]. This PECVD system is located in the Integrated Nanosystems Research Facility at University of California, Irvine. The a-Si:H(2) is deposited using a PECVD system with silane and helium gas mixture at 400°C. This process is done by a nano-fabrication foundry, the MEMS and Nanotechnology Exchange.

A.2 Estimation of Nonlinear Optical Coefficients for $Al_{0.36}Ga_{0.64}As$

The nonlinear refractive index n_{2_36}, the TPA coefficient $\beta^{(2)}{}_{36}$ and the ThPA coefficient $\beta^{(3)}{}_{36}$ for $Al_{0.36}Ga_{0.64}As$ can be approximated with the following equations [41, 44],

$$n_{2\_36}(x) = \left(\frac{E_{g\_36}}{E_{g\_18}}\right)^{-4} n_{2\_18}(x), \tag{A.2.1}$$

$$\beta_{36}^{(2)}(x) = \left(\frac{E_{g\_36}}{E_{g\_18}}\right)^{-3} \beta_{18}^{(2)}(x), \tag{A.2.2}$$

$$\beta_{36}^{(3)}(x) = \left(\frac{E_{g\_36}}{E_{g\_18}}\right)^{-7} \beta_{18}^{(3)}(x), \tag{A.2.3}$$

where E_{g_18} and E_{g_36} are the bandgap energies for $Al_{0.18}Ga_{0.72}As$ (1.648eV) and $Al_{0.36}Ga_{0.64}As$ (1.873eV); n_{2_18}, $\beta^{(2)}{}_{18}$ and $\beta^{(3)}{}_{18}$ are the nonlinear refractive index, the TPA coefficient and the ThPA coefficient for $Al_{0.18}Ga_{0.72}As$, respectively; x is the photon energy normalized by the bandgap energy. Since we need the nonlinear coefficients for $Al_{0.36}Ga_{0.64}As$ at 1.55μm (0.8eV), $x = 0.8/E_{g\_36} = 0.704/E_{g\_18} = 0.427$. Therefore, we read n_{2_18}, $\beta^{(2)}{}_{18}$ and $\beta^{(3)}{}_{18}$ at 1.76μm (0.704eV) from the plots in ref. [39] and [43] as 1.0×10^{-13}cm^2/W, 0.01cm/GW and 0.22cm^3/GW^2 respectively and calculated n_{2_36}, $\beta^{(2)}{}_{36}$ and $\beta^{(3)}{}_{36}$ at 1.55μm with the above equations as 6.0×10^{-14}cm^2/W, 0.007cm/GW and 0.09cm^3/GW^2 respectively.

Bibliography

[1] See for example: I. P. Kaminow and T. Li, *Optical Fiber Telecommunications IV-A: Components (Optics and Photonics)*, Academic Press, San Diego, 2002; I. P. Kaminow and T. Li, *Optical Fiber Telecommunications IV-B: Systems and Impairments (Optics and Photonics)*, Academic Press, San Diego, 2002.

[2] See for example: L. Pavesi and G. Guillot, *Optical Interconnects: The Silicon Approach*, Springer-Verlag, Berlin Heidelberg, 2006.

[3] K. K. Lee, D. R. Lim, L. C. Kimerling, J. Shin, and F. Cerrina, "Fabrication of ultralow-loss Si/SiO_2 waveguides by roughness reduction," Opt. Lett. 26, 1888-1890 (2001).

[4] Y. Vlasov and S. McNab, "Losses in single-mode silicon-on-insulator strip waveguides and bends," Opt. Express 12, 1622-1631 (2004).

[5] A. Koster, E. Cassan, S. Laval, L. Vivien, and D. Pascal, "Ultracompact splitter for submicrometer silicon-on-insulator rib waveguides," J. Opt. Soc. Am. A 21, 2180-2185 (2004).

[6] K. Ikeda, M. Nezhad and Y. Fainman, "Wavelength selective coupler with vertical gratings on silicon chip," Appl. Phys. Lett. 92, 201111 (2008).

[7] A. Liu, R. Jones, L. Liao, D. Samara-Rubio, D. Rubin, O. Cohen, R. Nicolaescu and M. Paniccia, "A high-speed silicon optical modulator based on a metal–oxide–semiconductor capacitor," Nature 427, 615-618 (2004).

[8] V. R. Almeida, C. A. Barrios, R. R. Panepucci and M. Lipson, "All-optical control of light on a silicon chip," Nature 431, 1081-1084 (2004).

[9] Q. Xu, S. Manipatruni, B. Schmidt, J. Shakya, and M. Lipson, "12.5 Gbit/s carrier-injection-based silicon micro-ring silicon modulators," Opt. Express 15, 430-436 (2007).

[10] O. Boyraz and B. Jalali, "Demonstration of a silicon Raman laser," Opt. Express 12, 5269-5273 (2004).

[11] A. W. Fang, H. Park, O. Cohen, R. Jones, M. J. Paniccia, and J. E. Bowers, "Electrically pumped hybrid AlGaInAs-silicon evanescent laser," Opt. Express 14, 9203-9210 (2006).

[12] R. Claps, D. Dimitropoulos, V. Raghunathan, Y. Han, and B. Jalali, "Observation of stimulated Raman amplification in silicon waveguides," Opt. Express 11, 1731-1739 (2003).

[13] H. Park, A. W. Fang, O. Cohen, R. Jones, M. J. Paniccia, and J. E. Bowers, "An electrically pumped AlGaInAs-Silicon Evanescent Amplifier," IEEE Photon. Technol. Lett. 19, 230-232 (2007).

[14] H. Park, A. W. Fang, R. Jones, O. Cohen, O. Raday, M. N. Sysak, M. J. Paniccia, and J. E. Bowers, "A hybrid AlGaInAs-silicon evanescent waveguide photodetector," Opt. Express 15, 6044-6052 (2007).

[15] T. Tanabe, M. Notomi, S. Mitsugi, A. Shinya and E. Kuramochi, "All-optical switches on a silicon chip realized using photonic crystal nanocavities," Appl. Phys. Lett. 87, 151112 (2005).

[16] J. S. Foresi, P. R. Villeneuve, J. Ferrera, E. R. Thoen, G. Steinmeyer, S. Fan, J. D. Joannopoulos, L. C. Kimerling, H. I. Smith and E. P. Ippen, "Photonic-bandgap microcavities in optical waveguides," Nature 390, 143-145 (1997).

[17] C. A. Barrios, V. R. Almeida, R. R. Panepucci, B. S. Schmidt and M. Lipson, "Compact silicon tunable Fabry-Perot resonator with low power consumption," IEEE Photon. Technol. Lett. 16, 506-508 (2004).

[18] H.-C. Kim, K. Ikeda and Y. Fainman, "Resonant waveguide device with vertical gratings," Opt. Lett. 32, 539-541 (2007).

[19] For example, L. F. Stokes, M. Chodorow and H. J. Shaw, "All-single-mode fiber resonator," Opt. Lett. 7, 288-290 (1982).

[20] H. -C. Kim, K. Ikeda, and Y. Fainman, "Tunable Transmission Resonant Filter and Modulator With Vertical Gratings," J. Lightwave Technol. 25, 1147-1151 (2007).

[21] J. T. Hastings, M. H. Lim, J. G. Goodberlet and H. I. Smith, "Optical waveguides with apodized sidewall gratings via spatial-phase-locked electron-beam lithography," J. Vac. Sci. Technol. B 20, 2753-2757 (2002).

[22] P. Yeh and H. F. Taylor, "Contradirectional frequency-selective couplers for guided-wave optics," Appl. Opt. 19, 2848-2855 (1980).

[23] A. Yariv and P. Yeh, *Optical Waves in Crystals*, John Wiley & Sons, Hoboken NJ, 2003.

[24] H. W. Tan, H. M. van Driel, S. L. Schweizer, R. B. Wehrspohn and U. Gosele, "Nonlinear optical tuning of a two-dimensional silicon photonic crystal," Phys. Rev. B 70, 205110 (2004)

[25] H. Kogelnik and H. P. Weber, "Rays, stored energy, and power flow in dielectric waveguides," J. Opt. Soc. Am. 64, 174-185 (1974).

[26] M. Notomi, K. Yamada, A. Shinya, J. Takahashi, C. Takahashi and I. Yokohama, "Extremely Large Group-Velocity Dispersion of Line-Defect Waveguides in Photonic Crystal Slabs," Phys. Rev. Lett. 87, 253902 (2001).

[27] R. W. Boyd, *Nonlinear Optics*, Academic Press, San Diego CA, 1992.

[28] M. Notomi, A. Shinya, S. Mitsugi, E. Kuramochi and H. Ryu, "Waveguides, resonators and their coupled elements in photonic crystal slabs," Opt. Express 12, 1551-1561 (2004).

[29] M. Dinu, F. Quochi and H. Garcia, "Third-order nonlinearities in silicon at telecom wavelengths," Appl. Phys. Lett. 82, 2954-2956 (2003).

[30] V. Van, T. A. Ibrahim, P. P. Absil, F. G. Johnson, R. Grover and P.-T. Ho, "Optical signal processing using nonlinear semiconductor microring resonators," IEEE J. Sel. Top. Quantum Electron. 8, 705-713 (2002).

[31] J. E. Heebner., N. N. Lepeshkin, A. Schweinsberg, G. W. Wicks, R. W. Boyd, R. Grover and P.-T. Ho, "Enhanced linear and nonlinear optical phase response of AlGaAs microring resonators," Opt. Lett. 29, 769-771 (2004).

[32] V. Mizrahi, K. W. DeLong, G. I. Stegeman, M. A. Saifi and M. J. Andrejco, "Two-photon absorption as a limitation to all-optical switching," Opt. Lett. 14, 1140-1142 (1989).

[33] G. Priem, P. Bienstman, G. Morthier and R. Baets, "Impact of absorption mechanisms on Kerr-nonlinear resonator behavior," J. Appl. Phys. 99, 063103 (2006).

[34] M. J. Weber, *Handbook of Optical Materials*, CRC Press, 2003.

[35] A. H. Kachare, W. G. Spitzer and J. E. Fredrickson, "Refractive-index of ion-implanted GaAs," J. Appl. Phys. 47, 4209-4212 (1976).

[36] R. E. Fern and A. Onton, "Refractive index of AlAs," J. Appl. Phys. 42, 3499-3500 (1971).

[37] R. A. Soref and B. R. Bennett, "Electrooptical effects in silicon," IEEE J. Quantum Electron. QE-23, 123-129 (1987).

[38] S. Adachi (Ed.), *Properties of Aluminum Gallium Arsenide*, INSPEC IEE, 1993.

[39] A. Villeneuve, C. C. Yang, G. I. Stegeman, C.-H. Lin and H.-H. Lin, "Nonlinear refractive-index and two photon-absorption near half the band gap in AlGaAs," Appl. Phys. Lett. 62, 2465-2467, 1993.

[40] K. Al-hemyari, J. S. Aitchison, C. N. Ironside, G. T. Kennedy, R. S. Grant and W. Sibbett, "Ultrafast all-optical switching in GaAlAs integrated interferometer in 1.55 μm spectral region," Electron. Lett. 28, 1090-1092 (1992).

[41] M. Sheik-Bahae, D. J. Hagan, and E. W. Van Stryland, "Dispersion and band-gap scaling of the electronic Kerr effect in solids associated with two-photon absorption," Phys. Rev. Lett. 65, 96-99 (1990).

[42] A. Boskovic, S. V. Chernikov, J. R. Taylor, L. Gruner-Nielsen and O. A. Levring, "Direct continuous-wave measurement of n_2 in various types of telecommunication fiber at 1.55μm," Opt. Lett. 21, 1966-1968 (1996).

[43] J. U. Kang, A. Villeneuve, M. Sheik-Bahae, G. I. Stegeman, K. Al-hemyari, J. S. Aitchison and C. N. Ironside, "Limitation due to three-photon absorption on the useful spectral range for nonlinear optics in AlGaAs below half band gap," Appl. Phys. Lett. 65, 147-149 (1994).

[44] B. S. Wherrett, "Scaling rules for multiphoton interband absorption in semiconductors," J. Opt. Soc. Am. B 1, 67-72 (1984).

[45] P. Audebert, Ph. Daguzan, A. Dos Santos, J. C. Gauthier, J. P. Geindre, S. Guizard, G. Hamoniaux, K. Krastev, P. Martin, G. Petite and A. Antonetti, "Space-Time Observation of an Electron Gas in SiO_2," Phys. Rev. Lett. 73, 1990-1993 (1994).

[46] D. K. Armani, T. J. Kippenberg, S. M. Spillane and K. J. Vahala, "Ultra-high-Q toroid microcavity on a chip," Nature 421, 925-928 (2003).

[47] T. Uesugi, B. Song, T. Asano and S. Noda, "Investigation of optical nonlinearities in an ultra-high-Q Si nanocavity in a two-dimensional photonic crystal slab," Opt. Express 14, 377-386 (2006).

[48] T. Tanabe, M. Notomi, S. Mitsugi, A. Shinya and E. Kuramochi, "Fast bistable all-optical switch and memory on a silicon photonic crystal on-chip," Opt. Lett. 30, 2575-2577 (2005).

[49] P. M. Fauchet, D. Hulin, R. Vanderhaghen, A. Mourchid and W. L. Nighan Jr., "The properties of free carriers in amorphous silicon," J. Non-Cryst. Solids. 141, 76-87 (1992).

[50] R. A. Street, *Hydrogenated Amorphous Silicon*, Cambridge University Press, Cambridge, 1991.

[51] A. Harke, M. Krause and J. Mueller, "Low-loss singlemode amorphous silicon waveguides," Electron. Lett. 41, 1377-1379 (2005).

[52] G. Cocorullo, F. G. Della Corte, R. De Rosa, I. Rendina, A. Rubino and E. Terzini, "Amorphous silicon-based guided-wave passive and active devices for silicon integrated optoelectronics," IEEE J. Sel. Top. Quantum Electron. 4, 997-1002 (1998).

[53] M. Iodice, G. Mazzi and L. Sirleto, "Thermo-optical static and dynamic analysis of a digital optical switch based on amorphous silicon waveguide," Opt. Express 14, 5266-5278 (2006).

[54] A. A. Said, M. Sheik-Bahae, D. J. Hagan, T. H. Wei, J. Wang, J. Young and E. W. Van Stryland, "Determination of bound-electronic and free-carrier nonlinearities in ZnSe, GaAs, CdTe, and ZnTe," J. Opt. Soc. Am. B 9, 405-414 (1992).

[55] M. J. A. de Dood, A. Polman, T. Zijlstra and E. W. J. M. van der Drift, "Amorphous silicon waveguides for microphotonics," J. Appl. Phys. 92, 649-653 (2002).

[56] M. N. Islam, C. E. Soccolich, R. E. Slusher, A. F. J. Levi, W. S. Hobson and M. G. Young, "Nonlinear spectroscopy near half-gap in bulk and quantum well GaAs/AlGaAs waveguides," J. Appl. Phys. 71, 1927-1935 (1992).

[57] T. Tanabe, K. Nishiguchi, A. Shinya, E. Kuramochi, K. Yamada, T. Tsuchizawa, T. Watanabe and H. Fukuda, "Fast all-optical switching using ion-implanted silicon photonic crystal nanocavities," Appl. Phys. Lett. 90, 031115 (2007).

[58] V. R. Almeida, C. A. Barrios, R. R. Panepucci, M. Lipson, M. A. Foster, D. G. Ouzounov and A. L. Gaeta, "All-optical switching on a silicon chip," Opt. Lett. 29, 2867-2869 (2004).

[59] T. Barwicz, C. W. Holzwarth, P. T. Rakich, M. A. Popović, E. P. Ippen and H. I. Smith, "Optical loss in silicon microphotonic waveguides induced by metallic contamination," Appl. Phys. Lett. 92, 131108 (2008).

[60] W. Henschel, Y. M. Georgiev and H. Kurz, "Study of a high contrast process for hydrogen silsesquioxane as a negative tone electron beam resist," J. Vac. Sci. Technol. B 21, 2018-2025 (2003).

[61] B. Soerowirdjo and P. Ashburn, “Effects of surface treatments on the electrical characteristics of bipolar transistors with polysilicon emitters,” Solid-State Electron. 26, 495-498 (1983).

[62] A. Neugroschel, M. Arienzo, Y. Komem and R. D. Isaac, “Experimental Study of the Minority-Carrier Transport at the Polysilicon-Monosilicon Interface,” IEEE Trans. Electron Devices ED-32, 807-816 (1985).

[63] K. Preston, P. Dong, B. Schmidt and M. Lipson, “High-speed all-optical modulation using polycrystalline silicon microring resonators,” Appl. Phys. Lett. 92, 151104 (2008).

[64] Q. Lin, O. J. Painter and G. P. Agrawal, “Nonlinear optical phenomena in silicon waveguides: modeling and applications,” Opt. Express 15, 16604-16644 (2007).

[65] W. Stutius and W. Streifer, “Silicon nitride films on silicon for optical waveguides,” Appl. Opt. 16, 3218-3222 (1977).

[66] C. H. Henry, R. F. Kazarinov, H. J. Lee, K. J. Orlowsky, and L. E. Katz, “Low loss Si_3N_4-SiO_2 optical waveguides on Si,” Appl. Opt. 26, 2621-2624, (1987).

[67] N. Daldosso, M. Melchiorri, F. Riboli, M. Girardini, G. Pucker, M. Crivellari, P. Bellutti, A. Lui and L. Pavesi, “Comparison Among Various Si_3N_4 Waveguide Geometries Grown Within a CMOS Fabrication Pilot Line,” J. Ligthtwave Technol. 22, 1734-1740 (2004).

[68] T. Barwicz, M. A. Popovic, M. R. Watts, P. T. Rakich, E. P. Ippen and H. I. Smith, “Fabrication of Add-Drop Filters Based on Frequency-Matched Microring Resonators,” J. Ligthtwave Technol. 24, 2207-2218 (2006).

[69] E. P. van de Ven, I-W. Connick, and A. S. Harrus, “Advantages of dual frequency PECVD for deposition of ILD and passivation films,” Proc. IEEE VLSI Multilevel Interconnection Conference (VMIC), 194-201 (1990).

[70] M. Notomi, A. Shinya, S. Mitsugi, G. Kira, E. Kuramochi and T. Tanabe, “Optical bistable switching action of Si high-Q photonic-crystal nanocavities,” Opt. Express, 13, 2678-2687 (2005).

[71] M. Sheik-Bahae, A. A. Said, T.-H. Wei, D. J. Hagan and E. W. Van Stryland, “Sensitive measurement of optical nonlinearities using a single beam,” IEEE J. Quantum Electron. 26, 760-769 (1990).

[72] C. A. Carter and J. M. Harris, “Comparison of models describing the thermal lens effect,” Appl. Opt. 23, 476-481 (1984).

[73] V. R. Almeida, R. R. Panepucci and M. Lipson, “Nanotaper for compact mode conversion,” Opt. Lett. 28, 1302-1304 (2003).

[74] Y. Ruan, W. Li, R. Jarvis, N. Madsen, A. Rode, B. Luther-Davies, “Fabrication and characterization of low loss rib chalcogenide waveguides made by dry etching,” Opt. Express 12, 5140-5145 (2004).

[75] J. C. Knights, R. A. Lujan, M. P. Rosenblum, R. A. Street and D. K. Bieglesen, “Effects of inert gas dilution of silane on plasma-deposited a-Si:H films,” Appl. Phys. Lett. 38, 331-333 (1981).